Doctoral Thesis in Physics

Dark Matter searches targeting Dwarf Spheroidal Galaxies with the Fermi Large Area Telescope

Maja Garde Lindholm

Oskar Klein Centre for
Cosmoparticle Physics

and

Cosmology, Particle Astrophysics
and String Theory

Department of Physics
Stockholm University
SE-106 91 Stockholm

Stockholm, Sweden 2015

Cover image: Top left: Optical image of the Carina dwarf galaxy. Credit: ESO/G. Bono & CTIO. Top center: Optical image of the Fornax dwarf galaxy. Credit: ESO/Digitized Sky Survey 2. Top right: Optical image of the Sculptor dwarf galaxy. Credit:ESO/Digitized Sky Survey 2. Bottom images are corresponding count maps from the Fermi Large Area Telescope.
Figures 1.1a, 1.2, 1.3, and 4.2 used with permission.

ISBN 978-91-7649-224-6 (pp. i–xxii, 1–120)

Printed by Publit, Stockholm, Sweden, 2015.

Typeset in pdfLaTeX

Abstract

In this thesis I present our recent work on gamma-ray searches for dark matter with the Fermi Large Area Telescope (Fermi-LAT). We have targeted dwarf spheroidal galaxies since they are very dark matter dominated systems, and we have developed a novel joint likelihood method to combine the observations of a set of targets.

In the first iteration of the joint likelihood analysis, 10 dwarf spheroidal galaxies are targeted and 2 years of Fermi-LAT data is analyzed. The resulting upper limits on the dark matter annihilation cross-section range from about 10^{-26} cm^3 s^{-1} for dark matter masses of 5 GeV to about 5×10^{-23} cm^3 s^{-1} for dark matter masses of 1 TeV, depending on the annihilation channel. For the first time, dark matter models with a cross section above the canonical thermal relic cross section ($\sim 3 \times 10^{-26}$ cm^3 s^{-1}) are strongly disfavored by a gamma-ray experiment. In the second iteration we include 15 dwarf spheroidal galaxies in the combined analysis, employ 4 years of data and an improved calculation of the dark matter density. The obtained upper limits range from about 10^{-26} cm^3 s^{-1} for dark matter masses of 2 GeV to about 10^{-21} cm^3 s^{-1} for dark matter masses of 10 TeV, depending on the annihilation channel.

I briefly describe some of the evidence for dark matter, the Fermi-LAT instrument and public data releases, dwarf spheroidal galaxies, likelihood analysis, and results from analyses of Fermi-LAT data. I also document some of the tests made to verify the method and to compare different analysis setups.

Keywords: dark matter, Fermi-LAT, dwarf spheroidal galaxies

But there's no sense crying
over every mistake.
You just keep on trying
till you run out of cake.

GLaDOS

Publications included in the thesis

Paper I M. Ackermann, M. Ajello, A. Albert, et al.. *Constraining Dark Matter Models from a Combined Analysis of Milky Way Satellites with the Fermi Large Area Telescope*, Phys. Rev. Lett. **107**, 241302 (2011) 10.1103/PhysRevLett.107.241302.

Paper II M. Ackermann, A. Albert, B. Anderson, et al.. *Dark matter constraints from observations of 25 Milky Way satellite galaxies with the Fermi Large Area Telescope*, Phys. Rev. D **89**, 042001 (2014) 10.1103/PhysRevD.89.042001.

Publications not included in the thesis

M. Llena Garde, J. Conrad, J. Cohen-Tanugi, for the Fermi-LAT collaboration, M. Kaplinghat, G. Martinez. *Constraining Dark Matter Signal from a Combined Analysis of Milky Way Satellites with the Fermi-LAT*, Fermi Symposium proceedings **eConf C110509**, (2011) arXiv:1111.0320 .

M. Llena Garde, on behalf of the Fermi-LAT Collaboration. *Constraining dark matter signal from a combined analysis of Milky Way satellites using the Fermi-LAT*, Proceedings from Identification of Dark Matter 2010 conference **Proceedings Of Science**, (2011) arXiv:1102.5701 .

B. Anderson, J. Chiang, J. Cohen-Tanugi, J. Conrad, A. Drlica-Wagner, M. Llena Garde, S. Zimmer for the Fermi-LAT Collaboration. *Using Likelihood for Combined Data Set Analysis*, Fermi Symposium proceedings **eConf C14102.1**, (2015) arXiv:1502.03081 .

S. Zimmer, M. Llena Garde, J. Conrad et al. . *Search for Dark-Matter-induced gamma rays from Galaxy Clusters*, In Preparation , (2015) .

Contents

Acknowledgments

First and foremost, I would like to thank my advisor, Jan Conrad, for his work and support during these years. He has been a great advisor, and will certainly continue his successful career a lot further up the ladder. I also want to thank Joakim Edsjö and Lars Bergström for helpful advice, kind words, and support at conferences.

Thank you Stephan for all the help with code and software. Thank you Joel for the friendship and for the entertaining coffee breaks. Thanks to my office mates during the years (Anders, Joachim, Hugh, Manuel, Knut, Calle), and to colleagues (Antje, Brandon, Christian, Pat, Rickard, Sofia, Tanja) for the great atmosphere.

I would like to thank Vetenskapens Hus (House of Science) for the best teaching hours a PhD student could ever wish for. I had a lot of fun working with you, Cecilia Kozma, Tanja Nymark, Stefan Åminneborg, and Mark Pearce (KTH).

I am very grateful to Sara Rydbeck, Barbro Åsman and Staffan Bergwik for starting the well-needed course "Physics and Gender". Thanks for letting me join in as teaching assistant.

I would also like to thank my student, Saga, for trying out new lab exercises and helping with the paper satellite.

Finally, I would like to thank my family and friends for keeping me sane during this process, especially Peter and Alvin. I would not have made it through without you.

Svensk sammanfattning

Vi känner endast till en bråkdel av hur vår värld fungerar. Kända objekt som till exempel stjärnor, planeter, gasmoln och svarta hål utgör endast ungefär 5% av universum, men resten är osynligt, 27% i form av okänd materia och resterande 68% i form av ett okänt energislag. Eftersom vi inte kan se dessa okända delar refererar vi till dem som ”mörka”.

Dessa komponenter kan inte observeras i sig själva, men vi kan se hur den mörka energin påskyndar universums expansion och hur den mörka materian påverkar sin omgivning genom gravitationell växelverkan. Vi kan till exempel mäta rotationshastigheter hos galaxer, beräkna gravitationspotentialen samt jämföra den därigenom beräknade massan med den synliga massan, och på så vis se hur galaxerna domineras av mörk materia.

Den populäraste teorin kring den mörka materian är att den består av partiklar som interagerar via svag växelverkan, och därmed varken avger eller reflekterar elektromagnetisk strålning. Ett möjligt sätt att detektera mörk materia är att iaktta hur partiklarna annihileras (alternativt sönderfaller) genom att detektera de sekundära partiklar som bildas i processen, till exempel positroner, neutriner eller fotoner i form av gammastrålning.

Vi har använt data från det rymdbaserade gammastrålningsteleskopet *Fermi Gamma-ray Space Telescope* (ett samarbetsprojekt mellan NASA och flera nationer, däribland Sverige) för att försöka detektera mörk materia i sfäriska dvärggalaxer.

Sfäriska dvärggalaxer är några av de mest mörk-materiedominerade objekten i universum. De lämpar sig utmärkt för att undersöka mörk materia med hjälp av gammastrålning, eftersom de inte visar tecken på att besitta andra astrofysikaliska processer som ger upphov till just gammastrålning. De sfäriska dvärggalaxer som omringar vår galax är dessutom relativt närliggande och många är belägna långt ifrån vintergatans

spiralarmar vilket gör att observationerna har låg galaktisk förgrund. Många av dvärggalaxerna har även väl uppmätta egenskaper, till exempel hastigheter och positioner för deras stjärnor, vilket gör att vi kan uppskatta mängden mörk materia i dessa objekt samt hur den är fördelad.

Vi har introducerat en ny analysmetod, som gör det möjligt att kombinera observationer av fler dvärggalaxer i en gemensam analys. Eftersom partikelmodellen för mörk materia är densamma överallt (även om astrofysikaliska egenskaper, såsom densitet, beror på källan) kan vi inkludera flera mörk-materiekällor i en gemensam statistisk analys, där vi gör en intervallskattning av parametrarna för en vald partikelmodell. Detta gör att vi baserar vår mätning på en större mängd data än om vi skulle analysera varje källa individuellt, vilket reducerar de statistiska osäkerheterna.

I vår första publikation analyserade vi två års data och kombinationen av 10 dvärggalaxer, och i vår efterföljande publikation inkluderade vi 15 dvärggalaxer i den kombinerade analysen och analyserade fyra års data (vi analyserade totalt 25 dvärggalaxer, men några uteslöts ur den kombinerade analysen på grund av brist på uppmätta astrofysikaliska parametrar och överlappande analysregioner). Vi detekterade ingen signifikant gammastrålning från dessa galaxer, men kunde beräkna övre gränser för annihileringstvärsnittet hos flera mörk-materiemodeller. De övre gränser vi får från dessa analyser är mer robusta och mer uteslutande än motsvarande gränser från andra jämförbara analyser, och vi utesluter modeller med annihilleringstvärsnitt lägre än 3×10^{-26} cm^3 s^{-1} för låga partikelmassor (till exempel massor lägre än 10 GeV om partiklarna annihilerar via b-kvarkar).

Vår kombinerade analysmetod har använts av andra forskargrupper och har numer blivit en standardmetod för att analysera dvärggalaxer och galaxhopar.

Abbreviations

ACD	Anti-Coincidence Detector
ACT	Air Cherenkov Telescope
b	Galactic latitude
CI	Confidence Interval
CL	Confidence Level
DES	Dark Energy Survey
DM	Dark Matter
dSph	Dwarf Spheroidal galaxy
Fermi-LAT	Fermi Large Area Telescope
1FGL	First Fermi-LAT source catalog
2FGL	Second Fermi-LAT source catalog
3FGL	Third Fermi-LAT source catalog
IRFs	Instrument Response Functions
l	Galactic longitude
LL	Lower Limit
MC	Monte Carlo
MLE	Maximum Likelihood Estimate
NFW profile	Navarro-Frenk-White profile
PDF	Probability Density Function
ROI	Region Of Interest
SDSS	Sloan Digital Sky Survey
TS	Test Statistic
UFD	Ultra-Faint Dwarf galaxy
UL	Upper Limit
WIMP	Weakly Interacting Massive Particle

Preface

Thesis plan

This thesis is divided into three parts: Part I gives an introduction to the field and to my work, Part II is an appendix describing work for a publication that is not included in the thesis, and Part III provides the included publications.

In Part I, I document some of the tests that we did not explain in the publications, but that are important for understanding the development of the method, and I try to explain the evolution of the method through the different iterations of the Fermi-LAT dwarf galaxy analyses. In Chapter 5 I collect some tests verifying the statistical method, and in Chapter 7 I collect some of the many tests that were made developing the analysis in Paper I and compare the analysis in Paper I with that of Paper II. This thesis was written with the hope that it woud be easy to read for new PhD students giving an insight to the joint likelihood method and a summary of dwarf galaxies and the Fermi-LAT. Part of the text relies on the work made for my Licentiate thesis.

Contribution to publications

Paper I

For Paper I, I did all Fermi-LAT data analysis and verifications (including writing the scripts for the analysis, from data selection to the final plots) and I drafted most of the paper (not the paragraph *J factors from stellar velocity data*, which was written by L. Strigari, M. Kaplinghat, and G. Martinez). All contact authors (J. Conrad, J. Cohen-Tanugi and I) collaborated in discussing methods, results, and conclusions, and revising the manuscript.

The idea behind the *CompositeLikelihood* and *Composite2* codes came from J. Conrad, and the codes were written by J. Chiang and J. Cohen-Tanugi, but I did verification and debugging. I also constructed many tests to verify the method, including making simulations and testing real data. A selection of these tests are presented in this thesis.

I helped many Fermi-LAT collaboration members getting started using the joint likelihood method and the *CompositeLikelihood* and *Composite2* codes.

I presented our work at IDM 2010 in Montpellier and at the Fermi Symposium 2011 in Rome, and wrote the conference proceedings. I also presented at TeVPA in Stockholm, gave an invited talk at SciNeGHE in Lecce, and a seminar at McGill University in Montreal.

Paper I was chosen for an APS Physics Synopsis and listed as the Physical Review Letters Editor's Suggestion.

Paper II

For Paper II I took part in the planning and outline of the paper and I made an independent supplementary analysis using the pipeline developed for Paper I.

Paper II was chosen for an APS Physics Synopsis.

Publications not included in the Thesis

For the paper *Search for Dark-Matter-induced gamma rays from Galaxy Clusters* (in preparation), I developed and wrote the code for the selection of galaxy clusters. This work is described in the Appendix. I also performed tests on the pipelines and made a comparison with older work.

For the conference proceeding *Using Likelihood for Combined Data Set Analysis*, I was involved in the planning and discussion.

All papers were published using my birth name, Maja Llena Garde.

Maja Garde Lindholm
Stockholm, August 2015

Part I

Introduction

Chapter 1

The dark side of the universe

Although we have learned a lot about how nature works during the last centuries, we really only know about 5 percent of our universe [47, 48]. That is the part that consists of particles we have observed and can explain by theory. The rest of our universe is unknown and invisible, so it is referred to as dark. About 27 percent consists of some kind of matter that neither reflects nor emits electromagnetic radiation, and since it is invisible, it has been named dark matter (DM), in contrast to the visible, luminous matter. The remaining 68 percent consists of an unknown energy, called dark energy, that accelerates the expansion of the universe.

The last few years have been interesting times for Particle Physics and Cosmology. There have been some major leaps forward, maybe the most significant being the discovery of the Higgs boson announced at CERN in July 2012 [17, 92], supporting the theory explaining why particles have mass. But there has also been improvements in how well we know the composition of the universe. As the Planck mission released its results in March 2013 [47], the estimation of the amount of DM in the universe in proportion to dark energy and ordinary matter, increased from the about 23 percent determined by the Wilkinson Microwave Anisotropy Probe (WMAP) mission [127] to about 27 percent. This was confirmed by the 2015 Planck results with increased precision [48].

The search for DM has reached the theoretically suggested parameter regions, and we are closing in on finding out what this mysterious matter really is.

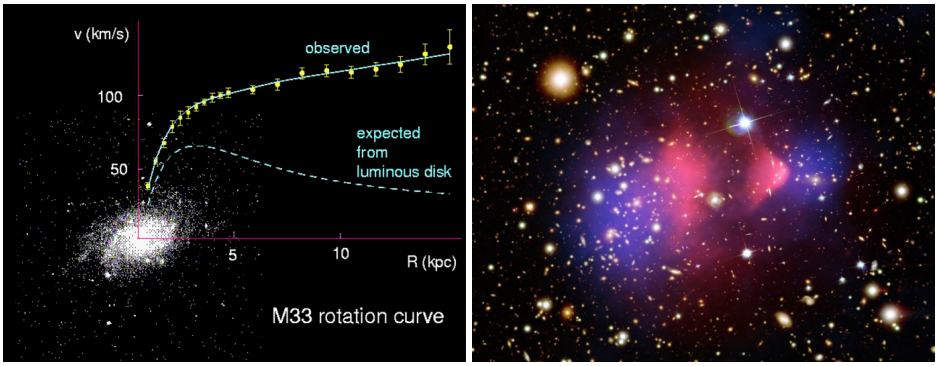

Figure 1.1: Two examples of observations that indicate the existence of DM. Left panel: Rotation curve of the nearby galaxy M33, where the measured rotation curve is noticable flatter than the expected rotation curve from luminous matter, indicating a DM halo. Figure from: Lars Bergström [76], rotational curve from [100] overlaid an optical image from NED [15]. Right panel: The Bullet cluster. The X-ray data showing the location of the gas is plotted in red and the lensing data showing the location of the mass is plotted in blue. Image credit: NASA, X-ray: NASA/CXC/CfA/Markevitch [154]; Lensing Map: NASA/STScI; ESO WFI; Magellan/U.Arizona/Clowe et al. [96] Optical: NASA/STScI; Magellan/U.Arizona/Clowe et al. [96].

1.1 Evidence for dark matter

The first indications of DM came from clusters of galaxies, where it was observed that the clusters are very heavy compared to their luminosity. The first observations were thought to have been presented by Zwicky in 1933, where he used the Doppler effect to measure the velocity dispersion for member galaxies of the Coma galaxy cluster. Using the Virial theorem connecting the total mass of the galaxy cluster to the averaged square of the velocities of the individual galaxies, he realized a large density of "dunkle Materie", dark matter, had to be allowed to theoretically explain the large velocity dispersion. But recent discoveries shows that this was actually first observed by Knut Lundmark at Lund University where he, three years before Zwicky, discussed the relation between luminous and dark matter (presented by Lars Bergström at a recent workshop [77] based on the original publication [151]. Lundmark might also have been

the first person to find observational evidence for the expansion of the universe [193]). The phenomenon was again observed in 1936 by Smith, who studied the Virgo cluster [191], and this was acknowledged by Zwicky in the updated English version of his work from 1937 [222], but it was not until the effect was observed in spiral galaxies by Rubin et al. [183], where it was concluded that a significant amount of the mass was located at large radii and that non-luminous matter exists beyond the luminous galaxy, that the ideas of Lundmark (or Zwicky) were finally accepted.

An example of measured rotational curves can be seen in the left panel of Fig. 1.1, where the rotational curve of the galaxy M33 is plotted on top of an optical image of the same galaxy. The radial velocity is much larger than what would be expected if the gravitational potential of the galaxy only came from its stars, and it is not declining at large radii as would be expected from luminous matter only. This implies a large DM halo extending beyond the stellar disk.

Another example of evidence for DM is the Bullet cluster, shown in the right panel of Fig. 1.1. In this image we see two colliding galaxy clusters, and by using data from X-ray telescopes and data from gravitational lensing observations, it was shown that the mass distribution is not the same as the distribution of gas [96]. The figure shows how the ordinary matter from one galaxy cluster has collided with the ordinary matter from the other galaxy cluster, giving rise to the typical ballistic shape of the gas cloud to the right (plotted in red). This shape arises from the friction when the two clouds pass through each other. The DM halos, detected through gravitational lensing (plotted in blue), are unaffected by the collision as they have just passed through without any interaction with neither the gas nor each other, implying that they consist of matter that is effectively collisionless (but interact gravitationally).

The large-scale structures of the universe, i.e. the distribution of galaxies and galaxy clusters, also gives an indication of the existence of DM. So called "N-body simulations" simulate how these structures form, and to recreate the universe as we know it, the simulations need DM. Examples of N-body simulations are the Aquarius [192] and Via Lactea II [104] simulations. Both are high-resolution simulations of DM halos the size of the Milky Way, finding a large amount of subhalos and smaller DM clumps, and giving indications of the shape of the Milky Way DM halo and its subhalos. These simulations rely on the cosmology for cold DM (i.e. non-relativistic at "freeze-out" as will be discussed in the next

section) and an expanding universe with dark energy included as a cosmological constant, Λ, referred to as ΛCDM cosmology.

1.2 Weakly interacting massive particles

One of the leading candidates for DM is weakly interacting massive particles (WIMPs). WIMPs are non-baryonic and neutrally charged particles, and predict the observed dark matter density as described below.

After the Big Bang, the particles were in chemical and thermal equilibrium, where chemical equilibrium means that every reaction between the particles is balanced by the reverse reaction (e.g. WIMP annihilation being balanced by WIMP creation through pair-production), so that the system as a whole does not change. This was maintained until the temperature of the universe became lower than the particle mass, and spontaneous pair-production stopped. When equilibrium can no longer be maintained, the abundance drops due to annihilation until the the annihilation rate falls below the expansion rate of the universe. This is called the "freeze-out", because the interactions maintaining the equilibrium "freeze out" and the particle abundance "freezes in". The relic abundance of a particle will depend on its annihilation cross section, as illustrated in the left panel of Fig. 1.2. This process can be expressed by the Boltzmann equation as [138]

$$\frac{dn_\chi}{dt} + 3Hn_\chi = \langle \sigma_{\text{ann}} v \rangle \left(n_{\chi,eq}^2 - n_\chi^2 \right) \tag{1.1}$$

where $H \equiv \dot{a}/a$ is the Hubble constant defining the expansion rate of the universe (a being the scale factor and $\dot{a} = da/dt$). n_χ is the actual number density of the particle and $n_{\chi,eq}$ is the equilibrium number density. $\langle \sigma_{\text{ann}} v \rangle$ is the thermally averaged annihilation cross-section summed over all annihilation channels. Averaging over the temperature is needed since the particles have random thermal directions and velocities.

To obtain a value for the relic number density of any particle, the Boltzmann equation can be solved numerically. Detailed numerical calculations (see eg. [138, 76]) give a value for the energy density, $\Omega_\chi h^2$, for a particle in the weak-scale mass range corresponding to

$$\Omega_\chi h^2 \sim 0.1 \frac{3 \times 10^{-26}\,\text{cm}^3\,\text{s}^{-1}}{\langle \sigma_{\text{ann}} v \rangle} \tag{1.2}$$

Using this relation, the observed relic dark matter density will give a value for $\langle \sigma_{\text{ann}} v \rangle$ in the same order as weak-scale interactions (a WIMP with a

mass of 100 GeV will e.g. predict a relic abundance that coincides within a factor 3 [99] of the most recent Planck result [48]). The correspondence that the WIMP, only by being a stable weakly interacting particle, predicts the observed relic DM density, is often referred to as the "WIMP miracle".

The thermal relic abundance calculation for a generic WIMP has been revisited recently by Steigman et al. [194]. The resulting annihilation cross section is plotted in the right panel of Fig. 1.2 compared to the resulting upper limits from Paper I and others, where this new relic abundance calculation is less in tension with the experimental results.

1.3 Other dark matter candidates

There are several DM candidates besides WIMPs, both other exotic particle models and baryonic and gravitational models. Here a subset is briefly described.

Axions were introduced to solve the problem that CP violation only arises in weak interactions and not in strong interactions (CP being the combined action of charge conjugation and parity). Axions are hypothetical neutral and very light particles, that interact weakly with ordinary matter. Axions and axion-like particles could behave as cold DM [76], and are predicted to convert to photons in magnetic fields. This photon mixing could be detected. The CERN Axion Solar Telescope (CAST) [219], uses magnetic fields to search for solar axions converting to photons in the detector, and with a non-detection the CAST collaboration set limits on the axion-photon coupling [60]. But this effect could also be detected with e.g. gamma-ray telescopes, since it would distort the spectra from astrophysical sources (as will be briefly discussed in Section 2.3).

An example of a model for DM that does not rely on unknown particles is the theory of MACHOs (MAssive Compact Halo Objects), introduced in 1986 by Paczynski [174], where he suggested using micro-lensing in order to detect dark objects in our galaxy consisting of non-luminous or dim objects, e.g. planets or black holes. The technique is applicable and the model is testable, and MACHOs have been ruled out as being a dominant DM halo contributor [54].

Another example is primordial black holes, i.e. black holes that are created due to large density fluctuations in the early universe. Primordial black holes span a large mass range, and even though the smallest (masses below 10^{15} g) would have evaporated through Hawking radiation

by now, the larger primordial black holes could be a DM candidate, either behaving as cold, non-baryonic matter or as MACHOs [88]. No detection has been made, but the obtained limits can be used to constrain models of the early universe involving e.g. inflation [88].

Instead of trying to explain what DM consists of, the theory of Modified Newtonian Dynamics (MOND) tries to explain the flat rotation curves of galaxies and galaxy clusters with a modified theory for gravity [163]. It does, however, not explain other evidence for DM, e.g. the Bullet cluster [96], and does not give a full description of the evolution of the universe and the growth of large scale structure as does ΛCDM cosmology.

1.4 How, and where, to search for dark matter

There are ways to detect the invisible. If the dark matter consists of WIMPs, then these particles can self-annihilate into standard model particles. For example, two WIMPs can annihilate into a quark-antiquark pair which then decay and give rise to other standard model particles, as illustrated in Fig. 1.3. The WIMPs could also annihilate into lepton pairs, like muon-antimuon pairs or electron-positron pairs, and to boson pairs like Z^+Z^- or W^+W^-. So even though the WIMPs are invisible to us, these standard model particles can be detected, and the measured particle spectra from these particles will give information about the original DM particle.

The method to search for the annihilation (or decay) products instead of the DM particle itself is referred to as indirect detection, and there are several (ongoing and planned) indirect detection experiments.

There are both space-based and ground-based gamma-ray observatories. Examples of space based observatories are the Fermi Large Area Telescope (Fermi-LAT), which will be discussed in detail in Chapter 3, AGILE (Astro-rivelatore Gamma a Immagini Leggero [178]), and the planned Gamma-400 [113]. Examples of ground based Air Cherenkov Telescopes (ACTs) are H.E.S.S. (High Energy Stereoscopic System [52]) in Namibia, the MAGIC (Mayor Atmospheric Gamma-ray Imaging Cherenkov [55]) telescope in La Palma, and the planned CTA (Cherenkov Telescope Array [46]).

While the space based telescopes detect the gamma rays directly through pair production within the detector, the ACTs use the atmosphere as part of the detector and detect the Cherenkov light from the air showers produced when the gamma ray interacts with the atmosphere.

The ACTs reach higher energies than the space based telescopes and have a large collecting area, but have to account for atmospheric distortions and will only cover one hemisphere.

Recent results from PAMELA (Payload for Antimatter Matter Exploration and Light-nuclei Astrophysics) [49, 50] show an excess in the positron fraction. This could be interpreted as a hint of dark matter (see e.g. [78]), but it could as well be explained by a population of pulsars [152]. The Alpha Magnetic Spectrometer (AMS-2) on the International Space Station has also detected an excess in the positron fraction confirming the results from PAMELA [30]. Even though designed to be a gamma-ray telescope, Fermi-LAT can detect charged particles and results presented by the Fermi-LAT collaboration [25] show an excess in the electron-positron spectra at energies from under 100 GeV to above 1000 GeV. The Fermi-LAT team also confirmed the positron excess reported by PAMELA [38]. Since the Fermi satellite (described in Chapter 3) does not have an on-board magnet to distinguish between electrons and positrons, this study uses the Earth magnetic field. By looking close to the Earth, the Earth itself will shield away electrons or positrons depending on where in the magnetic field the satellite is situated.

There are also ongoing dark matter searches with neutrino telescopes, such as IceCube [32] and ANTARES [51]. The IceCube collaboration has e.g. looked for muon-neutrino signals from annihilating dark matter in nearby galaxies and galaxy clusters, in the Galactic center, in the Sun, and in the Galactic halo [21, 22, 23, 24].

Another way to search for dark matter is to try to detect the dark matter particles directly, referred to as direct detection. The Milky Way should have enough dark matter for this to be possible as the Earth journeys through the Milky Way halo. The direct detection experiments try to detect dark matter by measuring the nuclear recoil when particles hit the detector material through either ionization, scintillation, or vibrations (phonons), so they need a very clean detector material to distinguish a possible signal from background. The detector usually consists of a very pure crystal (as in e.g. CDMS [1], DAMA [2], CRESST [3]) or liquid nobel gas such as Xenon (Xenon100 [4]). Since the dark matter interaction cross section is predicted to be very small, large detectors are needed (e.g. the Xenon100 contains 100kg liquid Xenon), but the detectors are still compact compared to satellites and ACTs (the Fermi-LAT calorimeter weighs $\sim$ 1800 kg [62]). It is also very important to keep the particle backgrounds as low as possible. The most common setup for

direct detection experiment is to choose a site underground to minimize the cosmic-ray background. Some experiments claim detection, such as DAMA/Libra that reports an annual modulation signal with a 8.9σ confidence level [80], and CRESST that report a possible 4σ detection [58] (but this is not confirmed by the upgraded CRESST experiment [59]). Other experiments present limits and preferred regions in the mass vs. interaction cross-section parameter space.

There is also the possibility of creating DM in particle colliders. With the start of Large Hadron Collider (LHC) Run 2, the collider searches for DM enter a new era. The two main experiments at LHC, ATLAS [16] and CMS [91], restarted after an upgrade and maintenance shutdown, and with increased energy (almost double its previous energy) there is the possibility of discovering new physics. The search for DM is one of the primary targets for LHC Run 2, for both ATLAS and CMS [28]. There have been earlier DM searches by these experiments, but so far, no detection has been made (e.g. [18, 19, 20, 140, 141]).

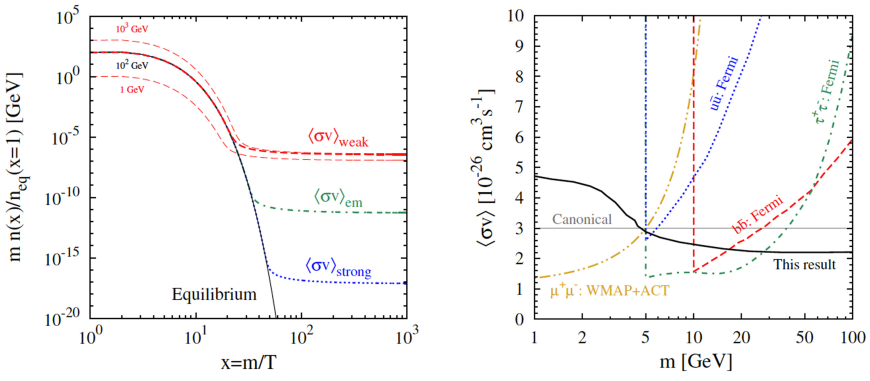

Figure 1.2: In the left panel the freeze-out of a massive particle is illustrated in terms of normalized mass density as a function of mass over temperature. The freeze-out of a particle with three different masses (1 GeV, 100 GeV and 1000 GeV) and an annihilation cross-section on the weak scale (here $\langle\sigma_{\rm ann}v\rangle = 2\times10^{-26}{\rm cm}^{-3}{\rm s}^{-1}$) is plotted in dashed red. For a particle with a mass of 100 GeV, electromagnetic scale interactions (here $\langle\sigma_{\rm ann}v\rangle = 2\times10^{-21}{\rm cm}^{-3}{\rm s}^{-1}$), and strong-scale interactions (here $\langle\sigma_{\rm ann}v\rangle = 2\times10^{-15}{\rm cm}^{-3}{\rm s}^{-1}$) are also plotted (dot-dashed green and dotted blue respectively), and the evolution of the equilibrium abundance is plotted in solid black. In the right panel observed limits from Fermi-LAT dSph analyses and constraints from reionization and recombination using WMAP and Atmospheric Cherenkov Telescopes for observations of the Cosmic Microwave Background are plotted together with the recent calculation of the thermal relic abundance from Steigman et al. (solid black) and the commonly used value of $3\times10^{-26}{\rm cm}^3{\rm s}^{-1}$ (solid gray). Figure credit: Stiegman et al. Reprinted figure with permission from [194] Copyright 2012 by the American Physical Society. Fermi limits from Paper I and [118]

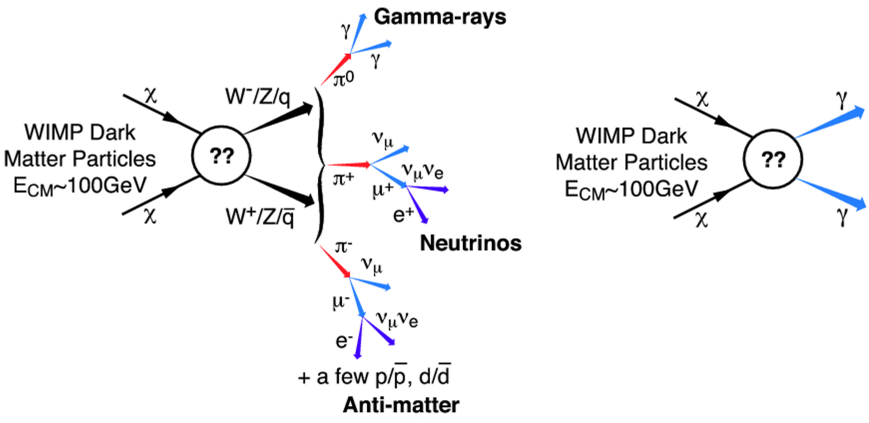

Figure 1.3: A schematic illustration of WIMP dark matter self-annihilating into standard model particles. Figure credit: Baltz et al. [63]. ©SISSA Medialab Srl. Reproduced by permission of IOP Publishing. All rights reserved.

Chapter 2

Gamma-ray searches for dark matter

2.1 The gamma-ray signal

As described in the previous Chapter, WIMP annihilation (or decay) give rise to standard model particles, and among these particles, gamma-ray photons are produced. The WIMPs could also annihilate into two gammas, a Z boson and a gamma, or possibly a Higgs boson and a gamma [134], and this would give a line feature in the spectrum. The fact that this line feature can not come from any other known astrophysical phenomena makes it so special that it is often referred to as the "smoking gun". The shape of the continuum gamma-ray spectra for different annihilation channels are compiled in Fig. 2.1, where the values originate from the DMFIT package [137] implemented in the Fermi Science Tools [5]. The gamma-ray yield in DMFIT was originally obtained using DarkSUSY [121], but DMFIT has been updated using Pythia 8.165 [190] and now includes more annihilation channels and covers a larger mass range (described in Paper II).

The gamma-ray flux from self-annihilating WIMPs can be expressed as

$$\Phi_{WIMP}(E,\psi) = \Phi^{PP}(E) \times J(\psi), \tag{2.1}$$

where $\Phi^{PP}(E)$ is the "particle physics factor" and $J(\psi)$ is the "astrophysical factor", or J-factor, in direction ψ [63]. The particle physics factor is described by

$$\Phi^{PP}(E) = \frac{1}{4\pi} \frac{<\sigma_{ann} v>}{2m^2_{WIMP}} \sum_f \frac{dN_f}{dE} B_f, \tag{2.2}$$

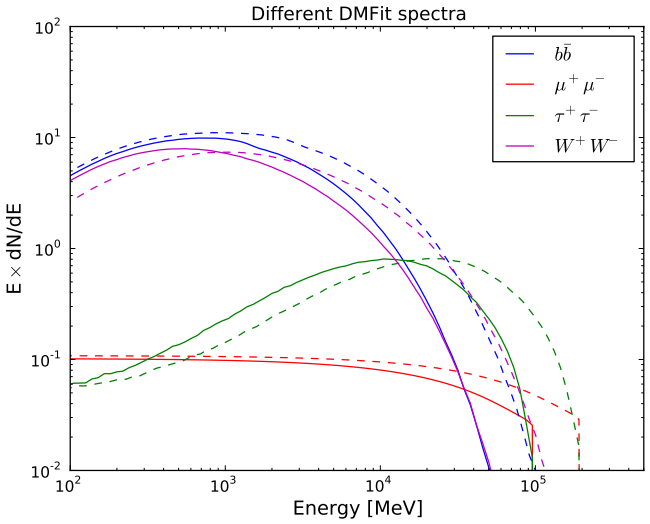

Figure 2.1: Examples of gamma-ray annihilation spectra from WIMPs with masses of 100 GeV (solid lines) and 200 GeV (dashed lines), annihilating through four different annihilation channels (the $b\bar{b}$ channel in blue, $\mu^+\mu^-$ channel in red, $\tau^+\tau^-$ channel in green, and W^+W^- channel in magenta). Values are obtained using the tables from the DMFIT package [137] implemented in the Fermi Science Tools [5].

where $\langle\sigma_{\rm ann}v\rangle$ is the velocity averaged WIMP annihilation cross section, m_{WIMP} is the WIMP mass, and $\sum_f \frac{dN_f}{dE}B_f$ is the gamma-ray spectrum generated per WIMP annihilation where the sum is over final states f with branching ratio B_f. As explained above, the particle physics factor has two main spectral features: the continuum feature and the line feature, but there might also be bump-like features from virtual internal Bremsstrahlung and final state radiation that we do not take into account here. The astrophysical factor is described by

$$J = \int_{l.o.s.,\Delta\Omega} \rho^2(r) dl d\Omega'. \tag{2.3}$$

Here, the integration is over the line-of-sight and the solid angle, $\Delta\Omega$, and $\rho(r)$ is the DM density distribution as a function of the radius from the center of the halo, r.

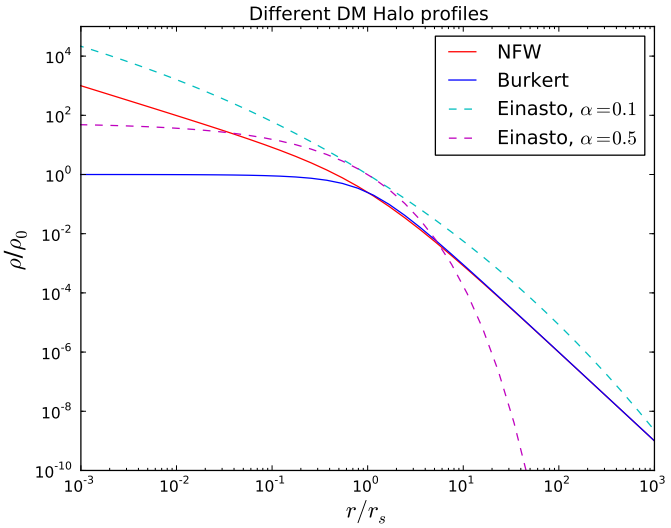

Figure 2.2: Different DM profiles plotted in arbitrary units and normalized to the scale density, ρ_0, and as a function of radius normalized to the scale radius, r_s. The NFW profile (solid red), and the Einasto profile with a low value for the index (dashed cyan), α, are cuspy while the Burkert profile (solid blue) has a constant density core. The Einasto profile with a higher value for the index (dashed magenta) is more cored than the Einasto profile with a low value for the index.

The DM density profile of galaxies is not known, but there are several profiles that fit N-body simulations, eg. the Navarro-Frenk-White (NFW) density profile [167], the Burkert profile [84], and the Einasto profile [110]. The NFW profile is defined as

$$\rho(r) = \frac{\rho_0 \, r_s^3}{r(r + r_s)^2}, \tag{2.4}$$

where ρ_0 is the scale density and r_s the is the scale radius where the profile changes shape, both of which vary for different halos. Similarly, the Burkert profile is defined as

$$\rho(r) = \frac{\rho_0 \, r_s^3}{(r_s + r)(r_s^2 + r^2)}, \tag{2.5}$$

and the Einasto profile defined as

$$\rho(r) = \rho_0 \exp\left\{\frac{-2((r/r_s)^\alpha - 1)}{\alpha}\right\}, \tag{2.6}$$

where α will alter the shape of the distribution. In Fig. 2.2 the NFW and Burkert profiles are plotted together with the Einasto profile for two different values of the index, α. The NFW profile is cusped while the Burkert profile has a constant density DM core. The shape of the Einasto profile depends on the index. It is still under debate whether the DM density profile is cored or cusped, and this will be discussed more in depth for dwarf spheroidal galaxies (dSphs) in Chapter 4.

2.2 Backgrounds

When analyzing gamma-ray data, there are two major components to the backgrounds; particles classified as gammas while they are not, and observed background such as point sources and Galactic foreground. Here I focus on Fermi-LAT analyses, where the particle background contamination is reduced in the data taking and event classification processes, and the gamma-ray background (including residual cosmic-ray contamination) is modeled (or e.g. masked or measured in a sideband).

The particle background is here defined as all events that are classified as gamma rays but originate from cosmic rays (or from cosmic-ray interactions in the Earth's atmosphere) [40]. Many cosmic rays are vetoed by the anti-coincidence detector (briefly described in Section 3.1), and many are correctly classified as cosmic rays in the event selection process.

Depending on the target of choice, different levels of cosmic-ray contamination can be accepted, and several event classes with different gamma-ray purity are prepared by the Fermi-LAT collaboration for internal and public use (See section 3.2). The residual cosmic-ray background contamination is included in the treatment of the gamma-ray backgrounds as described below.

The Fermi-LAT collaboration provides background models and source catalogs for the analysis of Fermi-LAT data. The background models consist of a Galactic diffuse emission template and an extragalactic isotropic diffuse emission template.

The Galactic diffuse emission template is a map containing a spatial and spectral part. The template is obtained by fitting inverse Compton

radiation maps predicted using GALPROP [199] and gamma-ray emissivities from gas density maps (divided in galactocentric rings to account for the non-uniform flux) to Fermi-LAT data in several energy bands together with known point sources and a model for isotropic diffuse emission [6, 170].

The isotropic template includes residual cosmic-ray contamination and unresolved point sources, and is fitted to the high-latitude sky (where the Galactic latitude, b, fulfills $|b| > 30^\circ$) together with the Galactic template and all known individual sources. Since the templates are degenerate (the isotropic template is adjusted to the Galactic template) it is of great importance to use the two templates together. Since the background models are derived by fitting to the Fermi-LAT data, each event class has a dedicated model due to the difference in residual cosmic-ray contamination.

Contamination from the Earth's albedo is reduced by making a zenith-angle cut when reducing the data. There is an Earth limb template for low energies (below 200 MeV) specific to the 2-year data set used in the development of the second Fermi-LAT catalog, 2FGL, and it should only be used for this data set [6]. There is also an updated version to be used with the 4-year data set used for the 3FGL [201].

With 4 years of data the Sun and the Moon needed to be taken into account in the development of the third Fermi-LAT catalog, 3FGL, and there are templates to be used with the corresponding dataset [201].

There have been several releases of source catalogs. The first iteration of the Fermi-LAT catalog (1FGL, [26]) used 11 months of data and contains 1451 sources, all modeled as power laws. For the second iteration (2FGL, [170]) there were several improvements, 24 months of data, higher resolution diffuse models, inclusion of extended and non-power-law sources, and an improved source association process. 2FGL contains 1873 sources. The most recent version is the 4-year catalog (3FGL, [201]) which contains 3033 sources, all plotted in Fig. 2.3.

Many of the catalog sources are identified as having known counterparts in other surveys, some are identified as new sources and are associated to a source class, while others remain unassociated. Examples of gamma-ray sources are blazars (and other active galactic nuclei), pulsars, supernova remnants, and X-ray binaries [201]. In searches for DM, pulsars are of special interest since the spectrum from pulsars resembles the DM spectra for some annihilation channels, both for gamma-rays and positrons. Both pulsars and DM have been suggested to explain the observed Galactic center gamma-ray excess [94, 176] and, as mentioned in

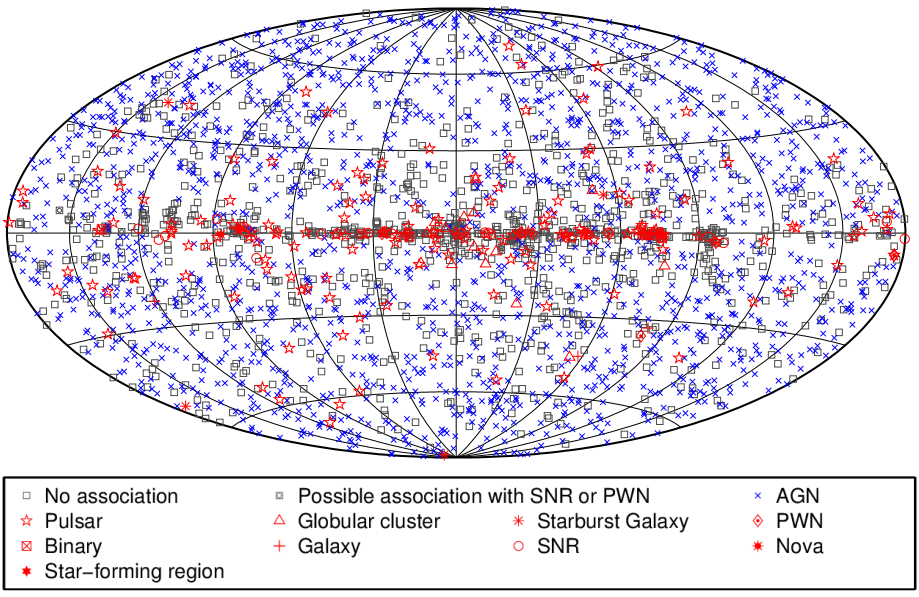

Figure 2.3: Sources in the third Fermi-LAT catalog (3FGL) plotted in Aitoff projection. Note that all active galactic nuclei are listed as AGN, regardless of category, supernova remnants are labeled SNR, and pulsar wind nebulae are labeled PWN. Figure credit: Fermi-LAT Collaboration [201].

Section 1.4, the rise in the positron fraction [78, 152].

2.3 Gamma-ray targets

There are many different places to look for DM with gamma rays, each with its own advantages and challenges.

The Galactic center is nearby and has a large concentration of DM, but the region is very complicated with many unknown gamma-ray sources and complicated diffuse gamma-ray emission from cosmic-ray interactions with interstellar radiation fields and gas, so the background modeling is therefore very complicated and the uncertainties are large. It is not clear whether the DM profile in the Galactic center is cusped or cored, leading to large DM modeling uncertainties [99]. A recent compilation of rotation curve measurements confirms the existence of DM in the inner galaxy

without assuming a specific DM distribution, but not even this compiled data is able to determine the shape of the DM profile [132].

Since the Galactic center is very challenging, an alternative is to search further out in the Galactic halo. The mass and shape of the halo is still uncertain, but the background is less complicated and the DM content is still high. The contribution to the diffuse emission by DM annihilating (or decaying) in the Galactic halo can be constrained and limits on the annihilation cross-section can be calculated, yielding results comparable to the results from dSphs but with much larger uncertainties involved [36].

Measurements of the high latitude isotropic diffuse emission can be used to constrain the total extragalactic isotropic DM signal (a combination of unresolved DM halo signals and possible Galactic subhalos). The resulting upper limits on the annihilation cross-section are comparable to, or more constraining than, the limits from dSphs for high DM particle masses (e.g. above $\sim 10^3$ GeV for the $b\bar{b}$ annihilation channel) [202]. The mentioned large uncertainty in the Galactic DM profile, the unknown properties of the unresolved DM halos, unresolved sources, and other sources of diffuse gamma-ray emission will, however, make it difficult to distinguish a possible signal [99].

Other interesting targets are galaxy clusters, since they are considered to be DM dominated systems. Many are situated at high Galactic latitude resulting in a low Galactic foreground, but they have predicted gamma-ray flux from cosmic-ray scenarios and there might also be a significant contribution from dark matter substructure, resulting in large uncertainties in the astrophysical factors [34, 44, 177]. There is, however, a large number of galaxy clusters, and the DM analysis can benefit from a combined analysis as described in Chapter 5 [44, 217, 218].

Since the spectral line feature is such a distinct feature, there are no astrophysical uncertainties, but the statistics may be low, and instrumental features can be a problem. There has been indications of a line signal from the Galactic center (e.g. [208]), but the significance has decreased over time [209] and is not confirmed by the Fermi-LAT team [37, 42]. The origin of this signal is yet not identified.

N-body simulations predict a large number of small DM Milky Way satellites, but not many have been observed. Some of these satellites might only be detectable in gamma rays, with no counterparts in other wavelengths. A search for DM satellite candidates from unassociated Fermi-LAT sources in the first year of data taking did not result in any

detection [39].

Milky Way satellites, such as the dSphs, have very low backgrounds and are easy to identify, and they do not have as large uncertainties in the astrophysical factors (J factors) as galaxy clusters, since the DM content can be determined from stellar velocity data (as described in Section 4.3). In this thesis the main focus lies on dSphs and they will be described further in Chapter 4.

If the DM consists of axion-like particles, the detection possibilities for the Fermi-LAT, and other gamma-ray telescopes, are predicted to be good [128, 185], and there is ongoing work within the Fermi-LAT collaboration targeting neutron stars and the central radio galaxy of the Perseus cluster, but there are no official results yet [75, 172]. Some primordial black holes should have high enough temperature to emit gamma rays and could be detected with e.g. Fermi-LAT, but no detection has yet been made [153].

An essential part of the work presented in this thesis is that the particle physics part of the DM spectrum is universal, i.e. it does not depend on the target, but the astrophysical factor is target dependent. So, the fact that the particle physics factor is universal makes it possible to investigate many targets at the same time, using a joint likelihood analysis method. For example, in Paper I [35], we target 10 dSphs and in Paper II [43] we target 15 dSphs in a combined analysis. This method can be used on other sources as well, like e.g. galaxy clusters [44, 217], and it is applicable to any parameter that is universal for all targets. The method and some statistical verifications are described in Chapter 5.

Chapter 3

The Fermi Large Area Telescope

As described in the previous chapters, WIMP DM could self annihilate giving rise to different final products such as gamma rays, neutrinos, positrons, electrons, and anti-protons. Different annihilation channels give rise to gamma-ray spectra as shown in Fig. 2.1. These gamma-ray spectra are distinguishable from astrophysical sources and could be detected by gamma-ray telescopes. The cut-off energy for the gamma-ray photons depends on the WIMP mass, so a detector that covers lower energies is needed to search for light WIMPs, and a detector that covers higher energies is needed to search for heavy WIMPs. To distinguish between DM and other astrophysical sources, good energy resolution and good spatial resolution is important. Good sky coverage makes it possible to cover all possible targets. Since the predicted statistics for many targets is very low, it is important with a lot of observation time.

The Fermi Gamma-ray Space Telescope fulfills all these criteria and is an excellent instrument to use in the search for DM.

3.1 The instrument

The Fermi Gamma-ray Space Telescope was launched in June 2008. Its main instrument, the Large Area Telescope (Fermi-LAT) [62], is a pair conversion telescope with an energy range from about 20 MeV to above 500 GeV. The field of view is 2.4 sr at 1 GeV. The Fermi satellite orbits around the earth, and with 2 orbits (about 3 hours), the Fermi-LAT covers the full sky. Between August 2008 and December 2013, the Fermi Gamma-ray Space Telescope was in regular survey mode, but between

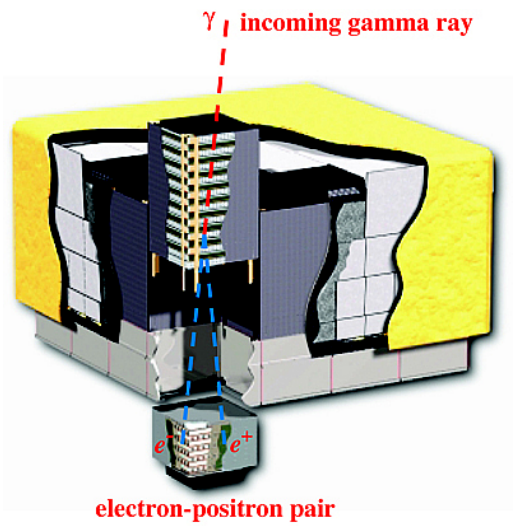

Figure 3.1: Illustration of the Fermi-LAT showing how an incoming gamma ray interacts in one of the towers, producing an electron-positron pair. The picture shows a converter-tracker tower separated at the top and a calorimeter separated at the bottom. The anti-coincidence detector is shown as light gray tiles under the yellow thermal blanket. Figure credit: Fermi-LAT Collaboration.

December 2013 and December 2014 a modified observing strategy was implemented giving increased coverage of the Galactic center while still covering the full sky. After this Galactic center biased survey mode, the observatory is now back at regular survey mode.

The Fermi-LAT measures $1.8 \times 1.8 \times 0.72$ meters and it consists of 16 identical modules containing a converter-tracker and a calorimeter. The telescope is covered with an anti-coincidence detector to veto charged particles. An illustration of an incoming event is shown in Fig. 3.1.

The converter-tracker consists of 12 thinner tungsten converter layers (front section) and 4 thicker tungsten converter layers (back section), interleaved with 16 silicon tracker planes. Tungsten is a high-Z material (high atomic number) that converts the gammas into electron-positron pairs. The thinner converter layers have better angular resolution and smaller Coulomb scattering effects than the thicker converter layers, while the thicker converter layers provide more converter material for high-energy gamma rays. Silicon is a semiconductor which is ionized when a particle passes through. In the silicon tracker planes in the Fermi-LAT,

the silicon strips are placed in different orientation (silicon strip detector) to be able to localize the event. The lower energy limit of the Fermi-LAT is set by the fact that it detects gamma rays through pair-production. In tungsten, the pair-production is dominant above 10MeV. At lower energies a significant fraction (about 50%) of the energy is deposited in the tracker (but the number of 'hits' in the tracker can still give an estimate of the energy deposited in the tracker). This is what sets the lower recommended energy limit for the Fermi-LAT (about 20 MeV). The high energy limit is mainly due to low statistics.

The Fermi-LAT calorimeter consists of 96 long narrow cesium-iodide scintillators stacked in eight layers. The scintillation blocks are read out by photodiodes. The scintillators are alternating in orientation so the location and spread of the shower can be determined. The direction of the incoming particle is determined so the calorimeter could serve as a tracker in it self, but with low resolution.

The anti-coincidence detector (ACD) consists of 89 individual plastic scintillator segments vetoing charged particles. The segmentation reduces self-vetoing arising from secondary particles that Compton scatter within the ACD, called backsplash, by only considering the veto signals from the ACD segment that the detected photon passed through [164].

On-board the Fermi-LAT there is also a data acquisition system and a trigger. The data acquisition system combines information from the different components to decide when a likely gamma ray has been detected and chooses what information to send to the ground. Some background rejection is made on-board by the anti-coincidence detector, but cuts reducing photons from the Earth albedo and correcting for the spacecraft rocking angle needs to be made when reducing the data.

3.2 Three generations of data

With increased knowledge of the behavior of the instrument in orbit, and more data, it is possible to improve the event reconstruction (how the directions and energies of the incoming gamma rays are recovered from instrument readout), the instrument response functions (IRFs), background models, and source catalogs. Therefore several versions of the data, referred to as Passes, have been released to the community. Every event is assigned a photon probability and reconstruction quality, which is used to organize the events in different data sets, referred to as event classes. The different event classes are recommended for different types of

analyses, ranging from data sets with high statistics but potentially high contamination from cosmic rays, to data sets with high gamma-ray purity but lower statistics. Each event class is paired with a corresponding set of IRFs. These IRFs consist of three parts; the instrument effective area (the detector efficiency), the Point Spread Function (PSF), and the energy dispersion (EDISP), and they describe the instrument performance as a function of, among other parameters, the photon energy, direction, and conversion point within the instrument (front or back).

Pass 6 was the first iteration of LAT data, using simulation-based IRFs (Pass6_V3 was derived using pre-launch based MonteCarlo generated photon samples, and was later updated to Pass6_V11 using knowledge gained during the time in orbit). The event classes were the high statistics but highly contaminated Transient class recommended only for short transient events (< 200s), the intermediate Diffuse class recommended for point source analyses and some bright diffuse sources, and the high gamma-ray purity DataClean class recommended for studies of diffuse emission. Due to rapid decrease of effective area and uncertainties in the IRFs, analyzing point sources at energies lower than 200 MeV was discouraged.

The Pass 7 data was released to the community in August 2011. For Pass 7, the event analysis was improved where on-orbit effects were taken into account in the data reduction. The event reconstruction algorithms were not changed, but new event classes were introduced, TRANSIENT, SOURCE, CLEAN, and ULTRACLEAN. The TRANSIENT class corresponds to the Pass 6 Transient class, the SOURCE class corresponds to the Pass 6 Diffuse class, the CLEAN class corresponds to the Pass 6 DataClean class, and the ULTRACLEAN class was designed for analysis of extragalactic diffuse gamma-ray emission by further reducing the residual cosmic-ray contamination [40]. In November 2013 a new version of Pass 7 was released, P7REP, where the entire dataset was reprocessed from scratch. This reprocessing was made to include new calibration constants [82]. The major differences compared to Pass 7 are a slight shift in the energy scale and an improved calorimeter reconstruction (where the expected degradation of the light yield and improvement of the position reconstruction were taken into account).

A comparison of the effective area in Pass 6 and Pass 7 is plotted in Fig. 3.2. The effective area describes how efficiently the Fermi-LAT detects gamma rays, and depends on the energy and incident angle of the photon. It is defined as the product of the cross-sectional geometrical col-

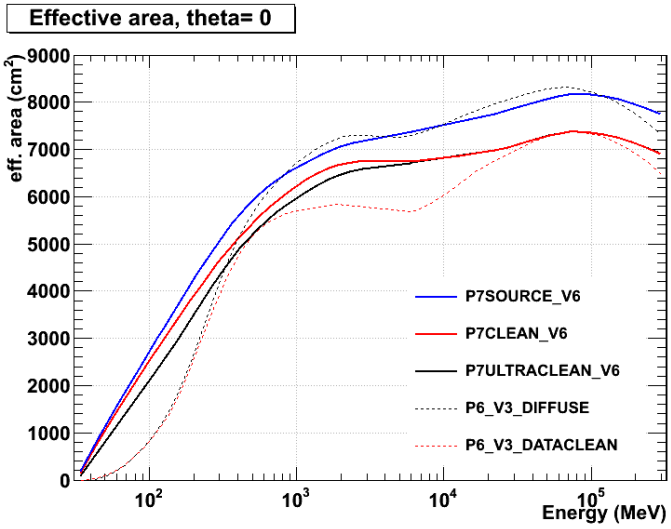

Figure 3.2: The effective area for Pass 6 and Pass 7 as a function of photon energy for different event classes and normal incidence photons ($\theta = 0$) averaged over all values of azimuthal angles. The event classes changed in Pass 7, and here P7SOURCE_V6 is to be compared with P6_V3_DIFFUSE, and P7CLEAN_V6 with P6_V3_DATACLEAN. Figure credit: Fermi-LAT Collaboration [33].

lection area, the probability for gamma-ray conversion, and the efficiency of the chosen event selection [40]. With Pass 7, the gain in effective area is noticeable both at low energies and mid-range energies.

Pass 8 is the latest iteration and was released in June 2015. It presents a radical revision of the entire event reconstruction process, using the knowledge gained during the years in orbit [61, 173]. There are e.g. improvements in the direction measurements, the energy measurements, the handling of ghost events, the event selection, and the instrument simulation. The event classes are divided into different subsets for different qualities of the directional reconstruction (four different PSF event types) and energy reconstruction (four different EDISP event types), in addition to the conversion point (two types, front and back), making it possible to further customize the dataset for a chosen analysis.

Chapter 4

Dark matter searches in dwarf galaxies

As mentioned in Chapter 2, dSphs are among the most dark matter dominated systems in the universe. Since they have a low content of gas and dust and no known gamma-ray sources, they are promising targets for gamma-ray searches for dark matter. They are also relatively near-by and many lie far enough from the Galactic plane to have low Galactic foreground. This makes them clean targets for gamma-ray searches with the Fermi-LAT.

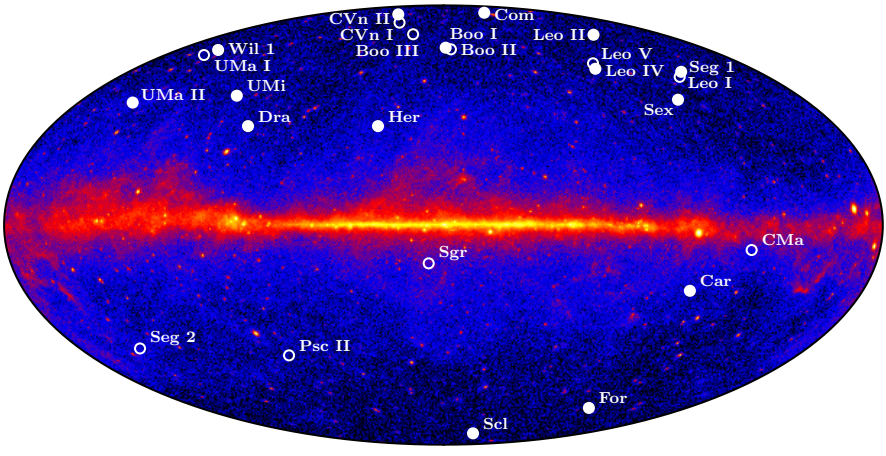

Figure 4.1: Locations of the 25 dSphs from Paper II plotted on top of a Hammer-Aitoff projection of a 4-year LAT counts map. The 15 dSphs included in the combined analysis are plotted as filled circles.

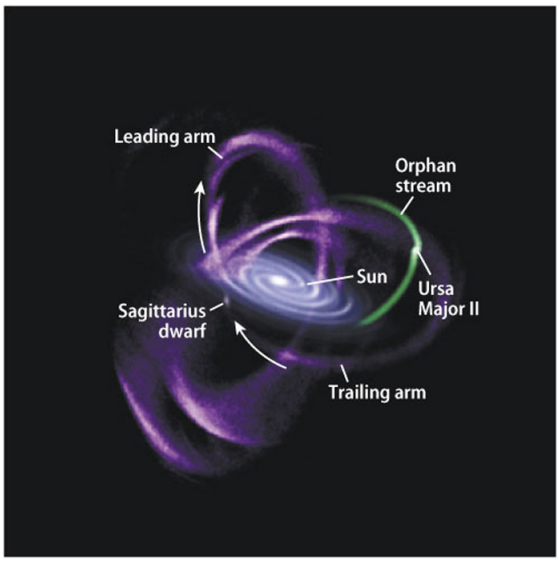

Figure 4.2: An illustration of the Sagittarius stream with its different arms that wrap around the Milky Way. Figure credit: Vasily Belokurov [68].

dSphs are usually divided into two groups: the 'classical' dSphs and the 'ultra-faint' dwarf galaxies (UFDs). The distinction between 'classical' dSphs and UFDs is not very well defined in intrinsic luminosity or sequence of discovery but here I follow the definition in [204]. The 'classical' dSphs are the brighter ones discovered before the Sloan Digital Sky Survey (SDSS) and they were mainly detected 'by eye', i.e. on photographic plates (except for Sagittarius). The UFDs are defined as the dSphs found in the SDSS, and in later surveys, as over-densities of individual stars. The positions of the known dSphs (the 9 'classical' dSphs and the 16 UFDs found in the SDSS) are shown in Fig. 4.1.

The dSphs have a wide range of metalicities showing signs of internal chemical evolution, meaning they are galaxies that at some stage hosted star formation. This can be compared to star clusters where the stars were formed in one single burst.

Whether the dSph DM profile is cored or cusp has been a source of debate (discussed in e.g. [196, 204]). In a recent paper by Martinez [157], briefly described in Section 4.3, cusped models are preferred over cored models for the full group of dSphs. This result does not make any statements about analyses of individual dSphs, as they can still prefer

cored models, e.g. caused by supernovae and tidal stripping. For example, Fornax and Ursa Minor show indications of a cored DM profile [56, 120, 144], while Sculptor has two stellar populations, both compatible with a cuspy profile [198].

In ΛCDM cosmology, there should, according to simulations, exist a large number of small satellites in the Milky Way halo. When only the 'classical' dwarfs were discovered, and even with the UFDs found in the SDSS, there were just not enough observed dSphs compared to theory [139, 189]. This has been referred to as the missing satellites problem, where some of the missing satellites may be dark satellites as mentioned in Section 2.3. With the new possible dSphs found in the Dark Energy Survey (described in Section 4.2) this problem is further reduced [67].

Since the dSphs are part of our local galaxy group, and lie within the galactic halo, they are subjects to interactions and tidal forces. Some dSphs are thought to be torn apart by the Milky Way and some may recently have collided with the disc or other systems. Many lie within stellar streams as illustrated in Fig. 4.2. Tidal disruption can e.g. create an unbound stellar population near a dSph, give rise to tidal tails, or create an observable velocity gradient i.e. that stars in different locations have different velocities, which may be an issue when e.g. determining the mass of the galaxy.

4.1 Summary of known dwarf galaxies

In this section, a summary of all known dSphs is compiled. In Table 4.1 the positions and distances for all known dSphs are listed, and where stellar velocity data is available, the J-factors (and their statistical uncertainties) are also listed together with the reference to the corresponding stellar velocity data. This list will increase significantly in the near future since new dSphs are being discovered, as will be discussed in the next section.

In Paper I we targeted the 10 dSphs that, at the time, had well determined J-factors and were not overlapping (Bootes I, Carina, Coma Berenices, Draco, Fornax, Sculptor, Segue 1, Sextans, Ursa Major II, and Ursa Minor). In Paper II all dSphs in Table 4.1 were targeted, but only a subset of 15 dSphs were included in the combined analysis due to overlaps and missing stellar data (Hercules, Canis Venatici II, Leo II, Leo IV, and Willman I, in addition to the dSphs analyzed in Paper I). The analyses are described in Chapter 6.

Name	l (deg)	b (deg)	Distance (kpc)	$\overline{\log_{10}(J^{NFW})}$ ($\log_{10}$[GeV^{2}cm^{-5}sr])	Reference
Bootes I	358.1	69.6	66	18.8 ± 0.22	[101]
Bootes II	353.7	68.9	42	–	–
Bootes III	35.4	75.4	47	–	–
Canes Venatici I	74.3	79.8	218	17.7 ± 0.26	[189]
Canes Venatici II	113.6	82.7	160	17.9 ± 0.25	[189]
Canis Major	240.0	-8.0	7	–	–
Carina	260.1	-22.2	105	18.1 ± 0.23	[206]
Coma Berenices	241.9	83.6	44	19.0 ± 0.25	[189]
Draco	86.4	34.7	76	18.8 ± 0.16	[165]
Fornax	237.1	-65.7	147	18.2 ± 0.21	[206]
Hercules	28.7	36.9	132	18.1 ± 0.25	[189]
Leo I	226.0	49.1	254	17.7 ± 0.18	[160]
Leo II	220.2	67.2	233	17.6 ± 0.18	[145]
Leo IV	265.4	56.5	154	17.9 ± 0.28	[189]
Leo V	261.9	58.5	178	–	–
Pisces II	79.2	-47.1	182	–	–
Sagittarius	5.6	-14.2	26	–	–
Sculptor	287.5	-83.2	86	18.6 ± 0.18	[206]
Segue 1	220.5	50.4	23	19.5 ± 0.29	[188]
Segue 2	149.4	-38.1	35	–	–
Sextans	243.5	42.3	86	18.4 ± 0.27	[206]
Ursa Major I	159.4	54.4	97	18.3 ± 0.24	[189]
Ursa Major II	152.5	37.4	32	19.3 ± 0.28	[189]
Ursa Minor	105.0	44.8	76	18.8 ± 0.19	[165]
Willman 1	158.6	56.8	38	19.1 ± 0.31	[213]

Table 4.1: Properties of Milky Way dwarf spheroidal satellite galaxies. Table adapted from Paper II . The reference is to the stellar data used to calculate the J factors using the method in [157] where stellar data is available, and the J factors are calculated over a solid angle of $\Delta\Omega \sim 2.4 \times 10^{-4}$ sr (corresponding to an angular radius of 0.5° which is larger than, or close to, the angular size of the dSphs).

Bootes I

Bootes I was discovered by Belokurov et al. in 2006 and it has very irregular density contours suggesting it to be tidally disrupted [69].

Bootes II

Bootes II was discovered in 2007 by Walsh et al. [207]. It lies close to both the leading and the trailing arm of the Sagittarius stream (see Fig. 4.2) and might be associated with them [146].

Bootes III

Discovered in 2008 by Grillmair et al. in the middle of the Styx stellar stream, Bootes III is possibly disrupting and may be the progenitor of the mentioned stream [122]. It has an irregular shape and is probably in the final transition from being a dSph to totally dissolve into the Styx stream [86].

Canes Venatici I

Discovered in 2006 by Zucker et al. [221].

Canes Venatici II

Canes Venatici II was discovered in 2006 by Belokurov et al. [71] and independently by Sakamoto and Hasegawa [184]. It is quite spherically symmetric, but there is evidence for extensions that may be part of streams or tails [71] .

Canis Major

Discovered by Martin et al. in 2003 [156], Canis Major seems to be disrupting and a major part of its matter might have been spread along its orbit. Its orbit lies very close to the Galactic Plane and it could even be considered a substructure of the plane itself [156].

Carina

This 'classical' dSph was discovered in 1977 by Cannon et al. [85]. It shows clear signs of tidal disruption [66].

Coma Berenices

Discovered in 2006 by Belokurov et al. [71], Coma Berenices seems to be a stable dSph with no signs of tidal stripping [166, 189], but with some substructure and an irregular and extended shape [71]. It lies on the edge of the Sagittarius Stream and might be associated with the leading arm (see Fig. 4.2) [73].

Draco

Discovered in 1955 by Wilson [214], this dSph is the most DM-dominated dSph among the 'classical' dSphs. It has a smooth stellar density profile and shows no signs of tidal disruption, and has even been called "a flawless dwarf galaxy" [200].

Fornax

This 'classical' dSph was the second to be discovered in 1938 by Shapley [187]. Battaglia et al [64] found three different stellar populations in Fornax: a young population in the center, a mid-aged population and an ancient population, all distinguishable from each other kinematically, from the metalicity distribution and in the spatial distribution. This could be a sign that Fornax has undergone a recent merger [64]. Fornax also has five star clusters bound to it which might indicate that it has a cored DM profile [120], and the hypothesis of a constant density core is further supported by the work of Amorisco et al. [56].

Hercules

The Hercules dSph was discovered by Belokurov et al. in 2006 [71] and shows evidence of strong tidal disruption.

Leo I

Discovered by Harrington et al [124] in 1950, this 'classical' dSph has an extremely high radial velocity and a complex star formation history which might imply that it has had a strong encounter with the Milky Way in the past, or even possibly with a third body [160]. It has been under debate whether it is bound to the Milky Way or not due to its high velocity and large distance, but recent studies show that it is extremely unlikely that it is not bound to our galaxy [81].

Leo II

Leo II is a 'classical' dSph and the second most remote. It was also discovered in 1950 by Harrington et al [124]. It shows no signs of any tidal perturbation [145].

Leo IV

Discovered by Belokurov et al. in 2006 [71], this UFD might be connected to Leo V, since some work detect an optical 'bridge' between the two [204].

Leo V

Discovered by Belokurov et al. in 2008 [72] and might be connected to Leo IV.

Pisces II

Discovered by Belokurov et al. in 2010 [74] and still awaiting spectroscopic follow-up [162]. It has an elongated shape.

Sagittarius

Discovered by Ibata et al. in 1994 [131], Sagittarius was the first dSph found via spectroscopy rather than 'by eye', but since it was discovered before the SDSS it is still considered a 'classical' dSph. It is the most luminous and most massive dSph but strongly tidally disrupted and has recently formed significant stellar tidal tails [112]. Its proximity to the Galactic centre makes it complicated to separate from background. It lies in the Sagittarius stream as shown in Fig. 4.2.

Sculptor

Sculptor was the first 'classical' dSph and was discovered by Shapley in 1938 [186], and it was first classified to be a distant galaxy cluster before it was clear that it was a near-by object consisting of individual stars. It has two stellar sub-populations, one metal-rich and one metal-poor population, which seems to be a common feature among dSphs and points to a complex early stellar evolution [203]. Both populations are however consistent with an NFW dark matter potential [198].

Segue 1

Segue 1 was discovered by Belokurov et al. in 2006 where it was referred to as an unusually extended globular cluster that probably used to be associated with the Sagittarius dSph [71]. In 2009, Geha et al. concluded that Segue 1 is a DM dominated dSph [114], but Niederste-Ostholt et al. supported the claim it was a star cluster and that its stars were

indistinguishable from the Sagittarius stream [169]. However, more recent studies find that it is indeed a DM dominated UFD [188, 159]. They find that the contamination from the Sagittarius stream is not as prominent as estimated by earlier work, and that there are no evidence of it being tidally disrupted.

Segue 2

Discovered by Belokurov et al. in 2009 [73], Segue 2 lies on the edge of the Sagittarius stream and seems to be surrounded by a stellar debris, possibly coming from a tidally disrupting parent system. It might be the remnant of a larger galaxy (size of Ursa Minor) that was tidally stripped, or it may have been born in a low-mass DM subhalo [143].

Sextans

This 'classical' dSph was discovered in 1990 by Irwin et al. by automatic scanning of photographic survey plates [133], and the first to be discovered by an automated method. It contains some substructure in its center, which might be a remnant of a disrupted stellar cluster [65]. There are no evident signs of tidal disruption.

Ursa Major I

Discovered in 2005 by Willman et al. [212].

Ursa Major II

Ursa Major II was discovered in 2006 by Zucker et al. [220]. It is highly elongated and distorted which might suggest that it is being tidally disrupted [166], but the elongation is nearly perpendicular to the direction of the Galactic center, and typically it should point towards the Galactic center to be a sign of tidal disruption. It shows evidence of sub-populations of stars which can also be a sign of disruption [220]. Ursa Major II may be associated with the Orphan stellar tidal stream [70] (See Fig. 4.2).

Ursa Minor

Ursa Minor is one of the 'classical' dSphs and was discovered by Wilson et al. in 1955 [214]. It shows signs of tidal disruption since tidally disrupted stars have been identified in its outskirts [165]. It also has an extremely

low velocity dispersion substructure (possibly a stellar cluster) that might indicate that Ursa Minor has a cored DM structure [144].

Willman 1

The Willman 1 dSph was discovered in the SDSS data in 2004 by Willman et al. [211] and it was unclear weather or not Willman 1 was really a dSph. Later it was concluded that the large metallicity difference between the stars shows that Willman 1 is (or at least was) a dSph [213]. However, Willman 1 has very unusual kinematics where the inner stars have an offset in mean velocity from the outer ones. One theory presented in [213] is that it is not in dynamical equilibrium and has been stripped of a large amount of stars through tidal disruption.

4.2 A research field in motion

In March 2015, 9 possible new dwarf galaxies were detected in the Dark Energy Survey (DES) [7] data by two separate research teams [67, 147], and corresponding DM interpretations were made [109, 117]. Although interesting, these DM interpretations are not based on measured DM densities and should be viewed as preliminary. The new DES dwarf candidates will hopefully be observed further to correctly measure their DM content.

The DES collaboration use a likelihood-based algorithm to detect and classify stellar over densities in the internal DES catalog [67]. This publication was accompanied by a DM interpretation from a joint effort of the Fermi-LAT collaboration and the DES collaboration, where Fermi-LAT data targeting the DES dwarf galaxy candidates was analyzed using the pipeline from the Fermi-LAT dSph analysis [45] and preliminary upper limits on the DM annihilation cross section were obtained using estimated J-factors [109].

The independent research team [147] use the public DES data to build a catalog, and by matching 2D Gaussian functions to the background and possible stellar over densities, they obtain significance maps for possible over densities. This work was also accompanied by a DM interpretation using Fermi-LAT data targeting the most promising candidate from [147], Reticulum 2, to derive upper limits on the DM annihilation cross section for different possible J-factors [117].

Shortly thereafter, another new dwarf candidate was discovered in the Panoramic Survey Telescope And Rapid Response System (Pan-STARRS) data and followed up by photometry [149]. It is not clear if it is a dSph or a globular cluster since it is very faint and similar to Bootes II, Segue 1 and 2, and Willman 1.

Then the Survey of the Magellanic Stellar History (SMASH) also announced a new dwarf galaxy, Hydra II [155]. The dwarf is close to the Magellanic Stream and could possibly be connected to the Magellanic clouds.

In August 2015, the DES collaboration announced that 8 UFD candidates were discovered in the second year DES data [108], and that many of them might be connected to the Magellanic system.

4.3 Determining the dark matter content

The J factors are a central component in the DM analysis of dSphs, but neither the proper motions nor the individual distances of the stars in the dSphs are known, so to calculate the J factors, some assumptions have to be made. A common ansatz is that the dSph is spherically symmetric, in dynamical equilibrium, and that it has negligible binary motions. The mass profile is related to observed quantities using the Jeans equation, which describes the motion of a group of stars in a gravitational field.

When projected along the line of sight, the mass profile of the dSph will depend on observable quantities: projected velocity dispersion and projected stellar density. It will, however, also depend on assumptions about the stellar surface densities (i.e. the number of stars per unit area, modeled using e.g. King [142], Plummer [179], or exponential profiles), the shape of the DM halo (e.g. NFW, Burkert, or Einasto), and the intrinsic velocity anisotropy (the distribution of stellar orbits), β. β is defined as $\beta = 1 - \sigma_t^2/\sigma_r^2$ where σ_t^2 is the tangential velocity dispersion and σ_r^2 is the radial velocity dispersion [99].

The Jeans equation does not require the assumption that mass follows light, i.e. that the mass distribution is proportional to the stellar distribution, so the DM halo can be properly included [196]. The spherically symmetric Jeans equation is described as

$$\frac{1}{\rho_s}\frac{d}{dr}(\rho_s\sigma_r^2) + 2\frac{\beta\sigma_r^2}{r} = -\frac{GM(r)}{r^2}, \tag{4.1}$$

where G is the gravitational constant, $M(r)$ is the mass profile of the dSph (enclosed mass within radius r), and ρ_s is the three-dimensional density profile of the stellar distribution. σ_r^2 is not known, but the observable velocity dispersion projected along the line-of-sight, σ_{los}^2, can at a projected position, R, be expressed as

$$\sigma_{los}^2(R) = \frac{2}{I_s(R)} \int_R^\infty \left[1 - \beta(r)\frac{R^2}{r^2}\right] \frac{\rho_s \sigma_r^2 r}{\sqrt{r^2 - R^2}} dr, \tag{4.2}$$

where $I_s(R)$ is the stellar density at position R. I_s is obtained assuming a stellar surface density profile and ρ_s is obtained from I_s, normally assuming spherical symmetry. For a Plummer profile, I_s will only depend on the measured values of the total luminosity (L) and the half-light radius ($r_{1/2}$) [89], as

$$I(R) = \frac{L}{\pi r_{1/2}^2} \frac{1}{[1 + R^2/r_{1/2}^2]^2}. \tag{4.3}$$

The parameters of the mass profile are usually obtained assuming that the true stellar velocities, v_{true}, are distributed as a Gaussian with the mean value, $\bar{v}$, being the velocity of the dSph itself with intrinsic velocity dispersion, σ_{los}, given by the variance of the Gaussian. To include measurement uncertainties, the measured values, v_{los}, are assumed to be distributed as a Gaussian with the mean value being the true value, v_{true}, and the variance given by the measurement error, σ_m. A likelihood can then be constructed comparing the measured stellar velocities to the velocity dispersions for a set of free parameters defining the mass profile, $\boldsymbol{\theta}$ (and in some cases additional free parameters are added). In the Bayesian case (which is what is commonly used), the likelihood for the stellar sample with line-of-sight velocity distribution function $f(v_{los,i}, R_i)$, can e.g. be written as [196]

$$\begin{aligned} L(\boldsymbol{\theta}|D_{astro}) &= \prod_{i=1}^{n} f(v_{los,i}, R_i) \\ &= \prod_{i=1}^{n} \int \frac{1}{\sqrt{2\pi\sigma_{los}^2}} \exp\left[-\frac{(v_{true,i} - \bar{v})^2}{2\sigma_{los}^2}\right] \\ &\times \frac{1}{\sqrt{2\pi\sigma_m^2}} \exp\left[-\frac{(v_{los,i} - v_{true,i})^2}{2\sigma_m^2}\right] dv_{true,i} \\ &= \prod_{i=1}^{n} \frac{1}{\sqrt{2\pi(\sigma_{los}^2 + \sigma_m^2)}} \exp\left[-\frac{(v_{los,i} - \bar{v})^2}{2(\sigma_{los}^2 + \sigma_m^2)}\right], \end{aligned} \tag{4.4}$$

where i counts the individual stars, D_{astro} is the stellar data, and under the assumption of no rotational component (i.e. that the dSph is dominated by disorganized motion) [196].

The NFW profile can be re-parameterized to depend on the maximum circular velocity, V_{max}, and radius of maximum circular velocity, $R_{V_{max}}$, of the DM halo. This conversion is made by defining $r_s = R_{V_{max}}/2.163$ and $\rho_0 = \frac{4.625}{4\pi G}\left(\frac{V_{max}}{r_s}\right)^2$ (r_s given in kpc and ρ_0 in $M_\odot$ kpc^3), as described in [148].

The Jeans equation can be approximated to depend on the stellar velocity dispersion and half-light radius alone, constraining the mass only at the half-light radius [215, 205].

In Paper I we made a comparison using J factors from two different research groups, our internal work by M. Kaplinghat, G. D. Martinez, and L. Strigari, and an independent work by Charbonnier et al. [89]. Despite the fact that the effect of using different J factors for individual dSphs was clearly noticeable, the overall effect on the combined analysis of 10 dSphs was $< 10\%$ for a 100 GeV DM particle annihilating through the $b\bar{b}$ channel. This test is described in Section 7.1.4.

Both groups used Bayesian methods to calculate the J factors using the Jeans equation and measured line-of-sight velocities of stars, but some different assumptions were made. Common assumptions were that spherical symmetry was assumed for the stellar data and that the line-of-sight velocities were assumed to have a Gaussian distribution. For each dSph, the data is assumed to consist of one stellar population in dynamical equilibrium with negligible binary contamination.

For Paper I the DM mass distribution was calculated using an NFW profile parametrized to depend on V_{max} and $R_{V_{max}}$ as described above. The J factors were calculated for a radius of 0.5° which is larger than, or close to, the half-light radius for the dSphs. For the 'classical' dSphs, stellar velocities were binned in radial bins, but for the UFDs, which have fewer stars, individual stellar velocities were used. For the measured velocity dispersion, the intrinsic velocity dispersion and measurement errors were added in quadrature. For the 'classical' dSphs the intrinsic velocity dispersion was assumed to dominate the average measurement error (which was then neglected [158]). A flat prior was chosen for $\log(V_{max})$, and for the scale radius, the prior was chosen given that V_{max} should be consistent with the results of structure formation simulations (Aquarius and Via Lactea II).

In the analysis by Charbonnier et al. they make the minimal assumptions possible on DM distribution by choosing a generalized Hernquist profile [126] for the DM halo and fitting the parameters defining the shape of the profile. This profile is defined as

$$\rho(r) = \rho_0 \left(\frac{r}{r_s}\right)^{-\gamma} \left[1 + \left(\frac{r}{r_s}\right)^{\alpha}\right]^{\frac{\gamma-\beta}{\alpha}}, \tag{4.5}$$

where the NFW profile (described in Eq. 2.4) is recovered by $\alpha = 1, \beta = 3$, and $\gamma = 1$. They consider the spatial extension of the dSph and introduce a critical integration angle, where they claim an optimal J-factor estimate is obtained. As for Paper I stellar velocities are divided into radial bins. Here they estimate the square of the velocity dispersion in each bin by bootstrapping. They assume the orbital anisotropy to be constant but leave it free (within prior) in the fit, and they use a Plummer profile [179] for the stellar data. They also assume that 20% of the DM mass consists of substructure in form of NFW-shaped clumps. They use the publicly available CLUMPY package [90] for all their J-factor calculations. Since some of their included DM profiles cause a singularity at the center of the halo, a saturation scale is introduced.

The largest difference in J factor arises for Draco and Carina, where the Charbonnier et al. analysis gives lower values for the J factors. Charbonnier et al. do, however, have a different data set for Draco (and Ursa Minor). The fact that Charbonnier et al. model 20% of the DM mass as clumps could also have an impact even though they report that there is no significant boost from this fraction of substructure. There is also a noticeable difference for Sextans where the uncertainty is larger in the Charbonnier et al. analysis, but since their analysis has more free parameters, the uncertainties will be larger. For Paper I we used an NFW profile and Charbonnier et al. use a generic profile. As discussed in Section 7.1.4, the values we used for our comparison were for a integration angle of 0.492° since this is the reported integration angle closest to ours of 0.5°, and where the errors were asymmetric, we chose the larger error to be conservative. The smaller integration angle might give slightly lower values for the J factors. The J factors are plotted in Fig 4.3.

If the assumption is made that all dSphs are part of the same population of satellite galaxies, the data from the group of dSphs can be used to constrain the priors used in the Jeans modeling, where the individual priors then are interpreted as the probability of the observed properties given the underlying distribution of dSphs. For Paper II a novel Bayesian

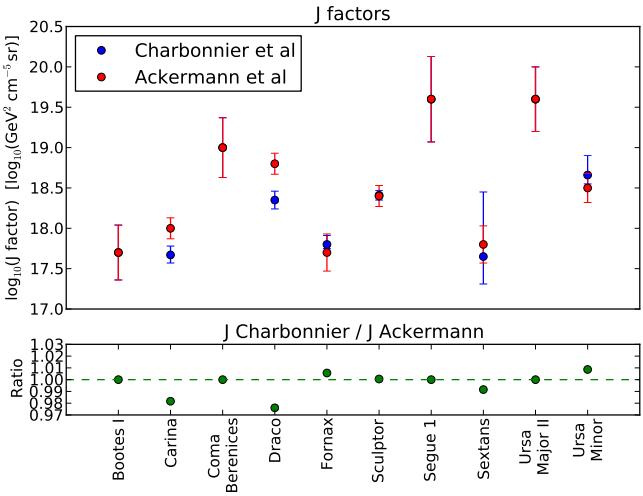

Figure 4.3: The top panel shows the J factors from Paper I (red) and the values for the 'classical' dSphs from Charbonnier et al. [89] (blue). In the bottom plot the ration comparing the two is plotted. Note that there are no values for Bootes I, Coma Berenieces, Segue 1, and Ursa Major II from Charbonnier et al.

hierarchical modeling technique by Martinez [157] was used, where the properties of the ensemble of dSphs were used to constrain the priors in this way, instead of relying on numerical simulations. Four different models for the DM density profiles were tested, NFW, Cored NFW, Burkert, and Einasto. This method not only constrains the individual properties, but also gives an overall estimate on the DM profile. As mentioned before, the fit seems to prefer a cuspy common halo shape. The resulting J factors for an NFW profile are plotted as a function of distance in Fig. 4.4. This plot shows a trend where closer dSph have higher J-factors. This originates from that the known dSphs seem to have a common inner mass-scale ($\sim 10^7$ solar masses within their central 300 parsecs) [197], resulting in a scaling of the J-factor approximately as the inverse square of the distance. There also appears to be a simple scaling relation between the half-light radius of a dSph and the mass within the half-light radius [205]. There is, however, work questioning the idea of a common mass scale and a simple scaling relation, where the the Milky Way dSphs are compared to the dSphs of the Andromeda galaxy [97].

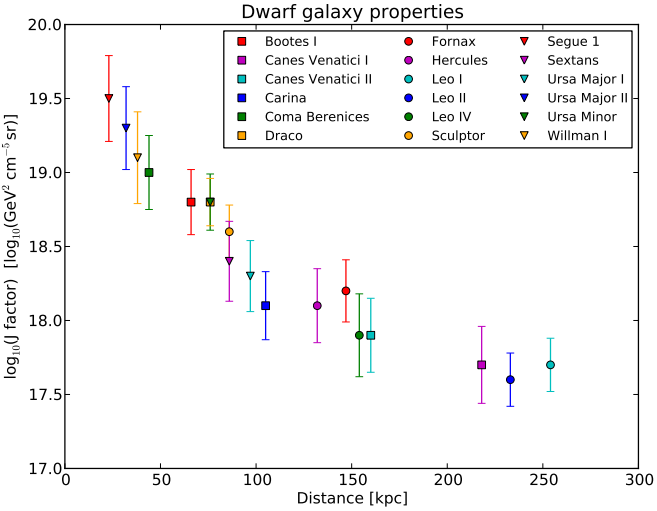

Figure 4.4: J factors of the 24 dSphs in Paper II for an NFW DM profile plotted as a function of their distance.

In most cases (except Bootes I, Draco and Ursa Minor), the same data was used for the J-factor calculations in Paper I and Paper II . The largest difference is for Bootes I, but when using the new data with the method used for Paper I the results are consistent.

Recent work by Geringer-Sameth et al. [116] use the approach of Charbonnier et al. [89], but more recent stellar data, to derive J factors for 20 dSphs. Since they analyze every dSph by itself, the uncertainties are much larger for the UFDs than in the Martinez analysis.

To facilitate an overall comparison of the resulting J factors, all J factors discussed in this thesis are compiled in Fig. 4.5.

4.3.1 J-factor systematics

As will be discussed in Section 5.5 we include the statistical uncertainties from the J-factor calculations in our DM analyses. The systematic uncertainties, however, are not included.

One large systematic effect is the choice of priors. Most Jeans modeling methods are dominated by the assumed priors.

In Paper I it is mentioned that a change of prior changes the median J factor for Segue 1 and Ursa Major II by a factor of ~ 2, and we therefore

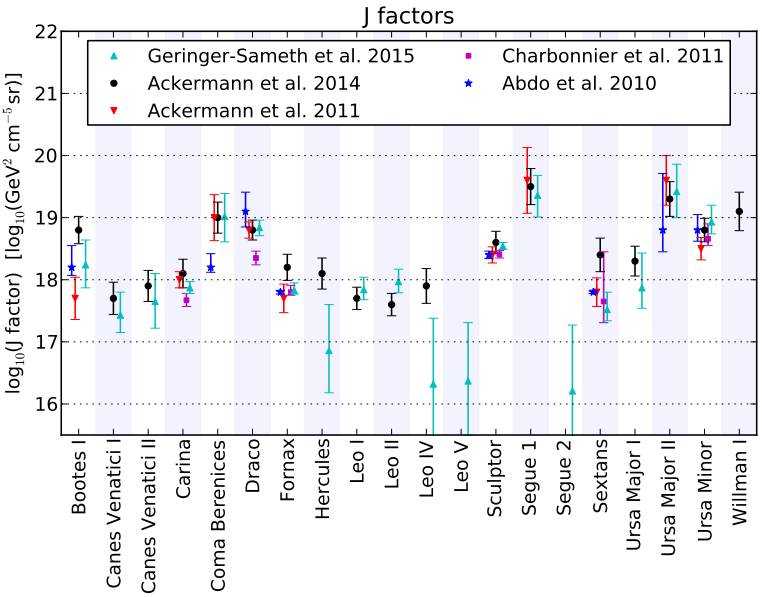

Figure 4.5: Compilation of J factors from five different publications, in reverse chronological order: values from Geringer-Sameth et al. 2015 plotted as cyan triangles [116], Paper II (Ackermann et al. 2014) plotted as black dots [43], Paper I (Ackermann et al. 2011) plotted as red triangles [35], values from Charbonnier et al. 2011, plotted as magenta squares [89], and the first Fermi-LAT dSph analysis (Abdo et al. 2010) plotted as blue stars [27].

present limits with and without these two UFDs. The assumption of using a Gaussian distribution for the velocities, and that the measurement error is much smaller than the intrinsic velocity dispersion, could give rise to a bias of about $\sim 50\%$ for the J factor.

Charbonnier et al. [89] mention a few systematic effects impacting their result. The choice of binning for the stars will add a factor of a few to the systematic uncertainty. The systematic effect from the prior for the inner slope of the DM profile is illustrated by testing two different priors, and this adds another factor of ~ 1.3.

The Bayesian hierarchical modeling technique is less prior dependent since it turns a prior dominated problem into a data dominated one by constraining the priors using data. Since the J-factor calculations for the

UFDs are the most prior dependent, these are the ones that benefit most from this technique.

The number of binary stars in the sample and other membership effects might alter the calculated J factor, and have to be taken into account when choosing the stellar sample. For binary star systems, it is the unknown center-of-mass velocity that is tracing the gravitational potential, and not the velocity of the individual stars. Stars from nearby stellar streams might also contaminate the stellar sample, and have to be addressed [188]. Assuming that the stars consist of one stellar population in dynamical equilibrium will also give rise to systematic effects, since some dSphs have multiple stellar populations and many show signs of tidal disruption.

The choice of the DM profile will directly impact the J factor and in DM searches it is therefore common to, either chose the more conservative model, or present the effect when using different models (as mentioned before, in Paper I we chose a NFW profile to be conservative and compare with values from Charbonnier et al. and in Paper II we also chose an NFW profile but compare with a Burkert profile).

Chapter 5

The likelihood method

In Paper I and Paper II , the main analyses have been performed using a frequentist approach and a binned maximum likelihood analysis. The method is discussed in the following sections, and all concepts are discussed in the framework of a counting experiment like ours.

5.1 Maximum likelihood analysis

One of the most common methods to estimate parameters of a model, given some observed data, is the maximum likelihood technique. The maximum likelihood estimate (MLE) of the parameter of interest, μ, is the value for which the likelihood, $L(\mu|D)$, has its maximum given the particular data, D. For large data samples, the MLE is consistent (converges towards the true value as the data increases), efficient (has a small variance), asymptotically unbiased, and the estimates are Normally distributed [136]. Free parameters in the likelihood fit, that are not the parameter of interest, are called nuisance parameters.

An unbinned likelihood analysis is always the best choice when possible, since it retains the full information of the data. In practice though, for large data samples, the unbinned likelihood becomes difficult to compute. Binning the data, e.g. in energy and space, is a common way to reduce computational time. The smaller the bins, the more accurate the likelihood will be (unbinned analysis can be compared to infinitesimally small bins), but it becomes computationally heavier as the number of bins increases.

We start by defining the Poisson likelihood for a target, i, an energy bin, j and a spatial bin, k, as a function of the signal parameter, μ, and

a set of nuisance parameters, $\boldsymbol{\theta}$, for the data, D. This binned Poisson likelihood can be written as:

$$L_{ijk}\left(\mu_{ijk}, \boldsymbol{\theta}_{ijk} \,|D\right) = \frac{\lambda_{ijk}^{n_{ijk}}}{n_{ijk}!} e^{-\lambda_{ijk}}, \tag{5.1}$$

where $n_{ijk} = n_{ijk}(D_i)$ are the observed counts and $\lambda_{ijk} = \lambda_{ijk}(\mu_i, \boldsymbol{\theta_i})$ are the counts predicted by the model for each target and bin.

5.1.1 Hypothesis testing

A hypothesis test is used to evaluate how well observed data agrees with different hypotheses (e.g. signal vs no signal). The significance level of a test, α, is the probability to reject the null hypothesis when it is true, also called a type I error. Similarly, when the null hypothesis is accepted, even though the alternative hypothesis is the true one, is called a type II error. If the probability of a type II error is β, then the power of the test is defined as $1 - \beta$, which is the probability that the test correctly rejects the null hypothesis when the alternative hypothesis is true. A so called p-value is defined as being the observed significance level, i.e. the probability to, assuming no signal, obtaining the observed number of events or more.

The Neyman-Pearson test is shown to be the optimal test to be used for simple hypotheses, where a critical region (where the null hypothesis is rejected) is chosen to maximize the power of the test [136]. It is defined as

$$TS = \frac{L(\mu_0)}{L(\mu_1)} \leq c_\alpha \tag{5.2}$$

where c_α is chosen to give the test the desired significance level, α.

For composite hypotheses this must be extended to the likelihood ratio test. The test statistic for the null hypothesis, the maximum likelihood ratio, is defined as:

$$TS = \frac{L\left(\mu_0, \hat{\hat{\boldsymbol{\theta}}} \,|D\right)}{L\left(\hat{\mu}, \hat{\boldsymbol{\theta}} \,|D\right)}. \tag{5.3}$$

Here μ is the parameter of interest and $\boldsymbol{\theta}$ are the nuisance parameters. $\hat{\mu}$ and $\hat{\boldsymbol{\theta}}$ are fitted over the full parameter range and $\hat{\hat{\boldsymbol{\theta}}}$ are fitted under the null hypothesis, i.e. $\mu = \mu_0$.

In log space, it is common to define a test statistic as

$$TS = -2\Delta \ln L = -2 \ln \frac{L\left(\mu_0, \hat{\hat{\boldsymbol{\theta}}} \,|D\right)}{L\left(\hat{\mu}, \hat{\boldsymbol{\theta}} \,|D\right)}, \tag{5.4}$$

since $-2\Delta \ln L$ is (asymptotically) distributed as χ^2 with n degrees of freedom (Wilk's Theorem [210]). Here n is the difference in free parameters of the null hypothesis versus the alternative hypothesis. Some requirements for Wilk's theorem are that the hypotheses are nested and that the MLE is efficient. The theorem is e.g. not valid if trial factors are included [98]. If the null hypothesis is on the boundary of the parameter range, rather than obeying Wilk's theorem the distribution is given by Chernoff's theorem [93],

$$-2\Delta \ln L = \frac{1}{2}(\delta(0) + \chi^2), \tag{5.5}$$

where the degrees of freedom of the χ^2 distribution are defined as for Wilk's theorem and the Dirac delta function, $\delta(0)$, describes the boundary (0 in this case).

5.1.2 Confidence intervals

While a hypothesis test accepts or rejects an hypothesis, a confidence interval (CI) will give an estimated range of values which is likely to include the true value of the parameter of interest. The CI is set to include the true value of the parameter of interest at a specific confidence level (CL), where the CL is defined as $1 - \alpha$. A CI can be either two-sided, having both an upper limit (UL) and a lower limit (LL), or one-sided interval giving either an UL or a LL. In the case of an UL (LL), the CI does not constrain the parameter of interest from lower (upper) values. In the case of a detection, two-sided CIs are usually published, but in the case of a null-detection (no detected signal) one-sided intervals are usually reported.

One important feature in frequentist statistics is the coverage of the method. If you report a 95% CI, you have to be sure that for many repeated experiments, the true value is covered with a probability of 0.95, i.e. that the CI fails to cover the true value in 5% of the cases. If the method overcovers, the results will be conservative, which is not a problem in itself, but it will lose sensitivity. Overcoverage can e.g. arise close

to physical boundaries of measured parameters. When working with discrete data, coverage is normally not exact for all signal strengths, and instead of demanding exact coverage, overcoverage is accepted. Systematic uncertainties may also cause overcoverage. Undercoverage is a larger issue since it leads to overly aggressive exclusion.

An example of a method for confidence intervals is the Neyman construction [168], where a confidence band is constructed using several pseudo-experiments from which the CI is obtained. A problem arises when setting intervals close to the boundary of the parameter range, where it is possible to measure the parameter at a value that is not allowed by the model (an unphysical value, e.g. a negative value for the DM annihilation cross-section). From a statistics point of view, this is not a problem since the method still covers by construction, but if the measured interval has no physically allowed values for the measured parameter, it is considered an 'empty interval'. Another problem that arises, regardless of how the CI is obtained, is when choosing between reporting ULs or two-sided CIs, known as 'flip-flopping'. Deciding which interval to report after analyzing the data, instead of before, might give undercoverage. These problems can be avoided by the so called 'unified approach' described by Feldman and Cousins in 1998 [111], where they introduced a method to include observations when constructing the confidence belt, yielding correct coverage and giving two-sided CIs when allowed by the observations and ULs otherwise.

In Paper I and Paper II , however, we use likelihood based CIs since they are not as computationally heavy as the full Feldman-Cousins computation. Knowing that our test statistic $(-2\Delta \ln L)$ follows a χ^2 distribution, we can find the CI where the log-likelihood has decreased by a factor of $up/2$ from its maximum, where up defines the chosen percentile of a χ^2 distribution with the adequate degrees of freedom [182]. For a 90% CI (or a 95% UL if the parameter is close to 0), e.g. , we find our interval where the log-likelihood has decreased by $2.71/2$ from its maximum. This method of likelihood based CIs works for non-Gaussian likelihoods as well as for Gaussian likelihoods [136]. In the case where there are multiple parameters (as in the case with a parameter of interest and nuisance parameters), this is called a profile likelihood and is defined as

$$L(\mu|D) = \frac{L(\mu, \hat{\hat{\boldsymbol{\theta}}}\,|D)}{L(\hat{\mu}, \hat{\boldsymbol{\theta}}\,|D)}, \tag{5.6}$$

where, as in Eq. 5.3, $\hat{\mu}$ and $\hat{\boldsymbol{\theta}}$ are fitted over the full parameter range

and $\hat{\hat{\boldsymbol{\theta}}}$ are fitted under the condition of the parameter μ. The profile likelihood method is known to have acceptable coverage for large numbers of parameters, and it is also known to cover even when the parameter of interest is close to its physical boundary [182]. The MINOS subroutine in Minuit [135] was implemented for this purpose and the profile likelihood method is often referred to as the 'method of minos' [136].

In Paper I we use the MINOS routine, as implemented in the Fermi Science Tools, to find our ULs. MINOS steps through the profile likelihood function to find the point where it has decreased by the chosen fraction. The MINOS routine works for both symmetric and asymmetric likelihood functions and is well tested. MINOS will return a two-sided CI when possible and a one-sided otherwise. By automatically changing from a one-sided confidence interval to a two-sided confidence interval when the signal becomes stronger, we avoid flip-flopping

In Paper II , the same method is used but with an independent routine implemented in the 'bin-by-bin' pipeline, described in Section 5.4.

5.2 The joint likelihood method

In the case where all targets have a common parameter, the sensitivity of the analysis can be increased by a combined analysis of the targets, using the joint likelihood method. For example, in the analysis of dSphs, the DM particle properties are the same for all targets (but the astrophysical properties are different). This is not to be confused with data stacking, where the data from different targets is added into one single stacked target and then this stacked data is analyzed (see e.g. [57, 103] for comparison of the methods).

A joint likelihood function can be created from the individual likelihood functions of each target,

$$L\left(\mu, \{\eta_i\} \,|D\right) = \prod_i L_i\left(\mu, \eta_i \,|D_i\right), \tag{5.7}$$

where μ are the common signal parameters and $\{\eta_i\}$ are the individual nuisance parameters.

Even though the signal is fitted jointly over different separate regions of interest (ROIs), the backgrounds are fitted separately and optimized in each ROI.

This method was first implemented for, and used in, Paper I , but has later become a popular method in astrophysics (see e.g. [29, 41, 43, 44,

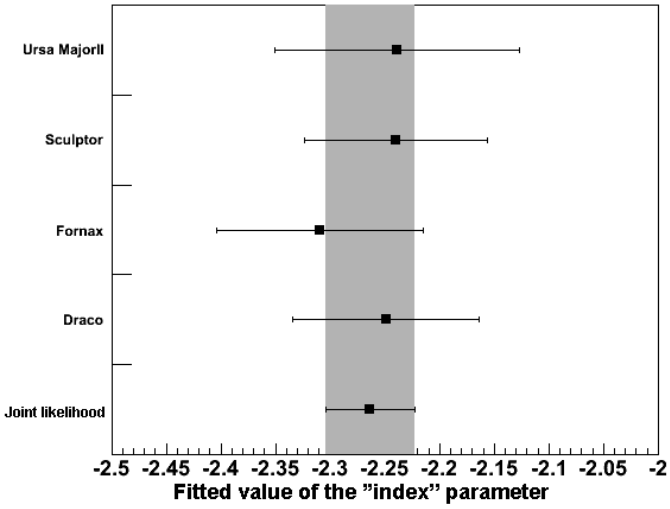

Figure 5.1: A simple example of the effect of a joint likelihood fit for 4 dSphs modeled as power-law point sources with the 'index' parameter set to -2.25. The gray band is a guide to the eye to compare with the combined result. The joint likelihood fit reduces the errors by a factor ~ 2.

45, 53, 109, 115, 118, 119, 129, 180, 217, 218] for joint likelihood analyses using the *Composite2* code, the 'bin-by-bin' pipeline, or similar analysis methods.).

An example of how the joint likelihood increases the sensitivity is shown in Fig. 5.1. Here four dSphs have been simulated as power law sources with background. The fit was made using the early iteration of the joint likelihood code in Fermi Science Tools, *CompositeLikelihood*. The combined fit gives a smaller CI than the individual fits since it includes more data. In this particular example, the errors have been decreased by a factor ~ 2. Coverage of the joint likelihood has been tested for different cases as described in Section 5.6.2.

In Paper II the test statistic (TS) distribution of the joint likelihood analysis of Fermi-LAT data was tested (see section 5.6.4). Even though the results for simulated data are well described by Chernoff's theorem, the results from real data are not. It is therefore of great importance to be cautious.

5.3 The Fermi-LAT likelihood

Since the standard method for analyzing Fermi-LAT data applies forward folding, the IRFs need to be included. In the Fermi Science Tools the likelihood analysis is implemented in the *gtlike* function which can perform unbinned or binned likelihood analysis of LAT data including the IRFs. As described in Chapter 3, the IRFs consist of three parts; the effective area, the PSF, and the energy dispersion. These functions can be written as

$$R(E', \psi'; E, \psi, s) = A(E, \psi, s) \times P(\psi'; E, \psi, s) \times D(E'; E, \psi, s), \quad (5.8)$$

where E is the true photon energy, ψ is the true photon direction, E' is the measured photon energy, ψ' is the measured photon direction, and s is the event selection. $A(E, \psi, s)$ is the instrument effective area, $P(\psi'; E, \psi, s)$ is the PSF, and $D(E'; E, \psi, s)$ is the energy dispersion [40].

The number of expected events, λ_{jk}, in each bin, depends on the model, $S(E, \psi) = S(\mu(E, \psi), \boldsymbol{\theta}(E, \psi))$, and on the IRFs, $R(E', \psi'; E, \psi, s)$,

$$\lambda_{jk} = \int_{Analysis\ space} R(E', \psi'; E, \psi, s) S(E, \psi) dt dE d\Omega. \quad (5.9)$$

The analysis space is here defined as the time range, energy range, and source region of the analysis. The source region, where the model is defined, is often chosen to be larger than the ROI to include photons coming from sources just outside the ROI due to the PSF. The total predicted number of events is the sum over the bins, $N_{pred} = \sum_{jk} \lambda_{jk}$, which is a function of the model.

Since N_{pred} then can be factored out, the binned likelihood used in the Fermi Science Tools then becomes[1]:

$$L(\mu, \boldsymbol{\theta} \,|D) = e^{-N_{pred}} \prod_{jk} \frac{\lambda_{jk}^{n_{jk}}}{n_{jk}!}, \quad (5.10)$$

where n_{jk} is the number of observed events in bin jk.

Additional likelihood terms can be added to include uncertainties in the nuisance parameters,

$$L_i\,(\mu, \eta_i \,|D_i) = L_i(\mu, \boldsymbol{\theta}_i \,|D_i) \times L_{i,\,nuisance}, \quad (5.11)$$

where η_i are the nuisance parameters for each target, i, and $L_{i,\,nuisance}$ are the likelihoods including the nuisance parameter uncertainties. In Paper

[1] http://fermi.gsfc.nasa.gov/ssc/data/analysis/documentation/Cicerone/Cicerone_Likelihood/Likelihood_formula.html

I and Paper II we included the uncertainty of the J factor by adding it to the likelihood function, where the additional likelihood term is obtained from the stellar data analysis determining the J factors. This will be described in Section 5.5.

5.3.1 Joint likelihood in Fermi Science Tools

The joint likelihood method was implemented within the Fermi Science Tools, first as the *CompositeLikelihood* code, where one parameter could be tied over the different ROIs, and later as the *Composite2* code, where several parameters can be tied.

The code is implemented for both unbinned and binned analysis, but an unbinned analysis becomes very computationally heavy when many ROIs are added.

Compared to the 'bin-by-bin' likelihood pipeline described in the next Section, the *Composite2* code has several advantages, e.g. that it uses the full likelihood and has no limitations in what energy cuts and energy binning to use, apart from what is recommended for the data. Several nuisance sources can be fitted together with the putative signal in the combined fit, limited only by the allowed number of free parameters in MINOS. There is also the option of tying the normalizations of the diffuse background models in a joint fit, as discussed in Section 7.1.5.

5.4 The 'bin-by-bin' likelihood approach

The standard recipe for fitting the Fermi gamma-ray sky is to fit the background models, most of the point sources, and the source of interest all at the same time. But when searching for DM you do not know the spectrum of the putative source. It can therefore be helpful to obtain flux upper limits to which different DM spectra can be fitted at a later point. Publishing the corresponding likelihoods opens up for the community to fit their own spectra to the result. Therefore a 'bin-by-bin' analysis pipeline was developed [171], where limits (or measurements) of the source flux are set in different energy bins.

In Paper II we use this 'bin-by-bin' likelihood analysis method as described in Section III and V of Paper II and summarized here.

First the backgrounds are fitted over the full energy range to obtain their best fit values (global MLEs). In the second step, a putative target source is included, modeled as a power law, to pick up any possible signal.

Then the source of interest, still modeled as a power law, is fitted independently in each energy bin to obtain limits on the putative source flux that are independent of the source spectrum over the full energy range. In this fit the background parameters are fixed at their best-fit value from the preceding global fit. This 'bin-by-bin' likelihood function is defined as

$$L\left(\{\mu_j\}, \hat{\boldsymbol{\theta}} \,|D\right) = \prod_j L_j\left(\mu_j, \boldsymbol{\theta}_j(\hat{\boldsymbol{\theta}}) \,|D_j\right), \tag{5.12}$$

where $L\left(\mu_j, \boldsymbol{\theta}_j \,|D_j\right)$ is the binned Poisson likelihood for each energy bin, j, $\{\mu_j\}$ is a set of independent signal parameters, $\hat{\boldsymbol{\theta}}$ is the global MLE of the nuisance parameters in all bins, and D is the photon data. The reason to use $\hat{\boldsymbol{\theta}}$ instead of fitting the nuisance parameters in each step is to avoid numerical instabilities for faint sources.

To recreate a pseudo-profiled global likelihood function to test a given signal spectrum, the 'bin-by-bin' likelihoods are joined tying the signal parameters over the energy bins:

$$\tilde{L}\left(\mu, \hat{\boldsymbol{\theta}} \,|D\right) = \prod_j L_j\left(\mu_j(\mu), \boldsymbol{\theta}_j(\hat{\boldsymbol{\theta}}) \,|D_j\right). \tag{5.13}$$

This is not a true profile likelihood since the nuisance parameters are fixed to their best fit values, but it has been shown to give comparable result to the full likelihood (see Section 7.1.1). In Paper II this first global fit is made for background sources only, and the MLE of the background normalization parameters change with $< 1\%$ if a second broad-band fit is made including a power-law signal source, which is considered negligible in this case.

When recreating the global likelihood function, additional nuisance parameters arising from the model for the signal spectra can be added (which was introduced for the analysis in Paper I , described above). In Paper II , the statistical uncertainties in the astrophysical part of the DM spectrum were included this way (see section 5.5). The likelihood then becomes

$$\tilde{L}_i\left(\mu, \eta_i \,|D_i\right) = \tilde{L_i}(\mu, \hat{\boldsymbol{\theta}}_i \,|D_i) \times L_{i,\,nuisance}, \tag{5.14}$$

where, as in Eq. 5.11, η_i are the nuisance parameters for each target, and $L_{i,\,nuisance}$ are the likelihood including the nuisance parameter uncertainties.

The 'bin-by-bin' analysis pipeline was developed for Paper II , but has now been used in several other projects (see e.g. [45, 83, 107, 109, 218]).

5.4.1 Joint likelihood in 'bin-by-bin' pipeline

In the 'bin-by-bin' pipeline the joint likelihood is implemented in a similar way, but with the difference that it is a joint likelihood of pseudo-profile likelihoods instead of the joint likelihood of the full likelihoods as in the *Composite2* code. The resulting joint likelihood from the 'bin-by-bin' pipeline is then

$$\tilde{L}\left(\mu, \{\eta_i\} \,|D\right) = \prod_i \tilde{L}_i\left(\mu, \eta_i \,|D_i\right), \tag{5.15}$$

where $\tilde{L}_i\left(\mu, \eta_i \,|D_i\right)$ is described en Eq. 5.14. The pseudo-profile likelihoods are computed over all nuisance parameters individually for each target and joined afterwards.

5.5 Including statistical uncertainties of the astrophysical factor

As described in Eq. 5.11 and Eq. 5.14, additional likelihood terms can be added to the likelihood including nuisance parameters and their uncertainties. If we knew the likelihood for the J factors, e.g. from a fully frequentist analysis, this would be straight forward. However, the J factors are determined using a Bayesian approach (described in Chapter 4) and thus including the J-factor uncertainties in the analysis of the LAT data is not trivial. An ansatz has to be made on what shape to use for the extra term in the likelihood, and this anzats can preferably be formulated using the result of the separate analysis determining the J factors.

For Paper I the J factors were derived using approximately flat priors, in this case wide compared to the posteriors as shown in Fig. 5.2. Our ansatz is thus to use the PDF from the J-factor analysis as our additional likelihood term. Even though the priors on individual parameters are wide, there are no guarantees that the total prior will be uniform in the region of interest. The priors used in the J-factor calculations are plotted in the left panel of Fig. 5.3.

The posterior PDFs of the J-factor analysis in Paper I can be well approximated with log-normal functions, and the term included in the likelihood analysis, as in Eq. 5.11 and Eq. 5.14, is thus

$$\begin{aligned} L_J(J_i) &\propto P_J(D_{astro,i}|J_i) \\ &\propto \frac{1}{\ln(10)\, J_i \sqrt{2\pi}\sigma_i} e^{-\left[\log_{10}(J_i) - \overline{\log_{10}(J_i)}\right]^2 / 2\sigma_i^2} \end{aligned} \tag{5.16}$$

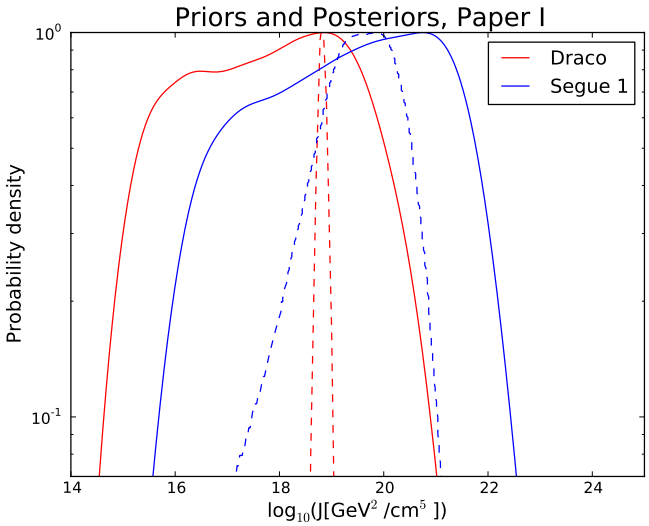

Figure 5.2: Example of the prior (solid lines) and posterior (dashed lines) probability density functions for two dSphs; Draco (red) which has a large stellar sample and hence a narrow posterior (small uncertainty), and Segue 1 (blue) which is an UFD with a resulting wide posterior. Data from Gregory D. Martinez.

where $\overline{\log_{10}(J_i)}$ and σ_i are functions of the data set $D_{astro,i}$, and J_i is the parameter. The ln(10) term arises from the transformation from the natural logarithm to $\log_{10}$. $D_{astro,i}$ is the astrophysical data (stellar positions and line-of-sight measurements).

The effect of including this uncertainty is naturally large when the uncertainty is large, and small when it is small. The effect on the combined limits depends on all the individual uncertainties and the change in the limits for an example of two dSphs with different uncertainties is shown in Fig. 5.4. A comparison of the resulting upper limits for all 10 dSphs for the different annihilation channels in Paper I , for using the nominal J factors and including the uncertainties, respectively, is compiled in Fig. 5.5. In the final stages of the preparation of Paper I , the DMFIT package was updated to include lower WIMP masses. Fig. 5.5 is obtained using the older version of DMFIT, and thus the limits for the lowest masses are not included.

For Paper II , a novel method for determining the J factors was introduced and the priors were no longer approximately flat [157]. Though the

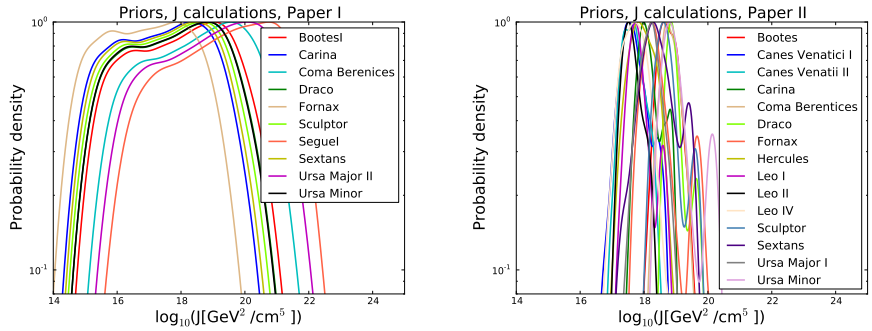

Figure 5.3: Examples of the shapes of the priors used for the J-factor calculations in Paper I (left) and Paper II (right). The analysis for each J-factor calculation was run without using the stellar data, which gives a posterior equal to the prior, which is then plotted. The priors used for Paper I are fairly flat while the priors used for Paper II are clearly not flat. Note that for Paper II a Bayesian hierarchical modeling technique was used. Data from Gregory D. Martinez.

priors had changed, we used the same ansatz for the J-factor uncertainties and continued to approximate the likelihood in the same way. The difference in the priors is shown in Fig. 5.3.

For the latest iteration of the Fermi-LAT dSph analysis [45], the ansatz for the J-factor term was changed to

$$L_J(J_i) \approx \frac{1}{\ln(10)\,\overline{J_i}\sqrt{2\pi}\sigma_i} e^{-\left[\log_{10}(J_i)-\log_{10}(\overline{J_i})\right]^2/2\sigma_i^2}, \tag{5.17}$$

where the difference from Eq. 5.16 lies in the denominator where J_i has been replaced by $\overline{J_i}$, i.e. the parameter value in the denominator has been replaced by the measured value. Here a log-normal function with peak value $\overline{J_i}$ was fitted to the posterior PDF to obtain the parameters for the added likelihood term. The same J-factor analysis method as in Paper II was used [157]. In the supplemental material of [45] it is stated that the advantages of this ansatz are the fact that it is properly normalized for all values of J_i, and that the MLE in the Fermi-LAT analysis coincides with the nominal value since the distribution peaks at the measured value. Although being a convenient choice, it is still an ansatz and the resulting impact on the limits is smaller, and hence this ansatz is less conservative.

A comparison of the resulting ULs is shown in Fig. 5.6 where we used 2 years of P7REP data for observations of the Draco dSph, the

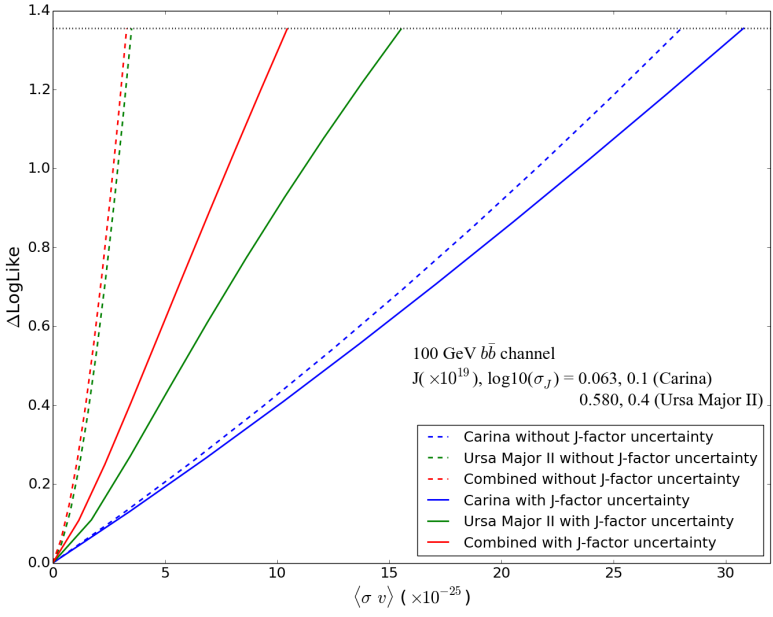

Figure 5.4: The profile likelihood, $\Delta \ln L$, plotted as a function of $\langle \sigma_{\rm ann} v \rangle$ for two different targets, Carina (blue) and Ursa Major II (green), and their combination (red). Likelihood curves obtained using nominal values for the J factor are plotted in dashed lines and likelihood curves including J-factor uncertainties are plotted in solid lines. The dotted black line indicates where $\Delta \ln L = up/2$ ($up = 2.71$ for 95% ULs). J factors and the corresponding uncertainties are given in the plot. Carina has a small J factor but also a small uncertainty giving a large UL that does not change much when the uncertainty is included. Ursa Major II on the other hand has a large J factor giving a small UL, but a large uncertainty resulting in a large impact when introducing it. The impact on the combined limit is neither as large as for Ursa Major II nor as small as for Carina. Figure credit: Johann Cohen-Tanugi for the Fermi-LAT Collaboration. Figure from [98].

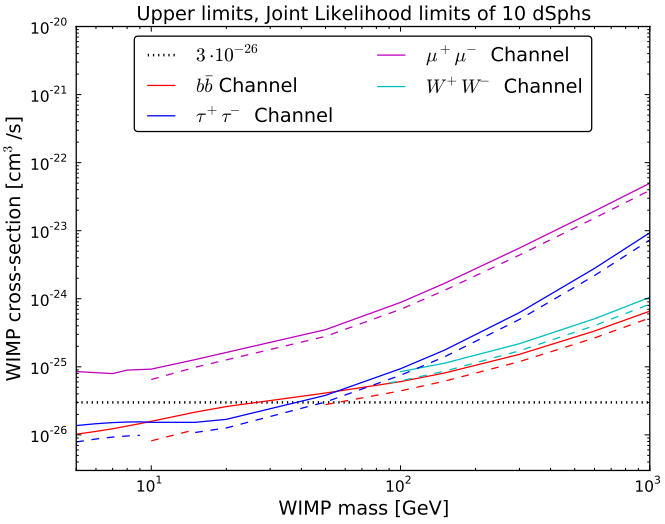

Figure 5.5: Upper Limits on the WIMP annihilation cross section when using the nominal value for the J factors (dashed lines) compared to the uper limits when including the J-factor uncertainty (solid lines) for four different annihilation channels. The average difference is approximately a factor 1.3 increase in the limits when introducing the J-factor uncertainties.

P7REP_CLEAN_V15 IRFs, corresponding diffuse background models, and the 2FGL point source catalog. Draco was modeled as an extended source with an NFW DM profile. In this particular case, the mass-averaged difference including the J-factor uncertainty compared to using the nominal value for the J factor is 1.32 for the $1/J$ ansatz (used in Paper I and Paper II) and 1.17 for the $1/\bar{J}$ ansatz (used in the latest iteration [45]), respectively.

It is important to note that Fig. 5.5 and Fig. 5.6 were made using different J factors, different data, different setups, and different pipelines and should not be compared to each other. Tests comparing the pipelines and J factors are discussed in Chaper 7

5.6 Statistical studies

The expected limits from the joint likelihood are not intuitive since different targets have different nuisance parameters and different backgrounds,

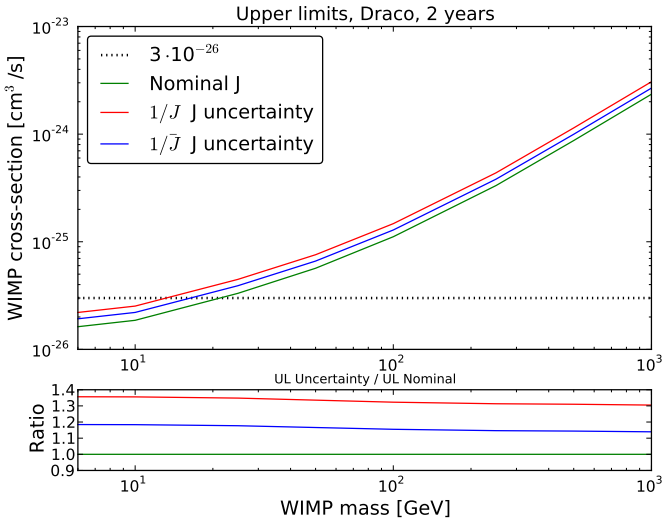

Figure 5.6: Top panel: ULs analyzing two years of data targeting the Draco dSph using the different formulations for the J-factor uncertainty in Paper I and Paper II (labeled $1/J$, plotted in red) and latest iteration of the Fermi-LAT dSph analysis [45] (labeled $1/\bar{J}$, plotted in blue). The ULs using the nominal J factors is plotted in green. Bottom panel: The ratio comparing the ULs including the uncertainties on the J factors with the ULs for the nominal values of the J factors.

and we have performed a series of tests to explore the behavior of the method.

5.6.1 Recover a simulated signal

To ensure that our method is sensitive to a weak signal we simulated weak DM sources to test the *Composite2* code. Fig. 5.7 shows the results when simulating a weak source in 6 dSphs and making both individual and combined analyses. The combined analysis (using the joint likelihood method) finds the weak signal with higher significance than the best individual dSph. For most of the dSphs, only ULs are set, but the joint likelihood gives a two-sided confidence interval that properly covers the true signal with good significance.

Note that the limits are calculated for fixed masses. To find the best fit value for the mass as well as the cross section, both parameters must

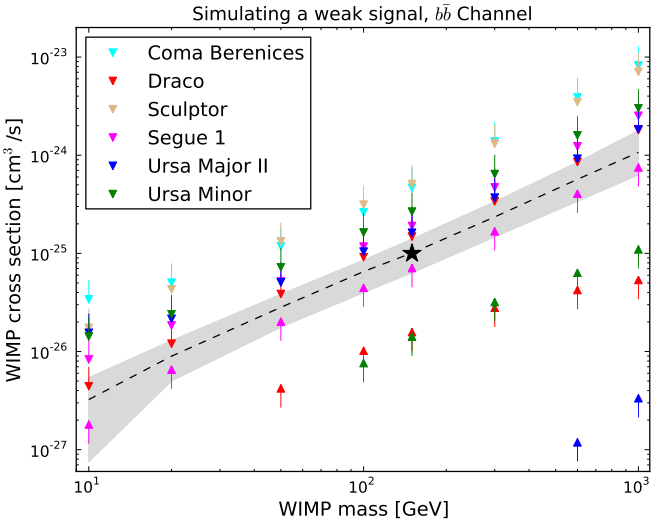

Figure 5.7: Result of a test where weak signals proportional to the dwarfs J factors are simulated together with diffuse backgrounds (galactic and isotropic). The simulated signal is a DM particle with a mass of 150 GeV and cross section of 10^{-25} cm^3 s^{-1} annihilating through the $b\bar{b}$ channel, here indicated with a star. ULs are plotted with downward-facing arrows, and LLs with upward-facing arrows. This signal is recovered by the combined analysis (gray shaded band, MLE plotted as dashed line), but not by all individual analyses (some only yielding ULs).

be left free in the fit. In Fig. 5.8 the individual fit result is shown for two dwarfs. For this test we simulated 1 year of Pass-6 data using the P6_V3_DIFFUSE IRFs and the signal strengths for the different dwarfs was set proportional to their J factor. The diffuse models were *gll_iem_v02* and *isotropic_iem_v02*.

We also made tests simulating strong signals with background and recovered the parameters as expected. As an example, when simulating a signal from a 150 GeV WIMP with $\langle\sigma_{\rm ann}v\rangle$ =10^{-25} cm^3 s^{-1} with very high flux and galactic and isotropic backgrounds, we recover the parameters as $\langle\sigma_{\rm ann}v\rangle = (0.88 \pm 0.13) \times 10^{-25}$ cm^3 s^{-1} and mass= (141 ± 14)GeV when leaving both mass and cross section free in the fit. A combined analysis of multiple targets will, as described above, narrow the CIs.

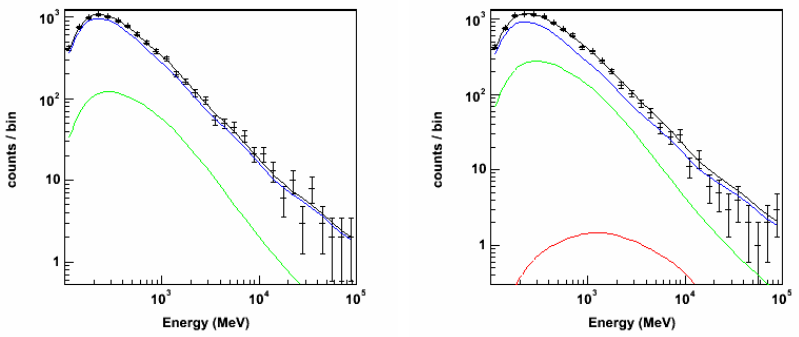

Figure 5.8: Spectral plots of Sculptor in the left panel and Segue 1 in the right panel from an analysis of a weak simulated signal from a DM particle with a mass of 150 GeV and cross section of 10^{-25} cm^3 s^{-1} annihilating through the $b\bar{b}$ channel. The signal is chosen to be proportional to the dwarf J factor and is therefore stronger for Segue 1. The isotropic diffuse component is plotted in green and the galactic diffuse component in blue. The DM component is plotted in red but not visible for Sculptor.

5.6.2 Coverage

When first implementing the joint likelihood method, we made a simple Toy Monte Carlo test and could see that the method covered. We found that, in the case where the signal is constrained to only take positive values in the fit, the method will overcover because the CI will be shifted towards the positive values. However, for the test case where the signal could take all values in the fit, overcoverage was not an issue. We do constrain the DM cross section to only take positive values in the dSph analyses ([35, 43, 45]), yielding conservative results.

In this first test we performed a joint likelihood analysis of 10 targets, simulating the target as one Poisson process for the signal and one for background (with 3 background counts), and analyzing using Minuit and MINOS with level=2.71 (giving 90% two-sided confidence intervals and 95% upper limits). The results from more recent runs using the code from this first test are shown in Fig. 5.9, both in the case of two-sided intervals and for upper limits. The 'saw-like' feature is due to the discreetness of the Poisson process.

But when using real data, there are unresolved point sources that we know might alter the TS distribution (see Section 5.6.4). This might also

affect the coverage. Coverage studies of the joint likelihood in the 'bin-by-bin' pipeline from Paper II using Monte Carlo have been made in Paper II and in the following iteration using Pass 8 data [43, 45], and these tests address the fact that we include the uncertainties of the J factors. These tests did not take unresolved point sources into account. The coverage behavior was confirmed in both cases [43, 45].

5.6.3 Behavior of the combined limits

In theory, the confidence intervals of the joint likelihood analysis would scale like $1/\sqrt{N}$ for a Gaussian likelihood, where N is the number of targets. But this is not always the case. When analyzing Fermi-LAT data we find that having a soft source spectrum (e.g. a DM particle with 20 GeV mass) will result in limits scaling like $1/\sqrt{N}$, while a hard source spectrum (e.g. a DM particle with 1000 GeV mass) will result in a $1/N$ scaling behavior. The Fermi-LAT is nearly background free at high energies and the limits will therefore scale like $1/N$ in this region. Using a Toy Monte Carlo, we retrieve the $1/\sqrt{N}$ behavior for the case where the signal parameter is unconstrained and there are 10 background counts to 1 signal count [57]. However, for the case where we set the background counts to 0.1, we get a $1/N$-like behaviour. In Fig. 5.10 the results from this Toy Monte Carlo are compiled.

5.6.4 TS distribution

In Paper II the TS distribution of individual fits from 50000 realistic Monte Carlo simulations was compared to the TS distribution of individual fits from LAT data at 7500 random blank-sky locations. The TS distribution from the simulated data is in agreement with Chernoff's theorem but the TS distribution from data is clearly not, and it was discussed to be due to insufficiently modeled backgrounds (i.e. unresolved point sources and imperfect diffuse background models). It has been suggested that multi-wavelength data can be used to identify unresolved sources and improve the background modeling, and Carlson et al. [87] show that more than 50% of the high-TS residuals observed in the blank sky correspond to sources found in other catalogs.

The study was repeated for the latest iteration of the Fermi-LAT dSph analysis, where the difference when using the 3FGL and 2FGL point-source catalogs for 6 years of data is discussed [45] (as mentioned in Section 2.2, 3FGL contains over 1000 more sources than 2FGL). The result

is shown in Fig. 5.11. Including more sources result in a TS distribution that lies closer to the distribution from Chernoff's theorem, implying that part of the discrepancy is caused by the fact that the data contains unresolved point sources that might contribute to a measured signal (i.e. increasing the number of type I errors in the analysis). It is worth noting that the 2FGL is inadequate to use when analyzing 6 years of data for other purposes than testing, since it is constructed using 2 years of data.

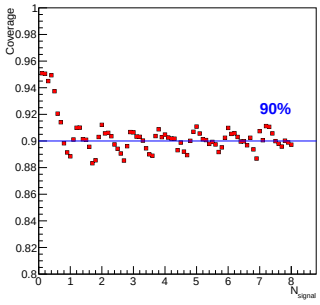

(a) Two-sided CIs, 10 targets, s>0

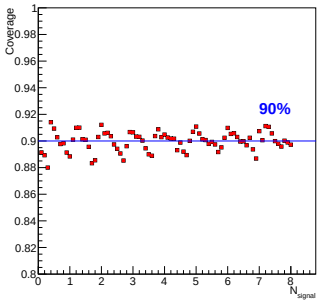

(b) Two-sided CIs, 10 targets, s free

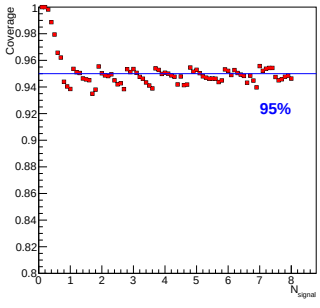

(c) Upper limits, 10 targets, s>0

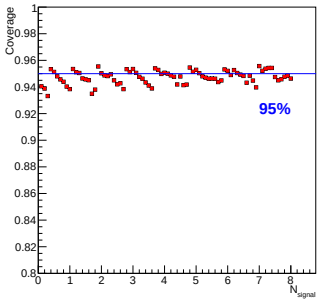

(d) Upper limits, 10 targets, s free

Figure 5.9: Coverage results from a simple Toy Monte Carlo test. We simulated 10 targets as Poisson processes with a background of 3. We made 10000 runs for each signal strength. The results are plotted for: (a) two-sided intervals, fitted signal constrained to be positive (b) two-sided intervals, fitted signal unconstrained (c) upper limits, fitted signal constrained to be positive (d) upper limits, fitted signal unconstrained.

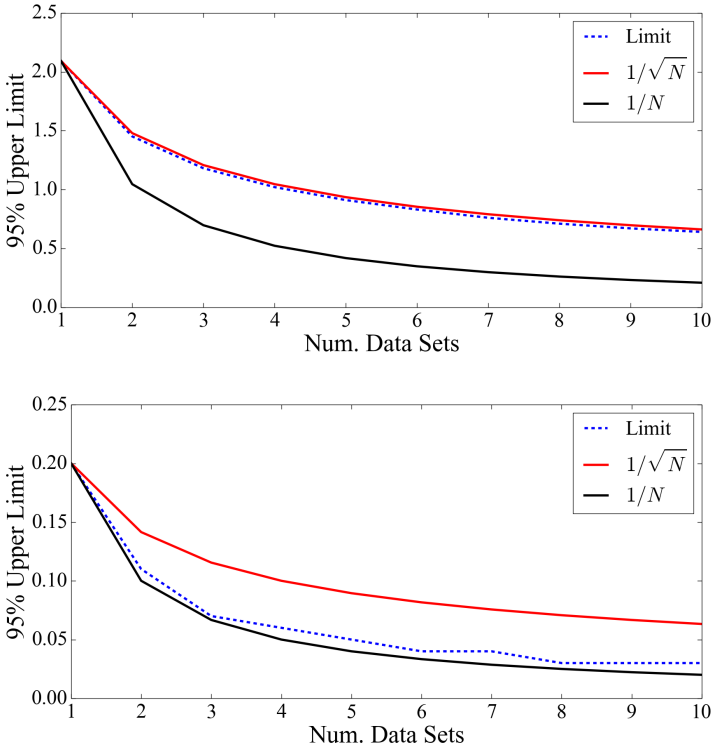

Figure 5.10: Both figures contain the 95% Upper Limit as a function of added targets, compared to $1/N$ and $1/\sqrt{N}$. In the upper plot, the signal-to-background is 1:10 with 100 total events in each set, and the parameter of interest is free to take any value in the fit. The limit follows the expected $1/\sqrt{N}$. If the case of very low background the limits will improve faster, as shown in the lower plot. Here the signal to background is 1:0.1. Figure from Anderson et al. [57].

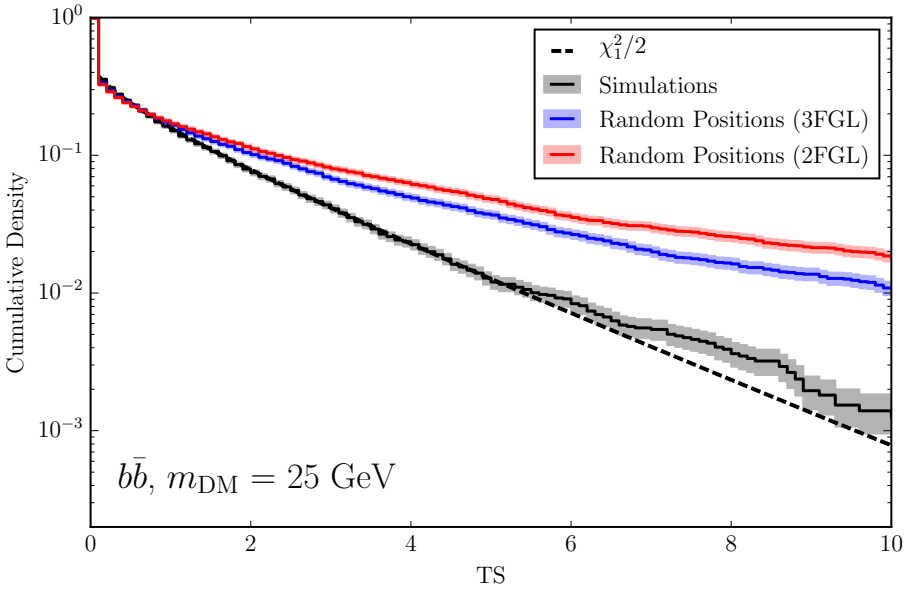

Figure 5.11: The TS distribution for a 25 GeV WIMP annihilating through the $b\bar{b}$ channel for three different setups: simulations using the Fermi-LAT Science Tools in solid black, random blank fields from data including the 3FGL catalog in solid blue, and random blank fields from data including the 2FGL catalog in solid red. The expected distribution from Chernoff's theorem is plotted in dashed black as a comparison [93]. The shaded bands are the estimated one sigma uncertainties. The results from simulations follows the expected distribution while the distributions using real data do not. Including more sources in the analysis of real data brings the distribution closer to the expected value. This is an implication that unresolved sources and poorly modeled backgrounds might cause this deviation. Figure credit: Ackermann et al. [45].

Chapter 6

Results of the Fermi-LAT dSph analyses

In the first dSph analysis published by the Fermi-LAT collaboration [27], individual DM limits for 8 dSphs were presented. However, since the DM particle properties are the same in all dSphs, we can use the joint likelihood method described in Chapter 5 to analyze a sample of dSphs. This method has now become the standard method for Fermi-LAT dSph analyses.

In our first study (Paper I) we analyzed 2 years of data targeting 10 dSphs. This analysis was the first to use this method and also the first to include the statistical uncertainties from the J factors. We used the Fermi Science Tools and implemented the *Composite2* code.

In our second study (Paper II) we updated to 4 years of data and analyzed more dSphs (15 in the combined fit and 25 in total). We also changed the method, using the 'bin-by-bin' likelihood analysis (described in Section 5.4) in order to reduce computational time and to obtain spectrally independent flux upper limits for the individual dSphs. We also took into account the spatial distribution of the dSphs to make a more realistic description.

A recent result, and the latest iteration of the Fermi-LAT dSphs analysis, uses 6 years of Pass-8 data [45]. This work is briefly discussed in Section 6.3. But several other results using Fermi-LAT data have been published and some of these will also be discussed in Section 6.3.

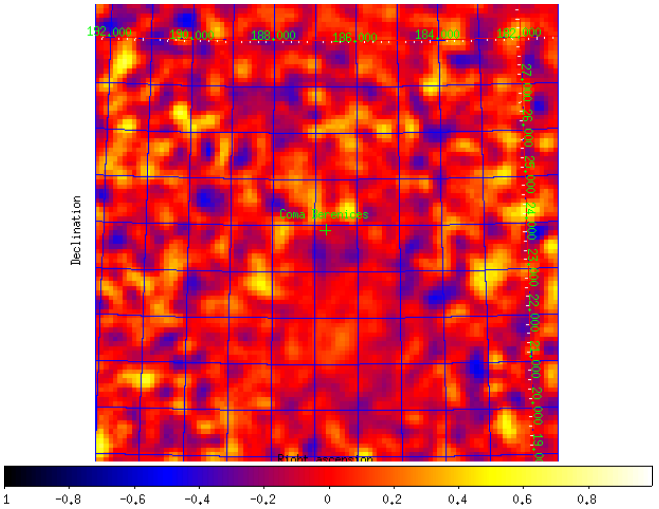

Figure 6.1: Residual map of the $10° \times 10°$ analysis region for Coma Berenices (the Model Map subtracted from the Counts Map and divided by the Model Map). The color bar goes from -1 (black) to 1 (white) and the map is smoothed with a Gaussian function with $\sigma = 1.5°$ to reduce statistical noise.

6.1 Paper I

In Paper I we used Pass-6 data and the corresponding P6V3 instrument response functions and the Diffuse event class with a high gamma-ray purity.

We selected ROIs of 10 degrees centered on each dSph. This is large enough to contain the point spread function at low energies and fit the background properly. Larger ROIs would give better background modeling, but we would risk getting a biased result from overlapping regions of interest. The counts maps showing the analysis regions for all 10 dSphs in Paper I are compiled in Fig. 6.2.

The Galactic diffuse emission component and the isotropic background component were modeled using recommended models for the Pass-6 data, *gll_iem_v02.fit* and *isotropic_iem_v02.txt*, respectively [6].

Point sources were taken from the 1FGL catalog [26] within 15 degrees of each dSph, but since we used 24 months of data we added sources from the unofficial two-year catalog where there were visible spatial residuals. The reason we chose a source region of 15 degrees is to take photons

leaking into the ROIs, due to the point spread function, into account.

A source that needed some extra care was the violently variable quasar in the Coma Berenices ROI, clearly visible in the counts map in Fig 6.2c. This source is named 1FGL J1224.7+2121 in 1FGL catalog (also named 4C +21.35, or PKS 1222+21) and is known to flare in radio, optical, x-ray and gamma. Agile and Fermi reported on a very intense gamma-ray flare in June 2010 [130, 195], but there has also been several earlier flares, e.g. [95, 105]. We managed to get a good fit, as can be seen in the residual map in Fig. 6.1. In later iterations of the Fermi source catalog (2FGL and 3FGL), this source has been modeled including the flares.

We selected an energy range from 200 MeV to 100 GeV and binned the data into 30 energy bins logarithmically spaced. We performed a spatial binning with a bin size of 0.1°. We also made cuts to minimize the contamination from photons coming from the Earth albedo, removing all events with a zenith angle larger than 100° degrees and time intervals where the targets are occulted by the Earth.

We analyzed four DM annihilation channels, $b\bar{b}$, $\tau^+\tau^-$, $\mu^+\mu^-$, and W^+W^-. The $b\bar{b}$ spectrum is representative for the spectra from the quark-antiquark annihilation channels, the $\tau^+\tau^-$ channel represents different shapes than the quark spectra (see Fig. 2.1), the $\mu^+\mu^-$ channel seemed to be favored in the context of the measured rise in the positron fraction [78], and the W^+W^- channel represents annihilation into bosons.

The resulting ULs for all channels are compiled in Fig. 6.3.

6.2 Paper II

For Paper II 4 years of Pass-7 reprocessed Fermi-LAT data was analyzed. We chose an energy range of 500 Mev - 500 GeV and binned the data in 24 logarithmically spaced energy bins to give 8 bins per decade, and 0.1° sized spatial bins. The new Pass-7 reconstruction and the longer exposure allowed for a higher high-energy cut. The CLEAN event class was used to further reduce the particle background contamination at high energies. The lower energy range was set to avoid any possible spectral dependence in the 'bin-by-bin' pipeline arising from the rapidly changing effective area for low energies. Here the square spatial map was optimized to be 14° × 14° which is the largest square possible to fit into a 10° circular ROI. Sources from 2FGL within 15° of each target were included in the models, and each ROI was scanned for new resolvable

point-like sources that were later added to the models. We used the corresponding IRFs (P7REP_CLEAN_V15) and diffuse background models (*gll_iem_v05.fit* and *iso_clean_v05.txt*). The novel 'bin-by-bin' likelihood technique was introduced and a great number of systematic studies were presented, of which a subset are briefly described in Chapter 5 and Chapter 7.

For Paper II an independent analysis was performed using the *Composite2* pipeline from Paper I . The energy range was chosen to be 100 MeV - 500 GeV instead of 500 MeV - 500 GeV to fully utilize the fact that the *Composite2* code can be used at low energies, but the number of energy bins was chosen to be the same as in Paper II (24 bins). In the Paper I pipeline the normalizations of all point sources within 5 deg were left free, but with more sources (2FGL instead of 1FGL) and more dSphs included in the analysis, point sources had to be fixed to their best fit value in the combined fit since MINOS does only take 100 free parameters. Just including 15 dSphs and fitting the cross section, including their J-factor uncertainties, and fitting the diffuse backgrounds, will result in 46 free parameters (1 for the cross section and 3×15 for the J factors and the two background components). The normalizations of the background models were free in both the individual and combined fits, and even though the point sources were fixed here, there is some room for more free parameters and very near-by sources could be left free in the combined fit.

1FGL contains 1451 sources [26] while 2FGL contains 1873 sources [170] (sources characterized in the 100 MeV - 100 GeV range for both catalogs). As an example, the Draco source region in Paper I contains 27 sources from 1FGL while the same source region in Paper II contains 35 sources from 2FGL and 5 additional sources. The different spectral plots from the fits are presented in Fig. 6.4.

There were some initial excesses in the Pass 7 data, and an example from the independent analysis (not presented in the paper) is shown in Fig. 6.5. A detailed study of the TS distribution for the 'bin-by-bin' analysis, described briefly in Chapter 5, concluded that the excesses were not significant (the global significance of the largest excess in the 'bin-by-bin' analysis is $p \approx 0.08$).

A comparison between this complementary analysis and the analysis published in Paper II is presented in Section 7.1.1. The published ULs from Paper II are collected in Fig. 6.6.

6.3 Results from other publications

The first dSph publication by the Fermi-LAT collaboration was published in 2010 and targeted 14 dSphs using 11 months of data [27], but the dSphs were analyzed separately. The setup of this paper is compared to the setup of Paper I and Paper II in Section 7.1.2.

The results for Draco from this analysis, and the combined analysis results from the other dSph publications presented here, are compiled in Fig. 6.7.

Another result published at the same time as Paper I is the analysis by Geringer-Sameth et al. [118] where they use Neyman construction for a joint analysis of 7 dSphs. In this analysis they do not use the conventional background models, but instead they measure the background in a sideband close to each dSph. They only include 7 dSphs because they avoid crowded regions to get proper sideband measurement (e.g. Coma Berenices is not included), they use 3 years of Pass 7 data, and since they are not fitting the background, they use ROIs of 0.5°. They use the J-factors from Paper I but they do not include the J-factor uncertainties (they do present a 95-percentile of the systematic uncertainty).

Maziotta et al. use a model-independent analysis where they unfold and stack the data and calculate upper limits using a Bayesian approach [161]. They perform both a stacking analysis where all dSphs are weighted equally, and a composite analysis where they weight the dSphs according to their J factors. They do include uncertainties from the J factors but the impact on the limits is small. The backgrounds are sampled in annuli surrounding each dSph. In Fig. 6.7 the result of the composite analysis is plotted with the results from the other dSph analyses.

An update to the Geringer-Sameth analysis using 70 months of P7REP data of the ULTRACLEAN class was published in 2015 [115]. The analysis is similar, but not identical, to their earlier work and they describe it as an update and a generalization of the previous study. They present a joint analysis of 20 dSphs with J factors derived in their accompanying publication [116], briefly mentioned in Section 4.3. They discuss the fact that the Fermi-LAT collaboration found excesses is probably due to the modeling of the backgrounds in our work (Paper II), while their results are consistent with background as they sample the background around each dSph and mask all catalog sources. They also mention that the calibration of the significance in Paper II using blank fields yields significances similar to theirs. As discussed in Section 5.6.4, we are well aware of

the fact that the TS distribution obtained from real data is not identical to the theoretical distribution and we do take this into account.

With the new Pass-8 data release, an updated Fermi-LAT collaboration analysis using 6 years of the latest data was published [45]. The analysis make use of the new Pass-8 features and analyze the data using the different PSF classes. The setup and the analysis pipeline is the same as for Paper II apart from the new treatment of the data and that the J-factor uncertainties are included with a slightly different shape of the likelihood (discussed in Section 5.5). Systematic uncertainties and statistical properties are also thoroughly investigated. This analysis gives the most constraining limits to date for gamma-ray searches in dSphs.

As can be seen in Fig. 6.7, there is a spread in the results arising from using different data sets, different number of targets, and different analysis methods. Abdo et al. [27] is the only limit plotted for a single dSph (Draco) and with the least amount of data, hence it is also the least constraining. The Geringer-Sameth et al. limits [118, 115] are, as is the Abdo et al. limit, for nominal values for the J-factors, i.e. no J-factor uncertainties are included. Geringer-Sameth et al. do, however, make a thorough investigation of how the statistical and systematic uncertainties affect their limits, but that is not included in this plot. The Maziotta et al. result is comparable with the other results despite the fact that the analysis method is different (unfolding and data stacking, compared to forward folding and joint likelihood). As will be discussed in Section 7.1.3, the limits using Pass-7 data (Paper II) are less constraining than the limits using Pass-6 data (Paper I). The Passes are, however, internally consistent and analyzing 4 years of Pass-7 data will yield more constraining limits than analyzing 2 years of Pass-7 data. The limits using 6 years of Pass-8 data are the most constraining.

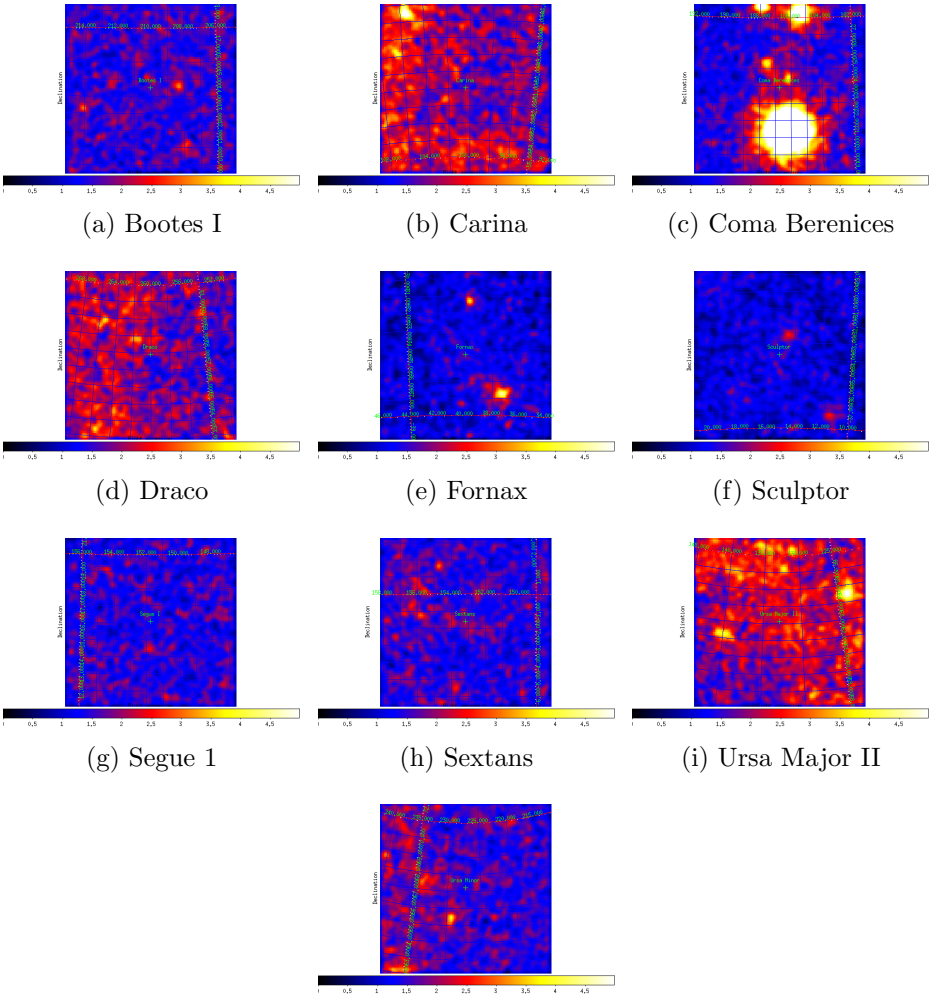

(a) Bootes I (b) Carina (c) Coma Berenices

(d) Draco (e) Fornax (f) Sculptor

(g) Segue 1 (h) Sextans (i) Ursa Major II

(j) Ursa Minor

Figure 6.2: Counts maps of the $10° \times 10°$ analysis regions of the 10 dSphs included in Paper I . The color bar goes from 0 (black) to 5 (white) and the maps are smoothed with a Gaussian function with $\sigma = 1.5°$ to reduce statistical noise .

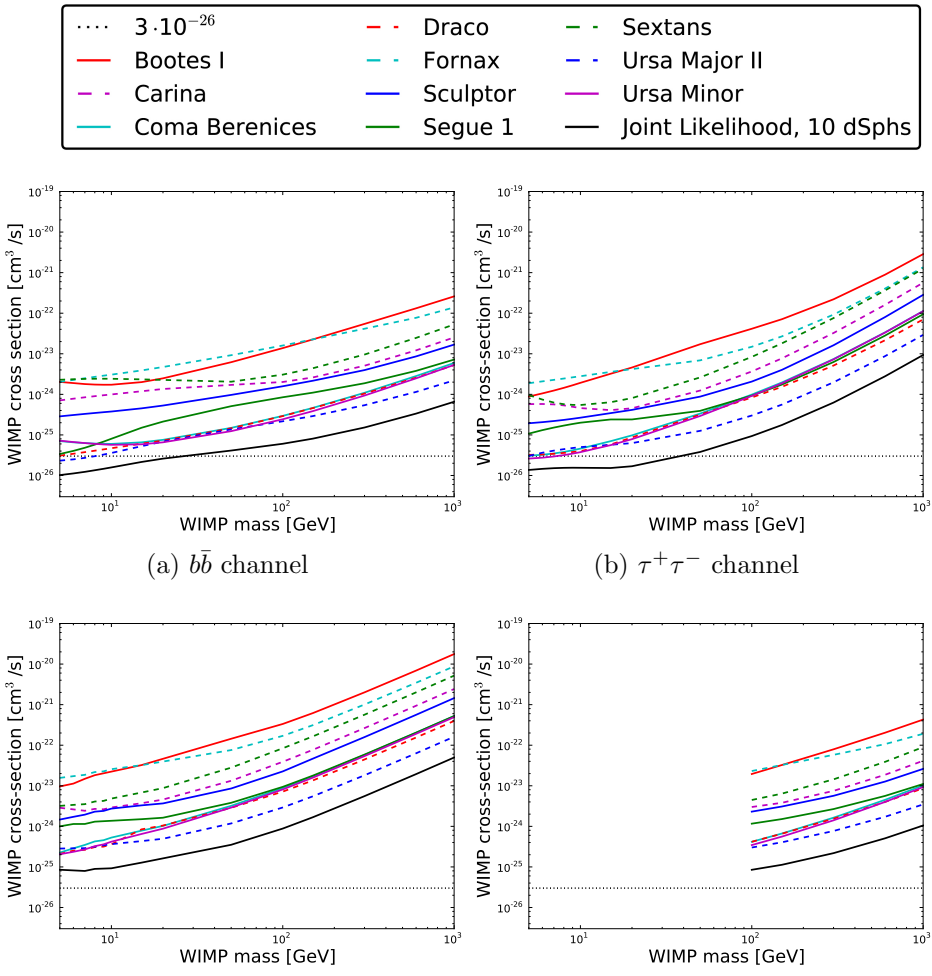

(a) $b\bar{b}$ channel (b) $\tau^+\tau^-$ channel

(c) $\mu^+\mu^-$ channel (d) W^+W^- channel

Figure 6.3: Individual and combined upper limits for the four annihilation channels analyzed in Paper I $b\bar{b}$ (a), $\tau^+\tau^-$ (b), $\mu^+\mu^-$ (c), and W^+W^- (d)

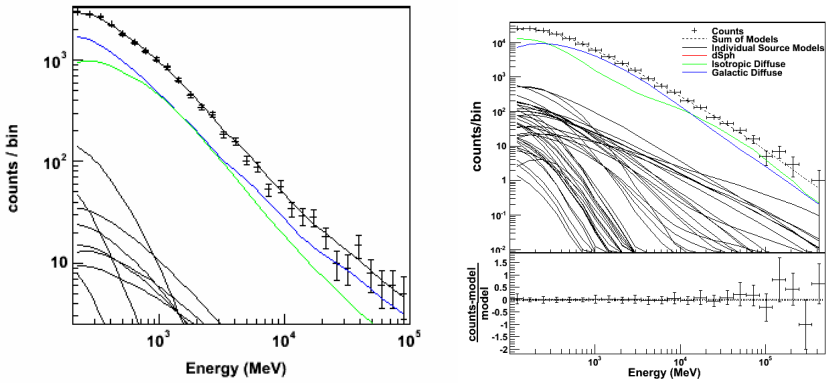

Figure 6.4: Spectral plots prepared for Paper I (left) and Paper II (right) showing the impact of using 1FGL versus 2FGL for Draco. In the left plot there are 27 1FGL sources, but many are to weak to be seen on this scale. In the right plot there are 40 background sources in total. The isotropic diffuse model is plotted in green, the galactic diffuse model in blue and the putative DM source in red (not visible). Catalog sources and additional point sources are plotted in black. The total model is also in black. Note that the scales in the plots are different. Also note that these plots were prepared for Paper I and Paper II respectively, and use different data and different background models. We use *gll_iem_v02.fit* and *isotropic_iem_v02.txt* for Paper I and *gll_iem_v05.fit* and *iso_clean_v05.txt* for Paper II .

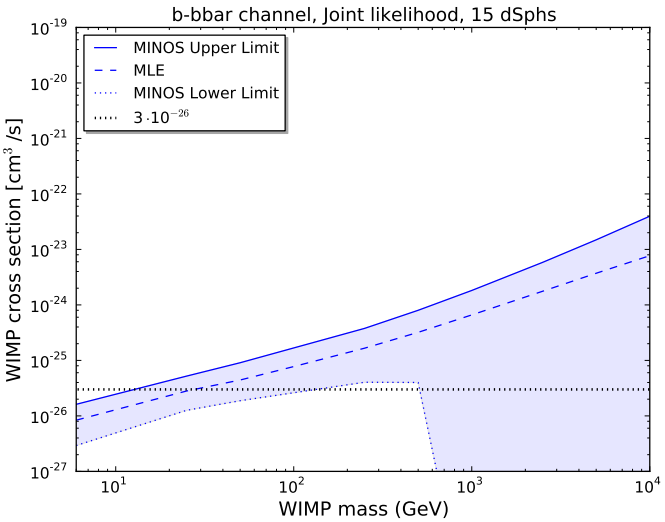

Figure 6.5: Result of the independent *Composite2* analysis for Paper II using Pass-7 reprocessed data. The UL is plotted in solid blue, the MLE is plotted in dashed blue, and the LL is plotted in dotted blue. The full CI is shaded blue. At DM masses below 500 GeV, two-sided CIs are obtained. The excess was found to be insignificant. The TS distribution does not follow asymptotic theorems, partly due to unresolved background sources, and the actual significance (for the 'bin-by-bin' analysis) was obtained from random sky positions.

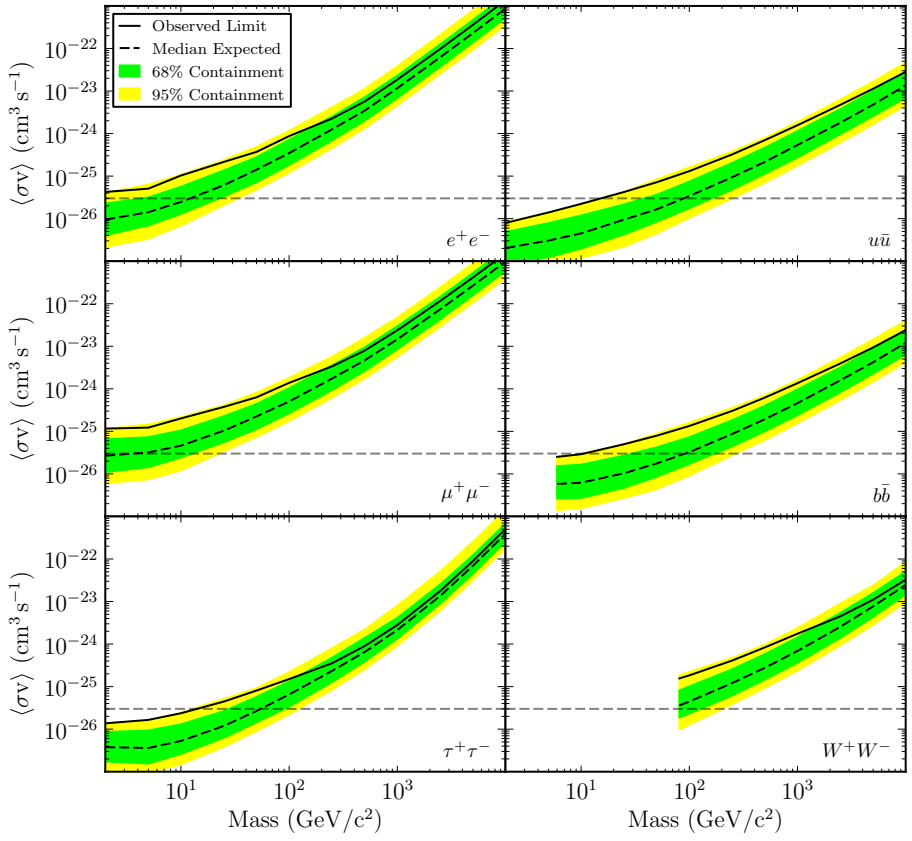

Figure 6.6: Combined upper limits for the 15 dSphs and six annihilation channels presented in Paper II . The measured ULs are plotted in solid black, and the mean expected limits from random sky positions are plotted in dashed black with the 68% containment band in green and the 95% containment band in yellow.

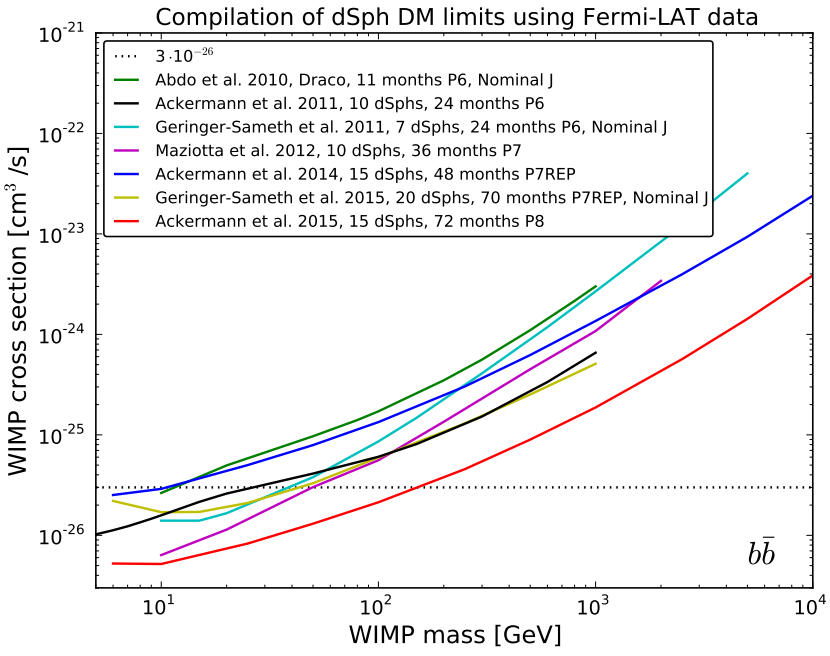

Figure 6.7: Compilation of the published ULs for the $b\bar{b}$ channel from a selection of dSph analyses using Fermi-LAT data. Note that the different publications use different data, different analysis setup, and different methods. The upper limits plotted, in chronological order, are from Abdo et al. 2010 (green) [27], Ackermann et al. 2011 (black, Paper I) [35], Geringer-Sameth et al. 2011 (cyan) [118], Mazziotta et al. 2012 (magenta) [161], Ackermann et al. 2014 (blue, Paper II) [43], Geringer-Sameth et al. 2015 (yellow) [115], and Ackermann et al. 2015 (red) [45].

Chapter 7

Systematic studies

In preparation of Paper I , Paper II , and [218] (paper not included in the thesis), we performed many tests to verify the methods and pipelines. A subset of these tests are presented here, with focus on comparing the pipelines in Paper I and Paper II and the different setup of the different generations of the Fermi-LAT dSph work. We also test some of the individual features of the *Composite2* code and the 'bin-by-bin' pipeline.

The tests are described in the following section, followed by a compilation, and short discussion, of the results.

7.1 The different tests

7.1.1 Full likelihood (Composite2) vs 'bin-by-bin' pipeline

One of the main differences in Paper I vs Paper II is the change of pipeline. In Paper I we used the *Composite2* code in the Fermi Science Tools and in Paper II we used the 'bin-by-bin' pipeline, both described in Chapter 5. To compare the two codes properly, the exact same setup (exactly the same data, model files, cuts, and version of the Fermi Science Tools) was used for both pipelines.

In the preparation of [218], we tested the pipelines for four galaxy clusters: A3526, Fornax, M49, and NGC4636. Since we test for differences in the pipelines, the result of the test does not depend on the target itself, and the result for clusters is valid for dSphs under the same conditions. We modeled the clusters as point sources and as extended sources, but did not include J-factor uncertainties. For this test we used the same setup as in Paper II (4 years of Pass-7 data). The results of the tests for both point sources and extended sources can be seen in Fig 7.1. When using

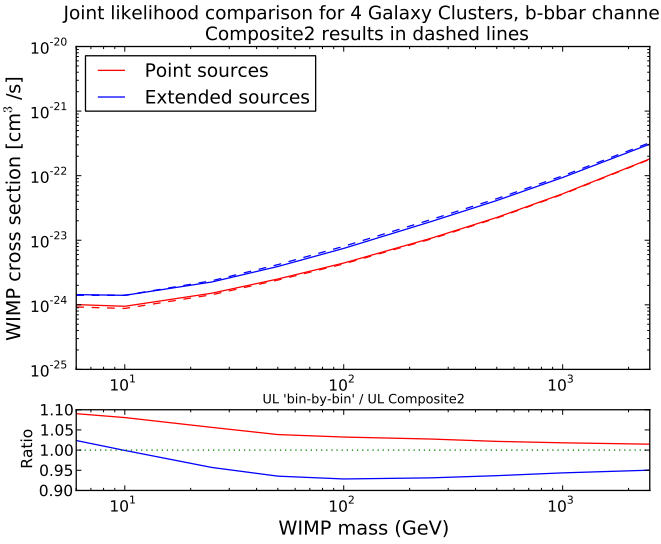

Figure 7.1: Comparison of the resulting ULs using *Composite2* (dashed lines) and the 'bin-by-bin' (solid lines) pipelines for an analysis of four galaxy clusters, using identical setup for the two analyzes. Results modeling the clusters as point sources are plotted in red and as extended sources in blue.

an identical setup, the two analysis pipelines yield very similar results, both in the case of modeling the targets as point sources and as extended sources (the difference is <9%, and the mass-averaged difference is 5% for extended sources and 4% for point sources).

For Paper II an independent analysis was performed using the pipeline from Paper I , but still yielding comparable results. In this complementary analysis, the analysis was independent and the setup was therefore not identical to the setup of the 'bin-by-bin' analysis presented in the paper. As described in Section 6.2, the energy range was set to 100 MeV - 500 GeV instead of 500 MeV - 500 GeV, point sources had to be fixed to their best fit value in the combined fit, but the normalizations of the backgrounds were free in both the individual and combined fits. In the 'bin-by-bin' analysis presented in Paper II all nuisance parameters were fixed att their best fit value in the 'bin-by-bin' fit.

The result of this complementary analysis is shown in Fig. 7.2. At the lowest mass point the difference is quite large, but the low-energy cut is lower for the *Composite2* analysis, yielding a lower limit since a larger

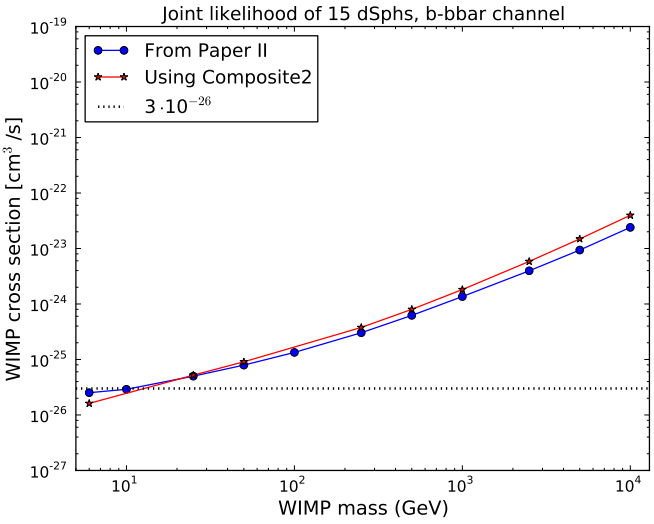

Figure 7.2: Comparison of the resulting ULs using *Composite2* and the 'bin-by-bin' pipelines for the independent supplementary analysis for Paper II .

part of the DM spectrum can be fitted at low masses.

In the *Composite2* analysis the background normalizations were free in the combined fit, while in the 'bin-by-bin' fit they are fixed at their best fit value. But the difference is small in comparison to the effect of other systematics (as is shown here for the four galaxy clusters, see Fig. 7.1), and the statistical uncertainties in the background models are therefore neglected in the 'bin-by-bin' pipeline.

7.1.2 Setup from different iterations of the dSph analysis

The Fermi-LAT collaboration has to date published four iterations of the DM analysis of dSphs [27, 35, 43, 45]. There is a difference in the binning and energy cuts in these publications, and here we test the resulting difference on the analysis of the Draco dSph.

The first iteration, [27], used eleven months of Pass-6 data of the Diffuse event class, which is recommended for point source analysis. To accommodate the large PSF at low energies a ROI of 10 degrees was chosen. The energy range analyzed was 100 MeV - 50 GeV (Also a dedicated high-energy analysis 1 GeV - 50 GeV was performed, where 5 degree ROIs

could be used due to the smaller PSF at higher energies). Since no official LAT catalog was completed at the time, a preliminary version of the 11 month LAT catalog was used.

The second iteration, Paper I [35], used 24 months of Pass-6 data of the Diffuse event class. According to the recommendations at the time we used an energy range of 200 MeV - 100 GeV. Binning in both energy and space was increased to 30 logarithmically spaced energy bins and 100×100 spatial bins. The recommended cut on the rocking angle was updated to 52 degrees. The ROIs have a radius of 10 degrees, but in the analysis a 10 degree square spatial map was used. Even though the circular ROIs overlap, the spatial maps do not, and bias from overlapping ROIs is avoided. The official 1FGL catalog was used, but additional sources were added manually since we now had 2 years of data, and a flaring source in the Coma Berenices ROI.

In the third iteration, Paper II [43], the dSphs were modeled as extended sources and 4 years of Pass-7 reprocessed data of the CLEAN event class was used. The chosen energy range was 500 MeV - 500 GeV. The number of energy bins was decreased to 24 logarithmically spaced energy bins for the use of the 'bin-by-bin' analysis method, and the square spatial map was optimized to have a side of 14 degrees, binned in 0.1° sized spatial bins. In the complementary *Composite2* analysis, there was no need to cut at 500 MeV so this analysis gave stronger limits for low WIMP masses as described in section 7.1.1.

The forth iteration, [45], using Pass-8 data, has the same setup as the third paper and is therefore not tested here.

The different analysis setup parameters are compiled in Table 7.1

For this test we employed the different setups on 2 years of Pass-7 reprocessed data for observations of the Draco dSph. By using the same dataset for all analyses we remove the impact of the data processing. We also used the same IRFs (P7REP_CLEAN_V15), the same catalog (2FGL), and the 'bin-by-bin' pipeline from the third paper, [43]. We modeled Draco as a point source and included the J-factor uncertainty. We used a maximum zenith angle cut of 100 degrees and a rocking angle cut of 52 degrees for all setups, so the impact of these choices is not tested. The resulting ULs are presented in Fig. 7.3.

In the lower panel of Fig. 7.3, the values for the setup from the first iteration and the setup from the third iteration are compared to those of the setup from the second iteration. The setup from the first iteration has a comparable low-energy cut to the setup from the second iteration

	First iteration [27]	Second iteration [35]	Third iteration [43]
Time	11 months	24 months	4 years
IRFs	P6_V3_DIFFUSE	P6_V3_DIFFUSE	P7REP_CLEAN
Low-energy cut	100 MeV	200 MeV	500 MeV
High-energy cut	50 GeV	100 GeV	500 GeV
Nr. of Energy bins	15	30	24
Max. Zenith angle	105 deg	100 deg	100 deg
Nr. of Spatial bins	64×64	100×100	141×141
Size Spatial bins	0.15625 deg	0.1 deg	0.1 deg
Rocking angle	43 deg	52 deg	52 deg
Source catalog	preliminary 11 month	1FGL + additions	2FGL + additions

Table 7.1: The different parameter choices for the first three Fermi-LAT dSph analyses.

and therefore gives comparable limits at low masses, while the setup from the third iteration has a higher low-energy cut and give less constraining limits for low masses. For high masses, the setup from the first iteration has a lower high-energy cut yielding less constraining limits while the setup from the third iteration has a higher high-energy cut yielding more constraining limits.

Because of the possible impact of the effective area at low energies for the 'bin-by-bin' pipeline, we also compare the two pipelines for all the different binning using the same setup as in the previous test. Although there is some difference between the pipelines for this individual limit, the effect of the binning is the same, and the discussion above is still valid. The results of this cross check are plotted in Fig 7.4.

7.1.3 Upgrade from Pass 6 to Pass 7

In Paper I we used Pass-6 data and in Paper II we updated to Pass-7 reprocessed data. As a first test (before we upgraded to reprocessed data) we compared the published result to the same setup using Pass-7 data with the *Composite2* pipeline. The result for different event classes using 2 years of data is shown in Fig. 7.5, where the Pass-6 Diffuse class should be compared to the Pass-7 SOURCE class as described in Section 3.2. (The effective area for different event classes in Pass 6 and Pass 7 was plotted in Fig. 3.2.) Note that the diffuse background models are different for the different datasets and that the Pass-6 analysis uses the 1FGL catalog with some additions while the Pass-7 analysis uses the 2FGL catalog. Apart from that, the setup is identical to the setup of Paper I .

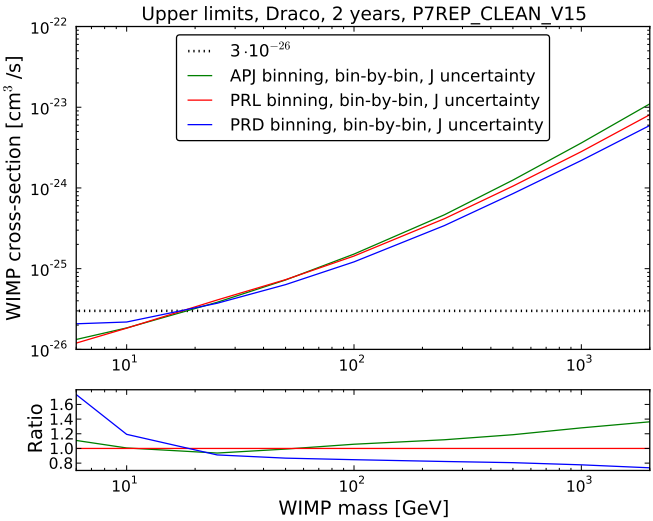

Figure 7.3: Comparing the binning from the first Fermi-LAT dwarf paper [27] (here called APJ binning), the second Fermi-LAT dwarf paper [35] (here called PRL binning), and the third Fermi-LAT dwarf paper [43] (here called PRD binning) using 2 years of Pass-7 reprocessed data. In the upper panel, ULs for the three setups are presented. In the lower panel, the ULs from the first and third setup are compared to the ULs from the second setup.

The Pass-7 data selection and setup yield weaker limits by a factor of ~ 2.4, but is internally consistent. Comparing the limits for 24 months to the limits for 43 months we find 52% difference in the ULs (to compare with 24/43= 56%).

7.1.4 Using different J factors

In the preparation of Paper I we tested J factors from Charbonnier et al. [89] as a comparison to the J factors used in our analysis. We made the comparison for a 100 GeV DM particle annihilating through the $b\bar{b}$ channel, but we only have Charbonnier et al. values for the 'classical' dSphs. Note that the fact that we include the J-factor uncertainties in the UL calculations results in that the correspondence between UL and J-factor is not always obvious. This test was performed using the *Composite2* code with the same setup as in Paper I .

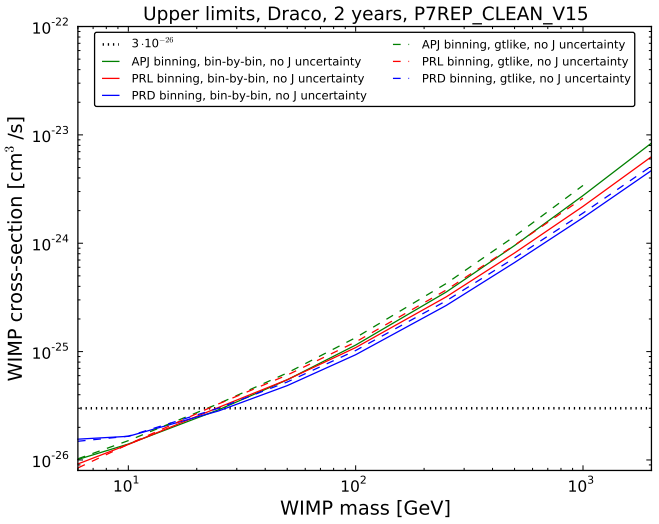

Figure 7.4: Comparing the binning from the first Fermi-LAT dwarf paper [27] (here called APJ binning), the second Fermi-LAT dwarf paper [35] (here called PRL binning), and the third Fermi-LAT dwarf paper [43] (here called PRD binning) using 2 years of Pass-7 reprocessed data. ULs for the three setups are presented for the 'bin-by-bin' pipeline (solid lines) together with the *Composite2* analysis (dashed lines).

Where the errors from Charbonnier et al. are asymmetric, we chose the larger error to be conservative. It is important to note that we include the errors in the same way for all J factors (as described in Section 5.5), even though we do not know the likelihood from the Charbonnier et al. analysis.

Substituting our J factors for the 'classical' dSphs for the J factors from Charbonnier et al. the combined UL of the 10 dSphs only changes with 8.6% for a DM particle with a mass of 100 GeV annihilating through the $b\bar{b}$ channel. The fact that the effect on the joint limit is so small is an example of the statistical strength of the joint likelihood method. For the individual dSphs the difference is larger, as can be seen in Fig 7.6. The individual statistical uncertainties can average out when combined in the joint likelihood, but in case of systematic biases, the result might not be conservative enough.

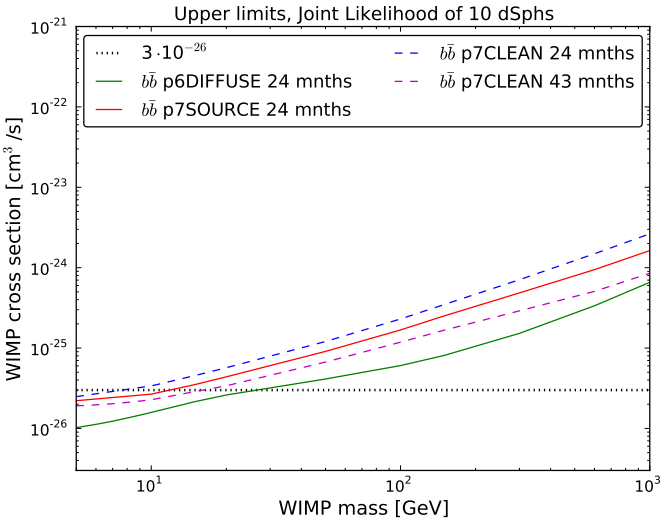

Figure 7.5: The resulting upper limits using the Paper I pipeline for 2 years of data for different data sets are shown. For comparison, results for 43 months is also plotted. The mass-averaged difference between 24 months and 43 months (dashed lines) is 52% (to compare with $24/43 = 0.56$), and the mass-averaged difference between 24 months Pass-6 data and 24 months Pass-7 data (solid lines) shows that the limits increase by a factor of 2.4 when moving to Pass 7.

7.1.5 Tying the backgrounds

One improvement that was made to the first Science Tools script for the joint likelihood (*CompositeLikelihood*) was the update to *Composite2*, where several parameters can be tied over the different ROIs, compared to just one in the first iteration.

We performed some initial tests exploring the results of tying the diffuse background model components over the different ROIs in the joint likelihood fit. The isotropic diffuse normalization should be the same at high latitude so this parameter should be possible to fit jointly for all dSphs. The galactic diffuse model is a spatial map and should be more accurately fitted when fitted against multiple ROIs than when fitted to one single ROI. If the models are correct, this will give a better value for the model parameters than fitting them individually in a small (10 deg) ROI and at the same time include their model uncertainties. Trusting the

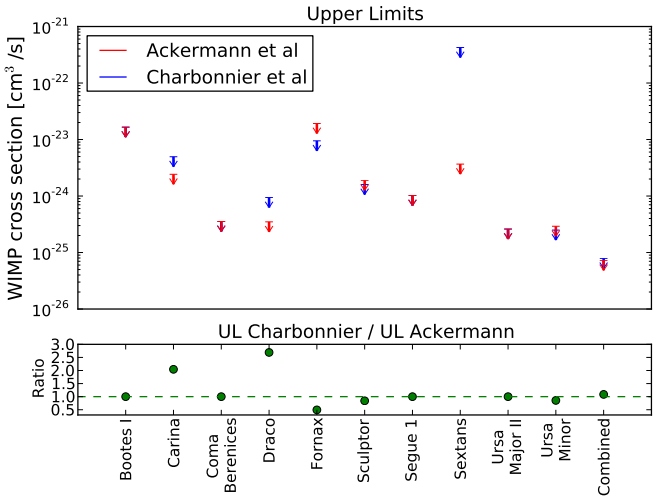

Figure 7.6: In the upper panel the upper limits from using J factors from Charbonnier et al compared to our values are plotted. Since Charbonnier et al. only analyze the 'classical' dSphs, we lack values for Bootes I, Coma Berenices, Segue 1 and Ursa Major II. In the lower panel, the ratio for the ULs using the Charbonnier J factors compared to using our J factors is plotted. The ratio for Sextans is 116 (due to the large uncertainty) and does not show in the plot.

model, the all-sky best fit parameters could be used in the analysis and fixed in the fit, but in this case we optimally would propagate the model uncertainty into our final results. Therefore fitting the background model parameters over the different ROIs using the joint likelihood would be a way to include the statistical uncertainties while fitting the backgrounds to a larger dataset than a single small ROI. At low latitudes, the background models are less accurate, but at high latitudes this could be a possible improvement to the analysis.

We found that, when fitting one background component jointly and the other individually, the ULs did not change much since the individually fitted background would compensate if the jointly fitted background would give a bad fit. This is no surprise since the two background models are developed together. The same can be observed for a single ROI if one background component is fixed. The resulting ULs for a set of 8 dSphs using 21 months of Pass 6 data is shown in Fig. 7.7. The best fit val-

ues for the normalization parameters from individual fits, and when tying the background components, for the same test on 8 dSphs are plotted in Fig 7.8, for data and simulation. For the simulated data the result is intuitive, tying the backgrounds will give MLEs that are closer to the nominal value (1 in this case) when both background models are fitted jointly, and MLEs that are close to the mean of the individual MLEs when only tying one background model component. The individual MLEs are spread symmetrically around the nominal value. For real data on the other hand, the result is much less intuitive and the degeneracy of the models seems to have a larger impact. Tying one background component gives similar result as for the simulation, but when tying both background components, the MLEs for the two components interchange and the MLE of the isotropic diffuse component is closer to the mean of the galactic diffuse component, and vice versa.

For both backgrounds fitted jointly, the ULs are more constraining at low WIMP masses but the spectral residuals are larger. As an example, the spectral residuals for Ursa Minor with four different setups are shown in Fig. 7.9. When analyzing simulated data, the difference in the residuals is not significant (panel (a) in Fig. 7.9), but this changes for real data (panel (b) in Fig. 7.9) where we get a large offset. Increasing the number of energy bins decreased the difference slightly in the residuals (panel (c) in Fig. 7.9).

We decided not to use this feature at the time, and in Paper I we leave the background parameters free and fit them individually in each ROI yielding conservative results at low WIMP masses.

7.2 Test results

From the results presented above, a few generalizations can be made. It is however important to note that the setup has to be chosen, not from these generalizations, but from the problem at hand. Conservative limits will be obtained when having a smaller energy range. More constraining limits will be obtained by increasing the energy range. The impact of fixing or tying the background components will depend on the background fluctuations. In case of a downward background fluctuation, fixing or tying the background components will yield more constraining limits, but the combined analysis is less sensitive to fluctuations since they are more likely to average out over the ROIs.

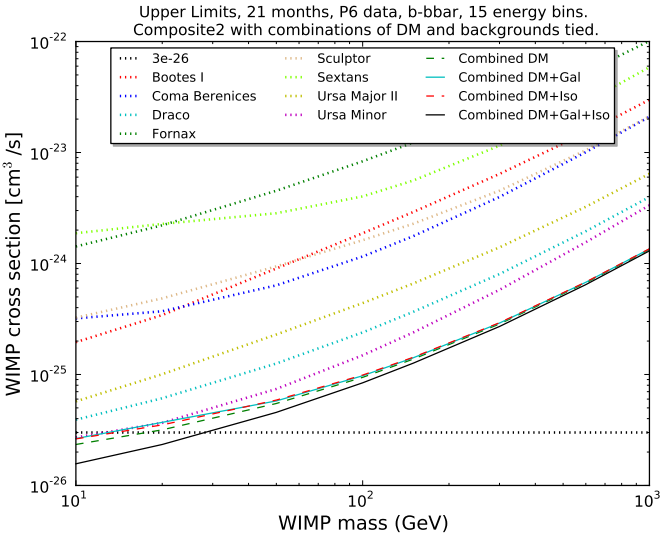

Figure 7.7: 98% Upper Limits for different choices of tied parameters. The individual limits for the different dSphs are plotted in dotted lines. Tying both background parameters (black solid line) yield stronger limits over the entire mass range, but specifically at low mass. Tying only one background parameter yield slightly weaker limits (cyan solid line and red dashed line) than when only tying the DM cross section (green dashed line).

For Paper II many systematics tests were made and presented in detail in Section VI of the paper. The uncertainties from the instrument performance (effective area, PSF, energy dispersion) were quantified using a set of 'bracketing IRFs'. The total effect on the combined analysis was in the order of 10% - 15%. The uncertainties in the background models were quantified by using a set of 8 reasonably extreme models developed to test systematic effects in the analysis of Supernova remnants [102]. These models were obtained through varying input parameters in the GALPROP code, e.g. the size of the cosmic-ray propagation halo and the distribution of cosmic-ray sources. The alternative models do however neither span the full uncertainty nor do they bracket the official model. The impact on the combined results is small, <10%. The spatial distribution of the dSphs is not known and to quantify the arising systematic effects the dSphs were modeled with Burkert profiles and different NFW profiles. The resulting impact on the combined limits is <20%.

Test	Low Mass	High Mass	Mass Averaged	Reference
Pipeline	+2%	-5%	5%	$b\bar{b}$ only, see Fig. 7.1
Setup versions	+73%	-27%	24 %	$b\bar{b}$ only, see Fig. 7.3
P6 vs P7	+116%	+148%	137%	$b\bar{b}$ only, see Fig. 7.5
Other J factors			8.6% at 100 GeV	$b\bar{b}$ only, see Fig. 7.6
Tying bkgr	+49%	+3%	17%	$b\bar{b}$ only, see Fig. 7.7
IRFs	<15%	<12%		Table VIII in Paper II
Diffuse	<10%	<3%		Table VIII in Paper II
Extension	<7%	<14%		Table VIII in Paper II

Table 7.2: Impact of different systematic effects on the combined upper limits

A compilations of the impact of the different tests is presented in Table 7.2. The largest effects arises when comparing Pass-6 and Pass-7 data ($\sim$ 137%, originating from a combination of the change in event selection, the new IRFs, new point source catalog, and the new background models) and when changing the low-energy cut to 500 MeV instead of 200 MeV ($\sim$ 73%, originating from the fact that a larger part of the low-mass DM spectrum can be fitted). But tying the background parameters across the ROIs also gives a significant effect ($\sim$ 17%), mainly at low WIMP masses.

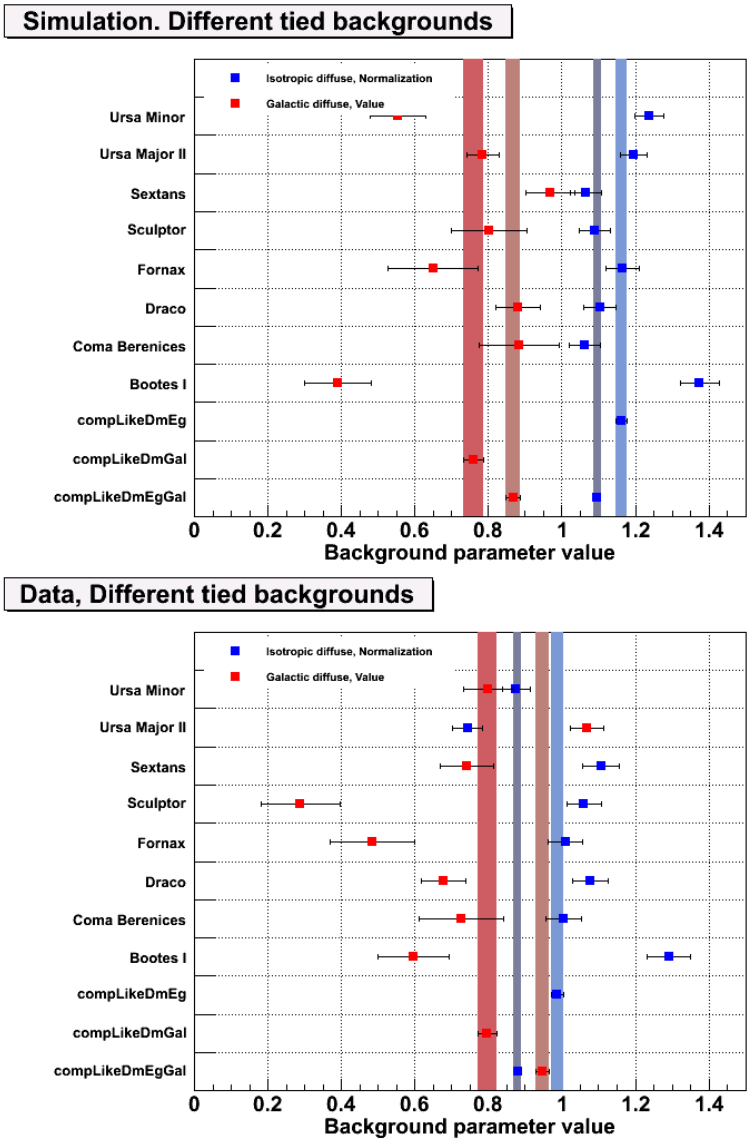

Figure 7.8: The MLEs and corresponding errors for the normalization parameters of the diffuse background components (the galactic diffuse model in red and the isotropic diffuse model in blue) plotted for individual fits and three combinations; DM and isotropic diffuse components tied (compLikeDmEg), DM and galactic diffuse components tied (compLikeDmGal), and all three components tied (compLikeDmEgGal). The shaded regions are plotted as guide to the eye for the values of the tied fits. In the upper panel the results for simulated data are plotted and in the lower panel the results for real data are plotted.

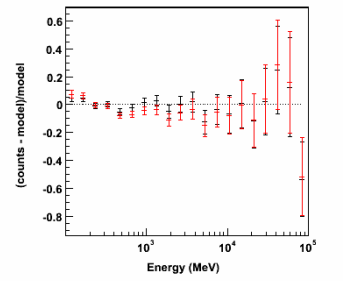

(a) Ursa Minor, 24m simulation, all tied

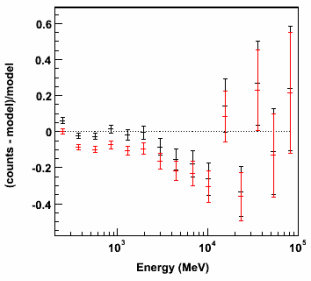

(b) Ursa Minor, 24m data, all tied

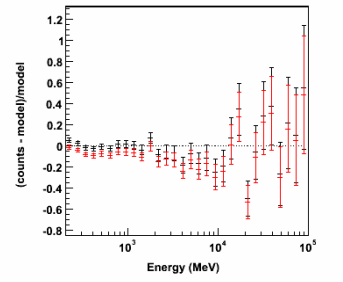

(c) Ursa Minor, 24m data, all tied

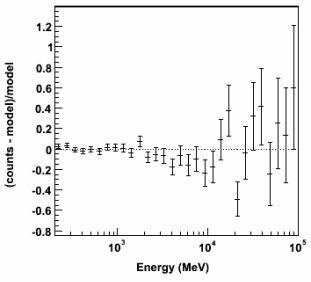

(d) Ursa Minor, 24m data, Paper I

Figure 7.9: Residual plots for Ursa Minor for different setups. Note the different scales on the y-axes. In the combined fit, 8 dSphs are fitted together. In panel (a) the residuals for tying both background components are shown using 1 year of simulated data. The residuals for the individual fit are plotted in black and the residuals after the joint likelihood fit are overplotted in red. In panel (b), corresponding residuals for 24 months data are plotted and the difference when tying the background parameters is clearly noticeable. In panel (c) we increase the number of energy bins to 30 and the difference is slightly smaller. Panel (d) shows the residuals from the individual fit of the published result, Paper I , as comparison. All fits are for a 100 GeV DM particle annihilating through the $b\bar{b}$ channel.

Chapter 8

Outlook

In this thesis I have presented two Fermi-LAT dSph analyses using the novel and powerful joint likelihood technique. The obtained upper limits in Paper I were the most robust and most constraining at the time of their publication. The Fermi-LAT collaboration continues to deliver robust and constraining limits with the new Pass-8 dSph analysis [45], and future analyses have bright prospects, not only by including more data, but from including more newly found dSphs, collaborating with other experiments, and further refining the analysis method.

Although many new dwarfs have been found, there are still many to come. The first annual release of DES data only covered about a third of the DES sky coverage, but the second release covers almost the full DES footprint. More dSphs will most certainly be found. Hargis et al. [123] predict that $\lesssim 100$ regular and a few hundreds of 'hyperfaint' dwarfs will be found with DES and the Large Synoptic Survey Telescope (LSST) within 300 kpc with a full sky coverage, but the uncertainties are very large. However, He et al. finds that this will only result in a factor $\sim$2-4 increase in Fermi-LAT sensitivity, but that does not include the predicted 'hyperfaint' dwarfs so the predicted increase in sensitivity might be very conservative [125]. There will also be spectroscopic follow-up analyses of the new dSph candidates, confirming (or rejecting) that they are indeed dSphs and obtaining properly measured J factors. A subset of all new satellites will probably be globular clusters.

But more dSphs will increase the problem with overlapping ROIs in the combined Fermi-LAT analysis. To avoid biases arising from counting the same data multiple times, either a subset of available dSphs will have to be chosen (as was made for Paper II), or optimized ROIs containing

several dSphs, similar to what has been done for galaxy clusters using the *Composite2* code [44], will have to be used.

A better understanding of TS distribution could reduce overcoverage and give more constraining limits. New catalogs reducing the amount of unresolved sources will also bring the TS distribution closer to the expected distribution following Chernoff's theorem. Multi-wavelength studies could also aid in identifying and including unresolved sources [87].

By applying a fully frequentist approach when determining the DM content in dSphs and calculating the J factors, the exact likelihood can be used in the Fermi-LAT analysis properly including the statistical uncertainties from the J-factor calculations. This would be a major leap forward in how to properly include the uncertainties. Better stellar data from future measurements will further reduce the uncertainties. The GAIA satellite [175, 8] was launched in 2013 and aims to create a 3-dimensional map of our Galaxy. Its instruments will perform high resolution astrometry, photometry and spectroscopy for about one billion Milky Way stars. The data from GAIA could reduce the statistical uncertainty in the J-factor determination by providing better measurements, but will probably not reach the required magnitude [9].

The possibility to tie the background parameters over the ROIs could be revisited. It is possible that, with the updated data, catalogs, models, and analysis, this will improve the limits without worsening the fits. This might be a way to avoid overlapping ROIs by having smaller ROIs for each dSph and fitting the backgrounds jointly. In this way there is enough data to get good fits even though the individual ROIs are too small to properly fit the backgrounds. This, of course, is just an idea and needs to be investigated further.

Including the background uncertainties in the likelihood, either by fitting them individually, fitting them jointly, or by using a method similar to the inclusion of the J-factor uncertainties, would further improve the accuracy of the limits.

There are several new, and upcoming, gamma-ray experiments that will present an increased sensitivity to DM searches. The upgrade of the H.E.S.S. observatory [52] with the H.E.S.S. II telescope, has been operational since July 2012, and reaches lower energies with higher resolution [10]. The DAMPE (DArk Matter Particle Explorer [11]) satellite mission is planned to be launched in 2015-2016, and the CALET (CALorimetric Electron Telescope [12]) experiment is planned to be placed on the International Space Station in 2015. Both DAMPE and CALET are dedicated

to high energy gamma rays, electrons, and cosmic rays, and have DM searches as a main science objective. Future observatories, like e.g. CTA (that should be operational by 2018) [31] and Gamma-400 [113], will also probe further into the DM parameter space. CTA observations of the Galactic center could probe the velocity-averaged thermal WIMP cross-section at masses between 300-2000 GeV for the $b\bar{b}$ annihilation channel with 100 hours of observation [106], or, with 500 hours of observations and for the $\tau^+\tau^-$ annihilation channel, maybe even between 50-10000 GeV [216]. H.E.S.S. II, CTA, and Gamma-400 could e.g. be able to detect a gamma-ray line at ~ 130 GeV with a significance above 5σ, or rule out the existence of such a feature [79].

Collider searches and direct detection experiments are also evolving. As mentioned in Section 1.4, the new phase of the LHC might lead to discoveries of new physics [150]. There are ongoing upgrades to direct detection experiments, e.g. XENON1t [13], and planned experiments, e.g. DARWIN [14].

These upgraded and new experiments will further improve the prospects of finally detecting and explaining the mysterious dark matter.

References

[1] http://cdms.berkeley.edu/.

[2] http://people.roma2.infn.it/ dama/web/home.html.

[3] http://www.cresst.de/.

[4] http://xenon.astro.columbia.edu/xenon100.html.

[5] http://fermi.gsfc.nasa.gov/ssc/data/analysis/software/.

[6] http://fermi.gsfc.nasa.gov/ssc/data/access/lat/ BackgroundModels.html.

[7] http://www.darkenergysurvey.org/index.shtml.

[8] http://sci.esa.int/gaia/.

[9] G. Martinez, private communication.

[10] http://www.mpi-hd.mpg.de/hfm/HESS/pages/press/2012/ HESS_II_first_light/.

[11] http://dpnc.unige.ch/dampe/index.html.

[12] http://calet.phys.lsu.edu/index.php.

[13] http://www.xenon1t.org/.

[14] http://darwin.physik.uzh.ch/.

[15] **NED image from STScI Digitized Sky Survey**. http://nedwww.ipac.caltech.edu. The NASA/IPAC Extragalactic Database (NED) is operated by the Jet Propulsion Laboratory, California Institute of Technology, under contract with the National Aeronautics and Space Administration.

[16] G. Aad et al. **The ATLAS Experiment at the CERN Large Hadron Collider**. *JINST*, **3**:S08003, 2008.

[17] G. Aad et al. **Observation of a new particle in the search for the Standard Model Higgs boson with the ATLAS detector at the LHC**. *Phys.Lett.*, **B716**:1–29, 2012.

[18] G. Aad et al. **Search for dark matter in events with a Z boson and missing transverse momentum in pp collisions at $\sqrt{s}$=8 TeV with the ATLAS detector**. *Phys. Rev.*, **D90**(1):012004, 2014.

[19] G. Aad et al. **Search for dark matter in events with heavy quarks and missing transverse momentum in *pp* collisions with the ATLAS detector**. *Eur. Phys. J.*, **C75**(2):92, 2015.

[20] G. Aad et al. **Search for Dark Matter in Events with Missing Transverse Momentum and a Higgs Boson Decaying to Two Photons in *pp* Collisions at $\sqrt{s} = 8$ TeV with the ATLAS Detector**. 2015. Submitted to Phys.Rev.Lett.

[21] M. G. Aartsen et al. **Search for dark matter annihilations in the Sun with the 79-string IceCube detector**. *ArXiv e-prints*, December 2012.

[22] M.G. Aartsen et al. **IceCube Search for Dark Matter Annihilation in nearby Galaxies and Galaxy Clusters**. *Phys.Rev.*, **D88**:122001, 2013.

[23] M.G. Aartsen et al. **Multipole analysis of IceCube data to search for dark matter accumulated in the Galactic halo**. *Eur.Phys.J.*, **C75**(1):20, 2015.

[24] R. Abbasi et al. **Search for Neutrinos from Annihilating Dark Matter in the Direction of the Galactic Center with the 40-String IceCube Neutrino Observatory**. 2012.

[25] A. A. Abdo et al. **Measurement of the Cosmic Ray e+ plus e- spectrum from 20 GeV to 1 TeV with the Fermi Large Area Telescope**. *Phys.Rev.Lett.*, **102**:181101, 2009.

[26] A. A. Abdo et al. **Fermi Large Area Telescope First Source Catalog**. *Astrophys. J. Suppl.*, **188**:405–436, 2010.

[27] A. A. Abdo et al. **Observations of Milky Way Dwarf Spheroidal galaxies with the Fermi-LAT detector and constraints on Dark Matter models**. *Astrophys. J.*, **712**:147–158, 2010.

[28] D. Abercrombie et al. **Dark Matter Benchmark Models for Early LHC Run-2 Searches: Report of the ATLAS/CMS Dark Matter Forum**. 2015.

[29] A. Abramowski et al. **Search for dark matter annihilation signatures in H.E.S.S. observations of Dwarf Spheroidal Galaxies**. *Phys.Rev.*, **D90**:112012, 2014.

[30] L. Accardo et al. **High Statistics Measurement of the Positron Fraction in Primary Cosmic Rays of 0.5-500 GeV with the Alpha Magnetic Spectrometer on the International Space Station**. *Phys. Rev. Lett.*, **113**:121101, Sep 2014.

[31] B. S. Acharya et al. **Introducing the CTA concept**. *Astroparticle Physics*, **43**:3–18, March 2013.

[32] A. Achterberg et al. **First year performance of the IceCube neutrino telescope**. *Astroparticle Physics*, **26**:155–173, October 2006.

[33] M. Ackermann and for the Fermi-LAT Collaboration. **Pass 7: An upgrade to the Fermi-LAT analysis**. In *Poster Instr S2.N1*, May 2011. 3:d Fermi Symposium, Rome.

[34] M. Ackermann et al. **Constraints on Dark Matter Annihilation in Clusters of Galaxies with the Fermi Large Area Telescope**. *JCAP*, **1005**:025, 2010.

[35] M. Ackermann et al. **Constraining Dark Matter Models from a Combined Analysis of Milky Way Satellites with the Fermi Large Area Telescope**. *Phys. Rev. Lett.*, **107**:241302, Dec 2011.

[36] M. Ackermann et al. **Constraints on the Galactic Halo Dark Matter from Fermi-LAT Diffuse Measurements**. *ApJ*, **761**:91, December 2012.

[37] M. Ackermann et al. **Fermi LAT search for dark matter in gamma-ray lines and the inclusive photon spectrum**. *Phys. Rev. D*, **86**(2):022002, July 2012.

[38] M. Ackermann et al. **Measurement of Separate Cosmic-Ray Electron and Positron Spectra with the Fermi Large Area Telescope**. *Phys. Rev. Lett.*, **108**:011103, Jan 2012.

[39] M. Ackermann et al. **Search for Dark Matter Satellites Using Fermi-LAT**. *ApJ*, **747**:121, March 2012.

[40] M. Ackermann et al. **The Fermi Large Area Telescope on Orbit: Event Classification, Instrument Response Functions, and Calibration**. *ApJS*, **203**:4, November 2012.

[41] M. Ackermann et al. **The Imprint of the Extragalactic Background Light in the Gamma-Ray Spectra of Blazars**. *Science*, **338**:1190–, November 2012.

[42] M. Ackermann et al. **Search for gamma-ray spectral lines with the Fermi large area telescope and dark matter implications**. *Phys.Rev.*, **D88**:082002, 2013.

[43] M. Ackermann et al. **Dark matter constraints from observations of 25 Milky Way satellite galaxies with the Fermi Large Area Telescope**. *Phys.Rev.*, **D89**:042001, 2014.

[44] M. Ackermann et al. **Search for cosmic-ray induced gamma-ray emission in Galaxy Clusters**. *Astrophys.J.*, **787**:18, 2014.

[45] M. Ackermann et al. **Searching for Dark Matter Annihilation from Milky Way Dwarf Spheroidal Galaxies with Six Years of Fermi-LATData**. *Phys. Rev. Lett.*, 2015.

[46] M. Actis et al. **Design concepts for the Cherenkov Telescope Array CTA: an advanced facility for ground-based high-energy gamma-ray astronomy**. *Experimental Astronomy*, **32**:193–316, December 2011.

[47] P.A.R. Ade et al. **Planck 2013 results. XVI. Cosmological parameters**. *Astron.Astrophys.*, **571**:A16, 2014.

[48] P.A.R. Ade et al. **Planck 2015 results. XIII. Cosmological parameters**. 2015. Submitted to Astron.Astrophys.

[49] O. Adriani et al. **A new measurement of the antiproton-to-proton flux ratio up to 100 GeV in the cosmic radiation**. *Phys.Rev.Lett.*, **102**:051101, 2009.

[50] O. Adriani et al. **An anomalous positron abundance in cosmic rays with energies 1.5-100 GeV**. *Nature*, **458**:607–609, 2009.

[51] M. Ageron et al. **ANTARES: The first undersea neutrino telescope**. *Nuclear Instruments and Methods in Physics Research A*, **656**:11–38, November 2011.

[52] F. Aharonian et al. **Observations of the Crab Nebula with H.E.S.S**. *Astron.Astrophys.*, **457**:899–915, 2006.

[53] M. Ajello et al. **Limits on large extra dimensions based on observations of neutron stars with the Fermi-LAT**. *JCAP*, **2**:12, February 2012.

[54] C. Alcock et al. **The MACHO project: Microlensing results from 5.7 years of LMC observations**. *Astrophys.J.*, **542**:281–307, 2000.

[55] J. Aleksić et al. **Performance of the MAGIC stereo system obtained with Crab Nebula data**. *Astroparticle Physics*, **35**:435–448, February 2012.

[56] N. C. Amorisco et al. **The core size of the Fornax dwarf spheroidal**. *MNRAS*, **429**:L89–L93, February 2013.

[57] B. Anderson et al. **Using Likelihood for Combined Data Set Analysis**. 2015.

[58] G. Angloher et al. **Results from 730 kg days of the CRESST-II Dark Matter Search**. 2011.

[59] G. Angloher et al. **Results on low mass WIMPs using an upgraded CRESST-II detector**. *European Physical Journal C*, **74**:3184, December 2014.

[60] M. Arik et al. **Search for Solar Axions by the CERN Axion Solar Telescope with ^{3}He Buffer Gas: Closing the Hot Dark Matter Gap**. *Phys. Rev. Lett.*, **112**:091302, Mar 2014.

[61] W. Atwood et al. **Pass 8: Toward the Full Realization of the Fermi-LAT Scientific Potential**. *2012 Fermi Symposium proceedings - eConf C121028*, 2013.

[62] W. B. Atwood et al. **The Large Area Telescope on the Fermi Gamma-ray Space Telescope Mission**. *Astrophys. J.*, **697**:1071–1102, 2009.

[63] E. A. Baltz et al. **Pre-launch estimates for GLAST sensitivity to Dark Matter annihilation signals**. *JCAP*, **0807**:013, 2008.

[64] G. Battaglia et al. **The DART imaging and CaT survey of the Fornax Dwarf Spheroidal Galaxy**. *Astron.Astrophys.*, **459**:423, 2006.

[65] G. Battaglia et al. **Study of the Sextans dwarf spheroidal galaxy from the DART Caii triplet survey**. *Mon.Not.Roy.Astron.Soc.*, **411**(2):1013–1034, 2011.

[66] G. Battaglia et al. **The Extensive Age Gradient of the Carina Dwarf Galaxy**. *The Astrophysical Journal Letters*, **761**(2):L31, 2012.

[67] K. Bechtol et al. **Eight New Milky Way Companions Discovered in First-Year Dark Energy Survey Data**. *ArXiv e-prints*, March 2015.

[68] V. Belokurov. http://www.ast.cam.ac.uk/˜vasily/.

[69] V. Belokurov et al. **A Faint New Milky Way Satellite in Bootes**. *Astrophys.J.*, **647**:L111–L114, 2006.

[70] V. Belokurov et al. **An Orphan in the Field of Streams**. *Astrophys.J.*, **658**:337–344, 2007.

[71] V. Belokurov et al. **Cats and Dogs, Hair and A Hero: A Quintet of New Milky Way Companions**. *Astrophys.J.*, **654**:897–906, 2007.

[72] V. Belokurov et al. **Leo V: A Companion of a Companion of the Milky Way Galaxy**. *Astrophys.J.*, **686**:L83–L86, 2008.

[73] V. Belokurov et al. **Segue 2: A Prototype of the Population of Satellites of Satellites**. *Mon.Not.Roy.Astron.Soc.*, **397**:1748–1755, 2009.

[74] V. Belokurov et al. **Big fish, small fish: Two New Ultra-Faint Satellites of the Milky Way**. *Astrophys.J.*, **712**:L103, 2010.

[75] B. Berenji and J. M. Siegal-Gaskins. **Constraints on Axions and Axion-Like Particles from Fermi-LAT Observations of Neutron Stars**. In *AAS/High Energy Astrophysics Division*, **14** of *AAS/High Energy Astrophysics Division*, page 107.06, August 2014.

[76] L. Bergström. **Nonbaryonic dark matter: Observational evidence and detection methods**. *Rept.Prog.Phys.*, **63**:793, 2000.

[77] L. Bergström. **Dark matter: past, present and future**. Workshop on Off-the-Beaten-Track Dark Matter and Astrophysical Probes of Fundamental Physics, Apr 2015.

[78] L. Bergström et al. **Dark matter interpretation of recent electron and positron data**. *Phys.Rev.Lett.*, **103**:031103, 2009.

[79] L. Bergström et al. **Investigating Gamma-Ray Lines from Dark Matter with Future Observatories**. *JCAP*, **1211**:025, 2012.

[80] R. Bernabei et al. **New results from DAMA/LIBRA**. *Eur.Phys.J.*, **C67**:39–49, 2010.

[81] M. Boylan-Kolchin et al. **The Space Motion of Leo I: The Mass of the Milky Way's Dark Matter Halo**. *Astrophys.J.*, **768**:140, May 2013.

[82] J. Bregeon and others. **Fermi-LAT data reprocessed with updated calibration constants**. *2012 Fermi Symposium proceedings - eConf C121028*, 2013.

[83] M. R. Buckley et al. **Search for Gamma-ray Emission from Dark Matter Annihilation in the Large Magellanic Cloud with the Fermi Large Area Telescope**. *Phys.Rev.D*, 2015.

[84] A. Burkert. **The Structure of dark matter halos in dwarf galaxies**. *IAU Symp.*, **171**:175, 1996.

[85] R. D. Cannon et al. **A new Sculptor-type dwarf elliptical galaxy in Carina**. *Mon.Not.Roy.Astron.Soc.*, **180**:81P–82P, September 1977.

[86] J. L. Carlin et al. **Kinematics and Metallicities in the Boötes III Stellar Overdensity: A Disrupted Dwarf Galaxy?** *Astrophys. J. Lett.*, **702**:L9–L13, September 2009.

[87] E. Carlson et al. **Improving the sensitivity of gamma-ray telescopes to dark matter annihilation in dwarf spheroidal galaxies**. *Phys. Rev. D*, **91**(6):061302, March 2015.

[88] B. J. Carr et al. **New cosmological constraints on primordial black holes**. *Phys. Rev. D*, **81**(10):104019, May 2010.

[89] A. Charbonnier et al. **Dark matter profiles and annihilation in dwarf spheroidal galaxies: prospectives for present and future gamma-ray observatories - I. The classical dSphs**. 2011.

[90] A. Charbonnier et al. **CLUMPY: A code for γ-ray signals from dark matter structures**. *Computer Physics Communications*, **183**:656–668, March 2012.

[91] S. Chatrchyan et al. **The CMS experiment at the CERN LHC**. *JINST*, **3**:S08004, 2008.

[92] S. Chatrchyan et al. **Observation of a new boson at a mass of 125 GeV with the CMS experiment at the LHC**. *Phys.Lett.*, **B716**:30–61, 2012.

[93] H. Chernoff. **On the Distribution of the Likelihood Ratio**. *Ann. Math. Statist.*, **25**(3):573–578, 09 1954.

[94] I. Cholis et al. **Challenges in Explaining the Galactic Center Gamma-Ray Excess with Millisecond Pulsars**. *ArXiv e-prints*, July 2014.

[95] S. Ciprini and on behalf of the Fermi Large Area Telescope Collaboration. **Fermi LAT confirmation of a strong GeV flare from 4C 21.35 (PKS 1222+21)**. ATel 2349, 12 2009.

[96] D. Clowe et al. **A direct empirical proof of the existence of dark matter**. *Astrophys.J.*, **648**:L109–L113, 2006.

[97] M. L. M. Collins et al. **The masses of Local Group dwarf spheroidal galaxies: The death of the universal mass profile**. *Astrophys. J.*, **783**:7, 2014.

[98] J. Conrad. **Statistical Issues in Astrophysical Searches for Particle Dark Matter**. *Astropart.Phys.*, **62**:165–177, 2014.

[99] J. Conrad et al. **WIMP searches with gamma rays in the Fermi era: challenges, methods and results**. *Invited review for Journal of Experimental and Theoretical Physics*, 2015.

[100] E. Corbelli and P. Salucci. **The extended rotation curve and the dark matter halo of M33**. *MNRAS*, **311**:441–447, January 2000.

[101] M. Dall'Ora et al. **Variable stars in the newly discovered Milky Way satellite in Bootes**. *Astrophys. J.*, **653**:L109–L112, 2006.

[102] F. de Palma, others, and for the Fermi LAT collaboration. **A Method for Exploring Systematics Due to Galactic Interstellar Emission Modeling: Application to the Fermi LAT SNR Catalog**. *ArXiv e-prints*, April 2013.

[103] H. Dickinson and J. Conrad. **Handling systematic uncertainties and combined source analyses for Atmospheric Cherenkov Telescopes**. *Astroparticle Physics*, **41**:17–30, January 2013.

[104] J. Diemand et al. **Clumps and streams in the local dark matter distribution**. *Nature*, **454**:735–738, August 2008.

[105] D. Donnato and on behalf of the Fermi Large Area Telescope Collaboration. **Fermi LAT observed another strong GeV flare from 4C 21.35 (PKS 1222+21)**. ATel 2584, 4 2010.

[106] M. Doro and CTA Consortium. **Dark matter and fundamental physics with the Cherenkov Telescope Array**. *Astroparticle Physics*, **43**:189–214, March 2013.

[107] A. Drlica-Wagner et al. **Searching for Dark Matter Annihilation in the Smith High-Velocity Cloud**. *Astrophys.J.*, **790**:24, 2014.

[108] A. Drlica-Wagner et al. **Eight Ultra-faint Galaxy Candidates Discovered in Year Two of the Dark Energy Survey**. *ArXiv e-prints*, August 2015. submitted to ApJ.

[109] A. Drlica-Wagner et al. **Search for Gamma-Ray Emission from DES Dwarf Spheroidal Galaxy Candidates with Fermi-LAT Data**. 2015. Accepted for publication in ApJ Letters.

[110] J. Einasto. **Kinematics and dynamics of stellar systems**. Trudy Inst. Astrofiz. Alma-Ata 51, 87., 1965.

[111] G. J. Feldman and R. D. Cousins. **Unified approach to the classical statistical analysis of small signals**. *Phys. Rev. D*, **57**:3873–3889, April 1998.

[112] P. M. Frinchaboy et al. **A 2MASS All-Sky View of the Sagittarius Dwarf Galaxy: VII. Kinematics of the Main Body of the Sagittarius dSph**. *Astrophys.J.*, **756**:74, 2012.

[113] A.M. Galper et al. **Status of the GAMMA-400 Project**. 2012.

[114] M. Geha et al. **The Least Luminous Galaxy: Spectroscopy of the Milky Way Satellite Segue 1**. *Astrophys.J.*, **692**:1464–1475, 2009.

[115] A. Geringer-Sameth et al. **A Comprehensive Search for Dark Matter Annihilation in Dwarf Galaxies**. 2014.

[116] A. Geringer-Sameth et al. **Dwarf galaxy annihilation and decay emission profiles for dark matter experiments**. *Astrophys.J.*, **801**(2):74, 2015.

[117] A. Geringer-Sameth et al. **Evidence for Gamma-ray Emission from the Newly Discovered Dwarf Galaxy Reticulum 2**. 2015.

[118] A. Geringer-Sameth and S. M. Koushiappas. **Exclusion of canonical WIMPs by the joint analysis of Milky Way dwarfs with Fermi**. *Phys.Rev.Lett.*, **107**:241303, 2011.

[119] A. Geringer-Sameth and S. M. Koushiappas. **Dark matter line search using a joint analysis of dwarf galaxies with the Fermi Gamma-ray Space Telescope**. *Phys.Rev.*, **D86**:021302, 2012.

[120] T. Goerdt et al. **Does the Fornax dwarf spheroidal have a central cusp or core?** *Mon.Not.Roy.Astron.Soc.*, **368**(3):1073–1077, 2006.

[121] P. Gondolo et al. **DarkSUSY: computing supersymmetric dark matter properties numerically**. *Journal of Cosmology and Astroparticle Physics*, **2004**(07):008, 2004.

[122] C. J. Grillmair. **Four New Stellar Debris Streams in the Galactic Halo**. *Astrophys.J.*, **693**:1118–1127, 2009.

[123] J. R. Hargis et al. **Too Many, Too Few, or Just Right? The Predicted Number and Distribution of Milky Way Dwarf Galaxies**. *ApJ*, **795**:L13, November 2014.

[124] R. G. Harrington and A. G. Wilson. **Two New Stellar Systems in Leo**. *PASP*, **62**:118–120, June 1950.

[125] C. He et al. **Prospects for detecting gamma rays from annihilating dark matter in dwarf galaxies in the era of the Dark Energy Survey and Large Synoptic Survey Telescope**. *Phys.Rev.*, **D91**(6):063515, 2015.

[126] L. Hernquist. **An analytical model for spherical galaxies and bulges**. *ApJ*, **356**:359–364, June 1990.

[127] G. Hinshaw et al. **Nine-year Wilkinson Microwave Anisotropy Probe (WMAP) Observations: Cosmological Parameter Results**. *ApJS*, **208**:19, October 2013.

[128] D. Hooper and P. D. Serpico. **Detecting Axionlike Particles with Gamma Ray Telescopes**. *Physical Review Letters*, **99**(23):231102, December 2007.

[129] X. Huang et al. **Probing Dark Matter Decay and Annihilation with Fermi LAT Observations of Nearby Galaxy Clusters**. *JCAP*, **1201**:042, 2012.

[130] G. Iafrate, others, and on behalf of the Fermi-LAT Collaboration. **Fermi LAT detection of a very intense GeV flare from 4C +21.35 (PKS 1222+21)**. ATel 2687, 6 2010.

[131] R. A. Ibata et al. **A dwarf satellite galaxy in Sagittarius**. *Nature*, **370**(6486):194–196, 07 1994.

[132] F. Iocco et al. **Evidence for dark matter in the inner Milky Way**. *Nature Physics*, **11**:245–248, March 2015.

[133] M. J. Irwin et al. **A new satellite galaxy of the Milky Way in the constellation of Sextans**. *Mon.Not.Roy.Astron.Soc.*, **244**:16P–19P, May 1990.

[134] C.B. Jackson et al. **Higgs in Space!** *JCAP*, **1004**:004, 2010.

[135] F. James. *MINUIT Reference Manual*. CERN Program Library Writeup D506.

[136] F. James. *Statistical Methods in Experimental Physics*. World Scientific Publishing, 2 edition, 2006.

[137] T. E. Jeltema and S. Profumo. **Fitting the gamma-ray spectrum from dark matter with DMFIT: GLAST and the galactic center region**. *JCAP*, **11**:3, November 2008.

[138] G. Jungman et al. **Supersymmetric Dark Matter**. *Phys. Rep.*, **267**:195, 1996.

[139] G. Kauffmann et al. **The Formation and Evolution of Galaxies Within Merging Dark Matter Haloes**. *Mon.Not.Roy.Astron.Soc.*, **264**:201, September 1993.

[140] V. Khachatryan et al. **Search for dark matter, extra dimensions, and unparticles in monojet events in protonproton collisions at $\sqrt{s} = 8$ TeV**. *Eur. Phys. J.*, **C75**(5):235, 2015.

[141] V. Khachatryan et al. **Search for the production of dark matter in association with top-quark pairs in the single-lepton final state in proton-proton collisions at $\sqrt{s} = 8$ TeV**. *JHEP*, **06**:121, 2015.

[142] I. King. **The structure of star clusters. I. an empirical density law**. *Astron.J.*, **67**:471, October 1962.

[143] E. N. Kirby et al. **Segue 2: The Least Massive Galaxy**. *Astrophys.J.*, **770**:16, 2013.

[144] J. T. Kleyna et al. **A dynamical fossil in the ursa minor dwarf spheroidal galaxy**. *Astrophys.J.*, **588**:L21–L24, 2003.

[145] A. Koch et al. **Stellar kinematics in the remote Leo II dwarf spheroidal galaxy – Another brick in the wall**. *Astronom. J.*, **134**:566–578, 2007.

[146] A. Koch et al. **A Spectroscopic Confirmation of the Bootes II Dwarf Spheroidal**. *The Astrophysical Journal*, **690**(1):453, 2009.

[147] S. E. Koposov et al. **Beasts of the Southern Wild. Discovery of a large number of Ultra Faint satellites in the vicinity of the Magellanic Clouds**. *ArXiv e-prints*, March 2015.

[148] M. Kuhlen et al. **The Dark Matter Annihilation Signal from Galactic Substructure: Predictions for GLAST**. *ApJ*, **686**:262–278, October 2008.

[149] B. P. M. Laevens et al. **A New Faint Milky Way Satellite Discovered in the Pan-STARRS1 3 pi Survey**. 2015.

[150] Katharine Leney. **ATLAS and CMS Exotics Searches: Run 1 Results and Run 2 Prospects**. Technical Report ATL-PHYS-PROC-2015-027, CERN, Geneva, May 2015.

[151] K. Lundmark. **Über die bestimmung der Entfernungen Dimensionen, Massen und Dichtigkeiten für die Nächstgelegenen Anagalaktischen Sternsysteme**. *Meddelanden fran Lunds Astronomiska Observatorium*, **125**:1–10, 1930.

[152] D. Malyshev et al. **Pulsars versus Dark Matter Interpretation of ATIC/PAMELA**. *Phys.Rev.*, **D80**:063005, 2009.

[153] D. Malyshev, others, and on behalf of the Fermi-LAT Collaboration. **Fermi LAT limit on evaporation of primordial black holes**. 5:th Fermi Symposium, Poster 3.07, Oct 2014.

[154] M. Markevitch. **Chandra observation of the most interesting cluster in the universe**. *ESA Spec.Publ.*, **604**:723, 2006.

[155] N. F. Martin et al. **Hydra II: a faint and compact Milky Way dwarf galaxy found in the Survey of the Magellanic Stellar History**. *ArXiv e-prints*, March 2015.

[156] N.F. Martin et al. **A Dwarf galaxy remnant in Canis Major: The Fossil of an in - plane accretion onto the Milky Way**. *Mon.Not.Roy.Astron.Soc.*, **348**:12, 2004.

[157] G. D. Martinez. **A robust determination of Milky Way satellite properties using hierarchical mass modelling**. *Mon.Not.Roy.Astron.Soc.*, **451**(3):2524–2535, 2015.

[158] G. D. Martinez et al. **Indirect Dark Matter detection from Dwarf satellites: joint expectations from astrophysics and supersymmetry**. *JCAP*, **6**:14, June 2009.

[159] G. D. Martinez et al. **A Complete Spectroscopic Survey of the Milky Way satellite Segue 1: Dark matter content, stellar membership and binary properties from a Bayesian analysis**. *Astrophys.J.*, **738**:55, 2011.

[160] M. Mateo et al. **The Velocity Dispersion Profile of the Remote Dwarf Spheroidal Galaxy Leo. 1. A Tidal Hit and Run?** *Astrophys. J.*, **675**:201, 2008.

[161] M. N. Mazziotta et al. **A model-independent analysis of the Fermi Large Area Telescope gamma-ray data from the Milky Way dwarf galaxies and halo to constrain dark matter scenarios**. *Astroparticle Physics*, **37**:26–39, September 2012.

[162] A. W. McConnachie. **The Observed Properties of Dwarf Galaxies in and around the Local Group**. *Astron.J.*, **144**:4, July 2012.

[163] M. Milgrom. **A modification of the Newtonian dynamics as a possible alternative to the hidden mass hypothesis**. *ApJ*, **270**:365–370, July 1983.

[164] A.A. Moiseev et al. **Observation and simulations of the backsplash effects in high-energy gamma-ray telescopes containing a massive calorimeter**. *Astropart.Phys.*, **22**:275–283, 2004.

[165] R. R. Muñoz et al. **Exploring halo substructure with giant stars: the velocity dispersion profiles of the Ursa Minor and Draco dwarf spheroidals at large angular separations**. *Astrophys. J.*, **631**:L137–L142, 2005.

[166] R. R. Munoz et al. **Turning the Tides on the Ultra-Faint Dwarf Spheroidal Galaxies: Coma Berenices and Ursa Major II**. *Astron.J.*, **140**:138, 2010.

[167] J. F. Navarro et al. **A Universal Density Profile from Hierarchical Clustering**. *Astrophys. J.*, **490**:493–508, 1997.

[168] J. Neyman. **Outline of a Theory of Statistical Estimation Based on the Classical Theory of Probability**. *Phil.Trans.Roy.Soc.Lond. A*, **236**:333–380, August 1937.

[169] M. Niederste-Ostholt et al. **The origin of Segue 1**. *Mon.Not.Roy.Astron.Soc.*, **398**(4):1771–1781, 2009.

[170] P. L. Nolan et al. **Fermi Large Area Telescope Second Source Catalog**. *ApJS*, **199**:31, April 2012.

[171] A. Drlica-Wagner on behalf of the Fermi-LAT Collaboration. **A Modified Likelihood Approach to Search for Faint Sources**. 5:th Fermi Symposium, Parallel 10B, Oct 2014.

[172] M. Mayer on behalf of the Fermi-LAT Collaboration. **Search for axion-like particle signatures in the gamma-ray spectrum of NGC 1275**. The 11th Patras Workshop on Axions, June 2015.

[173] P. Bruel on behalf of the Fermi-LAT Collaboration. **Performance of Pass 8 Event Analysis of the Fermi Large Area Telescope**. 5:th Fermi Symposium, Parallel 10B, Oct 2014.

[174] B. Paczynski. **Gravitational microlensing by the galactic halo**. *ApJ*, **304**:1–5, May 1986.

[175] M. A. C. Perryman et al. **GAIA: Composition, formation and evolution of the Galaxy**. *A&A*, **369**:339–363, April 2001.

[176] J. Petrović et al. **Millisecond pulsars and the Galactic Center gamma-ray excess: the importance of luminosity function and secondary emission**. *JCAP*, **2**:23, February 2015.

[177] A. Pinzke et al. **Prospects of detecting gamma-ray emission from galaxy clusters: cosmic rays and dark matter annihilations**. *Phys.Rev.*, **D84**:123509, 2011.

[178] C. Pittori and the AGILE Team. **The Gamma-Ray Imaging Detector AGILE: Scientific Goals and Instrument Performance**. *Chinese Journal of Astronomy and Astrophysics*, **3**(S1):517, 2003.

[179] H. C. Plummer. **On the Problem of Distribution in Globular Star Clusters: (Plate 8.)**. *Mon.Not.Roy.Astron.Soc.*, **71**(5):460–470, 1911.

[180] M. Regis et al. **Local Group dSph radio survey with ATCA (III): Constraints on Particle Dark Matter**. *JCAP*, **1410**(10):016, 2014.

[181] T. H. Reiprich and H. Böhringer. **The Mass Function of an X-Ray Flux-limited Sample of Galaxy Clusters**. *ApJ*, **567**:716–740, March 2002.

[182] W. A. Rolke et al. **Limits and confidence intervals in the presence of nuisance parameters**. *Nucl.Instrum.Meth. A*, **551**:493–503, October 2005.

[183] V. C. Rubin et al. **Rotational properties of 21 SC galaxies with a large range of luminosities and radii, from NGC 4605 /R = 4kpc/ to UGC 2885 /R = 122 kpc/**. *ApJ*, **238**:471–487, June 1980.

[184] T. Sakamoto and T. Hasegawa. **Discovery of a Faint Old Stellar System at 150 kpc**. *Astrophys.J.Lett.*, **653**:L29–L32, December 2006.

[185] M. A. Sánchez-Conde et al. **Hints of the existence of axionlike particles from the gamma-ray spectra of cosmological sources**. *Phys. Rev. D*, **79**:123511, Jun 2009.

[186] H. Shapley. **A Stellar System of a New Type**. *Harvard College Observatory Bulletin*, **908**:1–11, March 1938.

[187] H. Shapley. **Two Stellar Systems of a New Kind**. *Nature*, **142**:715–716, October 1938.

[188] J. D. Simon et al. **A Complete Spectroscopic Survey of the Milky Way Satellite Segue 1: The Darkest Galaxy**. *Astrophys. J.*, **733**:46, 2011.

[189] J. D. Simon and M. Geha. **The Kinematics of the Ultra-Faint Milky Way Satellites: Solving the Missing Satellite Problem**. *Astrophys. J.*, **670**:313–331, 2007.

[190] T. Sjöstrand et al. **A Brief Introduction to PYTHIA 8.1**. *Comput.Phys.Commun.*, **178**:852–867, 2008.

[191] S. Smith. **The Mass of the Virgo Cluster**. *ApJ*, **83**:23, January 1936.

[192] V. Springel et al. **The Aquarius Project: the subhaloes of galactic haloes**. *MNRAS*, **391**:1685–1711, December 2008.

[193] I. Steer. **New Facts From the First Galaxy Distance Estimates**. *JRASC*, **105**:18, February 2011.

[194] G. Steigman et al. **Precise relic WIMP abundance and its impact on searches for dark matter annihilation**. *Phys. Rev. D*, **86**(2):023506, July 2012.

[195] E. Striani et al. **AGILE detection of a gamma-ray flare from the blazar 4C+21.35 (PKS 1222+21)**. ATel 2686, 6 2010.

[196] L. E. Strigari. **Galactic searches for dark matter**. *Phys. Rep.*, **531**:1–88, October 2013.

[197] L. E. Strigari et al. **A common mass scale for satellite galaxies of the Milky Way**. *Nature*, **454**:1096–1097, 2008.

[198] L. E. Strigari et al. **Dynamical models for the Sculptor dwarf spheroidal in a Lambda CDM universe**. *ArXiv e-prints*, June 2014.

[199] A. W. Strong et al. **Cosmic-Ray Propagation and Interactions in the Galaxy**. *Annual Review of Nuclear and Particle Science*, **57**:285–327, November 2007.

[200] M. Sgall et al. **Draco, a flawless dwarf galaxy**. *Mon.Not.Roy.Astron.Soc.*, **375**(3):831–842, 2007.

[201] The Fermi-LAT Collaboration. **Fermi Large Area Telescope Third Source Catalog**. *accepted for publication in Astrophysical Journal Supplement Series*, January 2015.

[202] The Fermi LAT Collaboration. **Limits on Dark Matter Annihilation Signals from the Fermi LAT 4-year Measurement of the Isotropic Gamma-Ray Background**. *Submitted to JCAP*, January 2015.

[203] E. Tolstoy et al. **Two distinct ancient components in the Sculptor dwarf spheroidal galaxy: First results from DART**. *Astrophys.J.*, **617**:L119–L122, 2004.

[204] M. Walker. **Dark Matter in the Galactic Dwarf Spheroidal Satellites**. *Planets, Stars and Stellar Systems. Volume 5: Galactic Structure and Stellar Populations*, page 1039, 2013.

[205] M. G. Walker et al. **A Universal Mass Profile for Dwarf Spheroidal Galaxies?** *ApJ*, **704**:1274–1287, October 2009.

[206] M. G. Walker et al. **Stellar Velocities in the Carina, Fornax, Sculptor, and Sextans dSph Galaxies: Data From the Magellan/MMFS Survey**. *Astronom. J.*, **137**:3100–3108, February 2009.

[207] S. M. Walsh et al. **A Pair of Bootes: A New Milky Way Satellite**. *Astrophys. J. Lett.*, **662**(2):L83, 2007.

[208] C. Weniger. **A Tentative Gamma-Ray Line from Dark Matter Annihilation at the Fermi Large Area Telescope**. *JCAP*, **1208**:007, 2012.

[209] C. Weniger. **Gamma-ray lines in the Fermi-LAT data?** 2013. 2012 Fermi Symposium proceedings - eConf C121028.

[210] S.S. Wilks. **The Large-Sample Distribution of the Likelihood Ratio for Testing Composite Hypotheses**. *Annals Math.Statist.*, **9**(1):60–62, 1938.

[211] B. Willman et al. **A New Milky Way companion: Unusual globular cluster or extreme dwarf satellite?** *Astron.J.*, **129**:2692–2700, 2005.

[212] B. Willman et al. **A New Milky Way dwarf galaxy in Ursa Major**. *Astrophys.J.*, **626**:L85–L88, 2005.

[213] B. Willman et al. **Willman 1 - A Probable Dwarf Galaxy with an Irregular Kinematic Distribution**. *Astronom. J.*, **142**:128, October 2011.

[214] A. G. Wilson. **Sculptor-Type Systems in the Local Group of Galaxies**. *PASP*, **67**:27–29, February 1955.

[215] J. Wolf et al. **Accurate masses for dispersion-supported galaxies**. *MNRAS*, **406**:1220–1237, August 2010.

[216] M. Wood et al. **Prospects for Indirect Detection of Dark Matter with CTA**. *ArXiv e-prints*, May 2013.

[217] S. Zimmer, J. Conrad, for the Fermi-LAT Collaboration, and A. Pinzke. **A Combined Analysis of Clusters of Galaxies - Gamma Ray Emission from Cosmic Rays and Dark Matter**. 2011. 2011 Fermi Symposium - eConf Proceedings C110509.

[218] S. Zimmer et al. **Search for Dark-Matter-induced gamma rays from Galaxy Clusters**. In Prep., 2015.

[219] K. Zioutas et al. **A decommissioned {LHC} model magnet as an axion telescope**. *Nuclear Instruments and Methods in Physics Research Section A: Accelerators, Spectrometers, Detectors and Associated Equipment*, **425**(3):480 – 487, 1999.

[220] D. B. Zucker et al. **A Curious New Milky Way Satellite in Ursa Major**. *Astrophys.J.*, **650**:L41–L44, 2006.

[221] D. B. Zucker et al. **A New Milky Way Dwarf Satellite in Canes Venatici**. *Astrophys.J.*, **643**:L103–L106, 2006.

[222] F. Zwicky. **On the Masses of Nebulae and of Clusters of Nebulae**. *ApJ*, **86**:217, October 1937.

Part II

Appendix

Selection code for Galaxy Clusters

This Chapter describes the algorithm for selecting the galaxy clusters that will enter the combined analysis in the paper *Search for Dark-Matter-induced gamma rays from Galaxy Clusters* ([1] in preparation). I will describe the algorithm using an NFW profile without any boost from substructure.

We start with the 105 clusters compiled in the HIFLUCS catalog [2] (not including the Virgo cluster). First we remove clusters that we do not want in our sample for different reasons. In the example presented here, we removed cluster A0400 because it had large residuals consistent with a new source [3]. However, this source is now included in 3FGL and A0400 could probably be included in the sample. After this step, 104 clusters are left in the sample.

After removing A0400, we look at the spatial distribution of the clusters. First we remove the clusters that are close to the Galactic plane to avoid galactic foreground. We keep the clusters that are further away than 20 degrees from the Galactic plane. After this step, 93 clusters are left in the sample.

After this, we remove clusters that lie within the Galactic bubbles [4]. We have chosen the somewhat crude approach to remove clusters within a box defined by $340 < l < 20$ degrees and $50 < b < 50$ degrees, where l and b are galactic longitude and latitude, respectively. After this step, 86 clusters are left in the sample.

We want to avoid the Virgo region and remove clusters that overlap with Virgo. We remove clusters that are closer than 2 degrees from Virgo by making sure that the distance, d, between the centers of the clusters is smaller than the sum of the virial radius of Virgo (defined as where the enclosed mean mass density exceeds the critical density by a factor

200), $R_{200,Virgo}$, the virial radius of the other cluster, $R_{200,cluster}$, and 2 degrees, i.e. $d < R_{200,Virgo} + R_{200,cluster} + 2^\circ$ After this step, 84 clusters are left in the sample.

We also want to avoid clusters that overlap wth each other, so the next step is to remove clusters where the angular separation between the clusters is less then 2 degrees, i.e. $d < R_{200,cluster1} + R_{200,cluster2} + 2^\circ$ After this step, 53 clusters are left in the sample.

At the last step we chose to only have one cluster in each ROI, and therefor have to ensure that we do not have overlapping ROIs. The ROIs have a radius of 8 degrees, so no cluster centers can be closer to each other than 16 degrees. If two ROIs overlap we keep the cluster with the highest J factor. In the case where 3 or more ROIs are overlapping, we find the combination of non-overlapping ROIs that gives the largest overall J factor. After this step, 32 clusters are left in the sample.

We carefully chose the order of the steps mentioned above to ensure that no cluster was erroneously removed. If, e.g. , the step where we avoid overlapping ROIs is made earlier, clusters with high J factors lying in e.g. the bubble region could veto lower J-factor clusters that would have been selected if the 'bubble cut' was made earlier. The only step that could have been placed differently is the 'overlap cut', where clusters within 2 degrees of each other are removed, that could have been placed earlier to avoid including a cluster that overlaps with a removed cluster. The clusters are overlaid on a 4-year Fermi-LAT counts map in Fig. 8.1, where rejected clusters are plotted in red and included clusters in green.

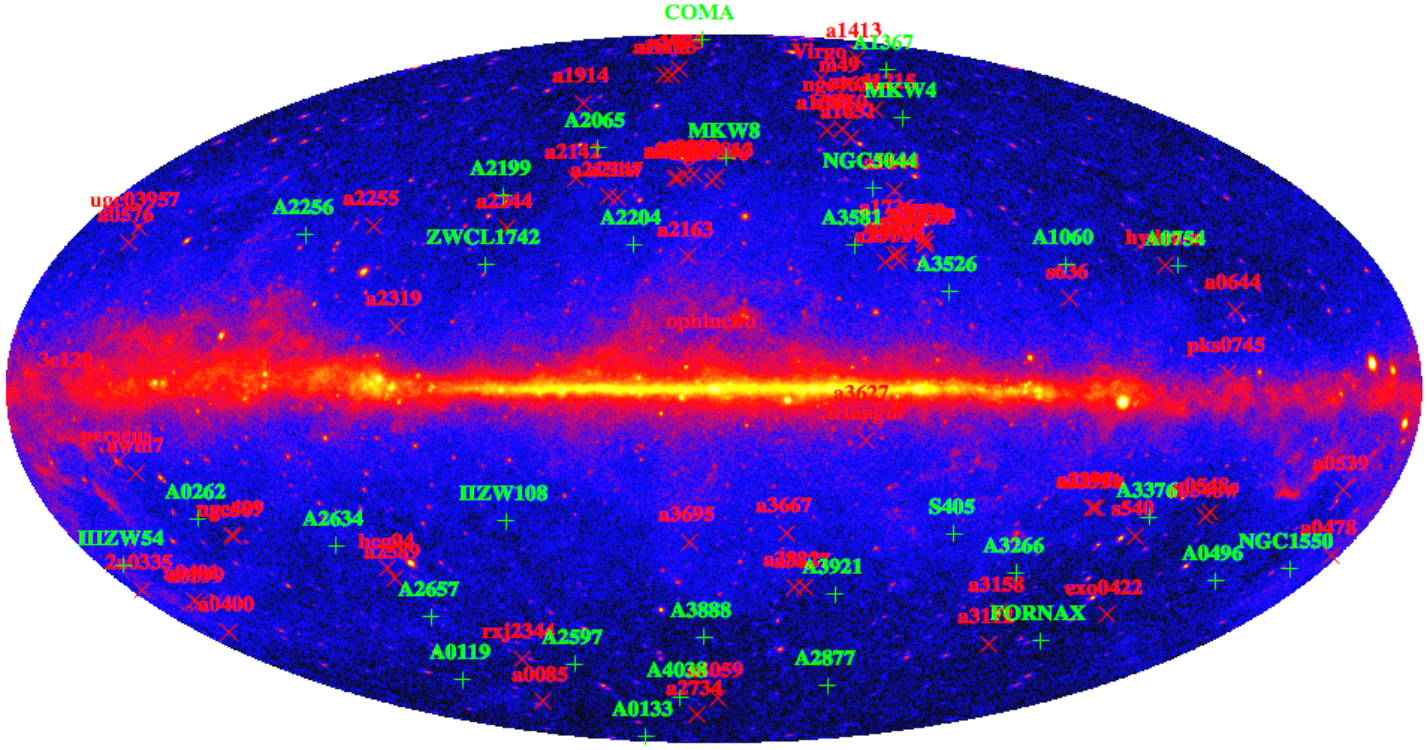

Figure 8.1: Selected clusters (in green) and removed clusters (in red), where the J-factors were obtained using an NFW profile and no boost from substructure, overlaid on a 4-year Fermi-LAT counts map.

References

[1] S. Zimmer, M. Llena Garde, J. Conrad et al. **Search for Dark-Matter-induced gamma rays from Galaxy Clusters**. *In Preparation* 2015.

[2] T. H. Reiprich and H. Böhringer **The Mass Function of an X-Ray Flux-limited Sample of Galaxy Clusters**. *Astrophys.J.* **567**:716, 2002.

[3] M. Ackermann et al. **Search for cosmic-ray induced gamma-ray emission in Galaxy Clusters**. *Astrophys.J.* **787**:18, 2014.

[4] M. Su, T. R. Slatyer, and D. P. Finkbeiner **Giant Gamma-ray Bubbles from Fermi-LAT: Active Galactic Nucleus Activity or Bipolar Galactic Wind?**. *Astrophys.J.* **724**:1044, 2010.